Numerical modelling of aeration and hydroelasticity in slamming loads and responses of marine structures

Von der Fakultät für Bauingenieurwesen und Geodäsie

der Gottfried Wilhelm Leibniz Universität Hannover

zur Erlangung des Grades

DOKTOR-INGENIEUR

Dr.-Ing.

genehmigte Dissertation
von

Ali Aghaei

Hannover, 2022

Referent:	Prof. Dr.-Ing. Arndt Hildebrandt
Korreferent:	Prof. Dr.-Ing. Bettar O. el Moctar
Tag der Promotion:	18. Februar 2022

Acknowledgments

Like "a journey of a thousand miles," this work started with the single step of sending a research proposal to Prof. Dr.-Ing. Hocine Oumeraci. He gave me this excellent opportunity to begin my Ph.D. study under his dedicated supervision, to which I am very indebted.

I hold deep gratitude to Prof. Dr.-Ing. habil. Torsten Schlurmann, and Prof. Dr.-Ing. Arndt Hildebrandt. Most of the work on this thesis was performed under their supervision and warm encouragement and valuable guidance.

I would also like to express my sincere, deep appreciation to Dr. -Ing. Stefan Schimmels. In our priceless discussions about this work, He warmly offered his valuable insights and expertise, which significantly elevated my work and knowledge.

This thesis was performed during my employment as a research associate at the Forschungszentrum Küste (FZK) in Hannover. I had the privilege of working with wonderful colleagues there. I have enjoyed working with them and learned from each one of them. Especially I would like to thank Dr. -Ing. Moritz Thom, Ms. Anja Masson, and Mr. Matthias Kudella for their kind and encouraging support.

I will never forget the support I received from Leibniz University and its excellent staff, who provide a very supportive environment for students at different levels and backgrounds.

Finally, my deepest gratitude goes to my family, particularly my parents and my wife, whose support and nurturing made this step possible for me.

Ali Aghaei

Hannover, 2021

Abstract

Slamming plays a significant role in the ultimate and fatigue limit state design of marine structures. Despite a relatively long history of investigations, there are still gaps in knowledge and open questions in understanding the slamming phenomenon and the approach it needs in the design phase due to its complex nature and limitations of research tools. The so-called hydroelasticity effect, which is the coupled interaction of structural responses with the body of fluid on both global and local scales, is one of the main complex aspects of slamming. Variation of fluid compressibility due to the mixing of air bubbles with the fluid, called aeration, alters the slamming loads and could also affect the hydroelastic coupling. The possible interaction of the two mentioned processes affecting the slamming physics and how to approach it in the analysis of slamming is still not well understood and is the focus of investigation in this thesis.

The research methodology of this work is based on studying the details of pressure and the flow field around the slamming area and the evolution of slamming force and structural response employing numerical modeling. A numerical tool for this purpose was developed and validated against benchmark experimental data available in the literature.

In the study of hydroelasticity, local shell deformations, as well as global deformations of the structure, were studied. The interlinked effects of local hydroelasticity and aeration were investigated by performing two sets of numerical simulation campaigns on the water entry of elastic flat plates and cylindrical shell sections. Both studies revealed that local flexibility has a noticeable reducing effect on peak values of slamming pressure and forces. This reduction effect of flexibility disappears for plates in the presence of aeration, which shows a significant indication of interdependence in the roles of aeration and hydroelasticity in slamming dynamics. In plate entry and cylinder entry simulations, aeration shows a damping effect on the response strain oscillations, strengthening with increasing aeration.

Both water entry studies present new insights with valuable details on slamming load's major characteristics and local structural response of plates and cylinders. Noticeable differences between plate and cylinder entries were observed; for instance, aeration causes a substantial extension of slamming load duration in plate entries, but no meaningful change is observed in cylinder entries. Extensive parameter studies led to new functional relations to determine peak slamming pressure/force in pure and aerated water entries in terms of relatively simple power-law approximations, which have been derived for plates and cylinders. The study shows that hydroelasticity may not be an essential issue for locally stiff structures, but considering air entrainment and entrapment processes is important to determine local loading characteristics.

This thesis also presents a novel simplified model of wave slamming on an SDOF cylindrical

structure. The model could reproduce the experimental slamming force and pressure time series of the large-scale wave slamming on a vertical monopile with a reasonable accuracy level. The validation study shows that the introduced simplified model could present valuable data on the physics of the interaction of a flexible cylindrical structure with impacting body of water. The simplified model was applied in a parameter study to investigate the effect of global structural vibration characteristics and aeration on wave slamming loads and structural response characteristics. The parameter study indicates that processes related to compressibility, such as aeration and air entrapment, are far more important than the structure's global flexibility. Since wave impact events in natural conditions may incorporate variable aeration levels in the water, which is shown to alter the structural response and duration of vibration, in both deterministic and stochastic studies of wave impact dynamics, the compressibility parameter is important and should be considered in the analysis.

Keywords: Slamming, Fluid-Structure Interaction, Aeration, Hydroelasticity, Water entry, Wave impact, Numerical modelling.

Kurzfassung

Slamming spielt eine bedeutende Rolle bei der Bemessung der Grenzzustände und des Ermüdungszustandes von maritimen Strukturen. Trotz vieler Untersuchungen in den vergangenen Jahrzehnten gibt es immer noch Wissenslücken und offene Fragen beim Verständnis des Slamming-Phänomens und der erforderlichen Herangehensweise in der Entwurfsphase aufgrund seiner komplexen Beschaffenheit und der Beschränkungen der Forschungsinstrumente. Der sogenannte Hydroelastizitätseffekt, der die gekoppelte Interaktion von strukturellen Reaktionen mit dem Fluidkörper sowohl auf globaler als auch auf lokaler Ebene darstellt, ist einer der wichtigsten komplexen Aspekte des Slammings. Die Veränderung der Fluidkompressibilität aufgrund der Vermischung von Luftblasen mit dem Fluid, der sogenannte Lufteintrag, verändert die Slamming-Belastungen und könnte auch die hydroelastische Kopplung beeinflussen. Die mögliche Interaktion der beiden genannten Prozesse, die sich auf das Slamming auswirken, und wie man sie bei der Analyse von Slamming berücksichtigen kann, ist noch nicht im Detail verstanden und steht im Fokus der Untersuchung in dieser Arbeit.

Die Forschungsmethodik dieser Arbeit basiert auf der Untersuchung der Details des Drucks und des Strömungsfelds um den Druckschlagbereich sowie der Entwicklung der Druckschlagkraft und der strukturellen Reaktion unter Verwendung der numerischen Modellierung. Zu diesem Zweck wurde ein numerisches Modell entwickelt und anhand von in der Literatur verfügbaren experimentellen Vergleichsdaten validiert.

Bei der Untersuchung der Hydroelastizität wurden sowohl lokale Schalenverformungen als auch globale Verformungen der Struktur untersucht. Die miteinander verknüpften Effekte von lokaler Hydroelastizität und Lufteintrag wurden untersucht, indem zwei numerische Simulationskampagnen zum Wassereintritt von elastischen flachen Platten und zylindrischen Schalenabschnitten durchgeführt wurden. Beide Studien zeigten, dass die lokale Flexibilität einen deutlich reduzierenden Effekt auf die Maximalwerte des Druckschlags und der Kräfte hat. Dieser reduzierende Einfluss verschwindet für Druckschläge auf Platten ohne Lufteintrag, was einen signifikanten Hinweis auf die gegenseitige Abhängigkeit der Rollen von Belüftung und Hydroelastizität in der Slamming-Dynamik zeigt. Bei Simulationen des Platteneintritts und des Zylindereintritts zeigt der Luftgehalt eine dämpfende Wirkung auf die Strukturschwingung, die sich mit zunehmendem Luftgehalt verstärkt.

Beide Studien zum Wassereintritt präsentieren neue Erkenntnisse mit bemerkenswerten Details zu den Auswirkungen der lokalen Hydroelastizität und des Luftgehalts auf die Charakteristiken der Druckschlaglast sowie auf die lokale Strukturantwort von Platten und Zylindern. Es wurden signifikante Unterschiede zwischen Platten- und Zylindereintritten gefunden; z. B. bewirkt der Luftgehalt eine erhebliche Verlängerung der Dauer der Schlagbelastung bei Platteneintritten, während bei Zylindereintritten keine auffällige Änderung

festgestellt wurde. Mit Parameterstudien wurden neue funktionale Beziehungen zur Bestimmung des maximalen Slamming-Drucks und der maximalen Slamming-Kraft für den Eintritt in unbelüftetes und belüftetes Wasser in Form von Potenzgesetz-Approximationen entwickelt, die für Platten und Zylinder untersucht wurden. Die Studie zeigt, dass die Hydroelastizität für lokal steife Strukturen nicht unbedingt von entscheidender Bedeutung ist, aber die Berücksichtigung von Lufteinschlüssen und Einschlussvorgängen ist wichtig, um lokale Belastungseigenschaften zu bestimmen.

In dieser Arbeit wird auch ein neuartiges vereinfachtes Modell des Wellenschlags auf eine zylindrische SDOF-Struktur vorgestellt. Das Modell konnte die experimentellen Zeitreihen der Slamming-Kraft und des Drucks des großflächigen Wellenschlags auf einen vertikalen Monopile mit einem angemessenen Genauigkeitsgrad reproduzieren. Die Validierungsstudie zeigt, dass das eingeführte vereinfachte Modell wertvolle Daten über die Physik der Interaktion einer flexiblen zylindrischen Struktur für den schlagartigen Wassereintritt liefern kann. Das vereinfachte Modell wurde in einer Parameterstudie angewandt, um die Auswirkung der globalen strukturellen Schwingungseigenschaften und des Luftgehalts auf die Wellenschlaglasten und die strukturellen Reaktionen zu untersuchen. Die Parameterstudie zeigt, dass Prozesse, die mit der Kompressibilität zusammenhängen, wie Luftgehalt und Lufteinschluss, weitaus wichtiger sind als die globale Flexibilität der Struktur. Da Wellenschlagereignisse unter realen Bedingungen variablen Luftgehalt im Wasser beinhalten können, die nachweislich die strukturelle Reaktion und die Dauer der Schwingung verändern, ist der Parameter der Kompressibilität sowohl in deterministischen als auch in stochastischen Studien der Wellenschlagdynamik wichtig und sollte in der Analyse berücksichtigt werden.

Schlüsselwörter: Slamming, Fluid-Struktur-Interaktion, Belüftung, Hydroelastizität, Wassereintritt, Wellenschlag, Numerische Modellierung.

Ehrenwörtliche Erklärung

Hiermit erkläre ich, dass ich die vorliegende Dissertation in Kenntnis und unter Beachtung der geltenden Promotionsordnung bei der Fakultät für Bauingenieurwesen und Geodäsie der Leibniz Universität Hannover eingereicht habe und mit einer Prüfung nach den Bestimmungen der Promotionsordnung dieser Fakultät einverstanden bin.

Ich versichere außerdem, dass ich die vorliegende Promotionsarbeit selbstständig und nur unter Verwendung der von mir angegebenen Quellen und Hilfsmittel verfasst habe. Sowohl inhaltlich als auch wörtlich entnommene Inhalte wurden als solche kenntlich gemacht. Die Arbeit hat in dieser oder vergleichbarer Form noch keinem anderem Prüfungsgremium vorgelegen.

Hannover, den 15.07.2022 $\hspace{6cm}$ Ali Aghaei

Contents

List of Figures

List of Tables

Acronyms

2D	two-dimensional
3D	three-dimensional
ALE	Arbitrary Lagrangian-Eulerian
DLM/FD	Distributed Lagrange Multiplier/Fictitious Domain
FE	Finite Element
FSI	Fluid-Structure Interaction
FZK	Forschungszentrum Küste institute
GWK	large wave flume
IB	Immersed boundary
SDOF	single degree of freedom
SOU	second-order upwind scheme
SPH	Smoothed Particle Hydrodynamics

List of Symbols

α	volume fraction (-)
$\mathbf{b}$	volumetric force source (Nm^{-3})
β	ratio of air bubbles volume to the fluid volume (-)
c	speed of sound (ms^{-1})
c_a	speed of sound in pure air (ms^{-1})
C_s	slamming coefficient (-)
c_w	speed of sound in pure water (ms^{-1})
$\boldsymbol{D}_r$	eigenvectors of nodal displacement space (-)
δ	Dirac delta function (-)
F	flux (m^3s^{-1})

$\boldsymbol{g}$	gravity acceleration vector (ms^{-2})
$\boldsymbol{I}$	identity tensor (-)
I_F	force impulse (Ns)
λ_s	Lame's first parameter (Pa)
μ	dynamic viscosity (Nsm^{-2})
μ_s	Lame's second parameter (Pa)
$\boldsymbol{\Omega}_x$	ALE reference domain, ALE grid domain (-)
$\boldsymbol{\Omega}_x$	spatial domain (-)
$\boldsymbol{\Omega}_X$	material domain (-)
$\boldsymbol{p}$	principal coordinate vector (m)
p	pressure (Pa)
p_r	principal coordinates (m)
ϕ	a general physical property (-)
ψ	compressibility (m^2s^{-2})
ρ	density (kgm^{-3})
$\boldsymbol{S}$	surface area vector (m^2)
σ	surface tension (Nm^{-1})
$\boldsymbol{\Sigma}$	Piola-Kirchhoff stress tensor (Pa)
$\boldsymbol{E}$	Green strain tensor (-)
t	time (s)
$\boldsymbol{T}$	stress tensor (Pa)
T_h	impact load duration (-)
$\boldsymbol{\tau}$	traction force (N)
$\boldsymbol{u}$	displacement vector (m)

$\boldsymbol{U}$	nodal displacement matrix (m)
$\dot{\boldsymbol{u}}$	velocity vector (ms^{-1})
$\boldsymbol{v}$	velocity vector (ms^{-1})
v_I	impact velocity (ms^{-1})
$\hat{\boldsymbol{v}}$	mesh velocity (ms^{-1})
$\boldsymbol{X}$	material coordinate vector (m)
$\mathbf{x}$	spatial coordinate vector (m)
χ	ALE reference coordinates (m)

1 Introduction

1.1 Motivation and problem statement

Marine structures are designed to resist extreme events in their lifetime caused by their special environment. However, due to uncertainties in the determination of extreme environmental loads, offshore and marine industries have been encountering structural failures causing environmental and economic damage and claiming human lives. Despite the significant number of studies for nearly 90 years, water impact loads, which in marine technology literature are referred to as "slamming" (Dias and Ghidaglia, 2018; Faltinsen et al., 2004), in general, and wave slamming (Figure 1.1), in particular, are still a primary source of uncertainty in the design and operation of marine vessels and structures (Tödter et al., 2020; Dias and Ghidaglia, 2018; Shams et al., 2017; Kapsenberg, 2011; Faltinsen et al., 2004).

Slamming occurs when there is a relatively large and vertical relative motion between the structural body and the water surface. In such cases, the water surface is relatively parallel to the structure's surface, and they hit, causing a substantial hydrodynamic load within a relatively short time.

(a)	**(b)**
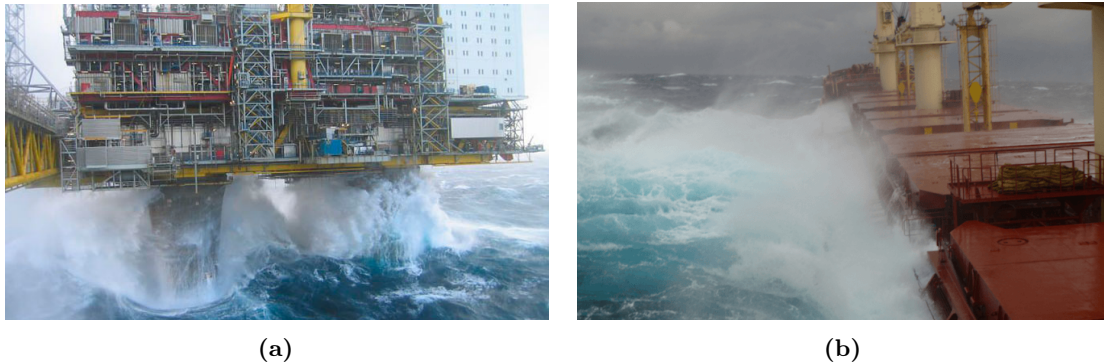
Figure 1.1: Wave slamming (a) on a platform, and (b) on a ship (snapshots are taken from https://www.youtube.com).

The mechanism described above inducing slamming load has the probability of occurrence in a relatively broad range of problems. Among the most important classes of slamming problems, the following may be named.

Wave slamming: Near-breaking, breaking waves and steep deep-water waves approaching the structure with water surface nearly parallel to the structure's surfaces (Figure

1.2 (a)) cause wave slamming loads (Wienke and Oumeraci, 2005; Hildebrandt and Schlurmann, 2012; Faltinsen, 2014).

Green water slamming: During the interaction of a marine vessel or a floating platform with rough sea, a large mass of water may land over the deck (Figure 1.2 (b)), which in some instances may lead to a slamming load named green water slamming (Buchner, 1995; Greco, 2001).

Sloshing-induced slamming: sloshing is a resonance phenomenon induced by a partially filled tank's resonating movements (Figure 1.2 (c)), which in extreme cases, generate slamming loads (Faltinsen and Timokha, 2009; Lyu et al., 2017).

Wetdeck slamming: Wetdeck slamming (Figure 1.2 (d)) occurs when, due to a relative vertical motion, the bottom of the multi-hull vessels and offshore platforms enters violently into the water (Ge, 2002).

Bow-stem slamming: The relative vertical motion of steep waves toward the bow of a moving vessel (Figure 1.2 (e)) causes the bow-stem slamming (Faltinsen et al., 2004).

Wave run-up slamming: During the impact of steep waves on the vertical structural members, a high-velocity upward flow, named run-up flow (Figure 1.2 (f)), may form, which may cause slamming loads on the upper platforms (Faltinsen et al., 2004; Damsgaard et al., 2007; Luengo Frades et al., 2019).

Highly intensive and localized pressure generated in slamming may cause local damage to the structural members, which may also lead to total failure of the structure. Several reports of such incidents can be found in the literature, for example, Kettle (2015), and Cruz and Krausmann (2008) in the offshore structures industry, and Gorf et al. (2002), and MAIB (2007) in the shipping industry. Kettle (2015) reviewed the experiences of wave slamming damages that occurred to the offshore structures in the North sea during the Britta storm. Cruz and Krausmann (2008) analyzed the damage on the offshore platforms in the Gulf of Mexico during Hurricanes Katrina and Rita. Figure 1.3 presents examples of structural damage due to wave slamming that occurred in recent years.

Slamming may also contribute to the structural components' fatigue failure by triggering a transient resonant response of the structure. This phenomenon is called ringing in the offshore structures industry (Kwon et al., 2001; Bredmose et al., 2013; Chaplin et al., 1997). The so-called whipping response in the ships also has the same mechanism and effect as ringing (Tuitman, 2010; Oberhagemann and el Moctar, 2011; Sun, 2007).

Two major interconnected phenomena may be acknowledged as the leading causes for current knowledge limitations about the slamming problem:

1. The slamming phenomenon is an outcome of strongly coupled interactions between fluid and structure. Therefore, the elastic interaction of fluid and structure may significantly affect wave impact loads and the response of the structure.
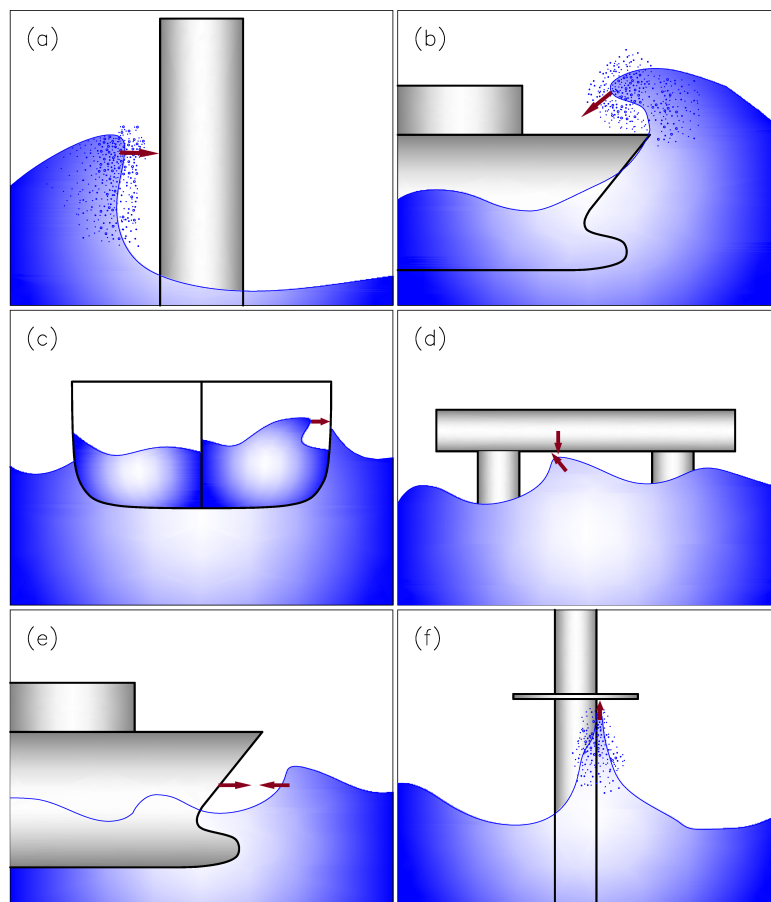
Figure 1.2: Sketches of slamming types: (a) breaking wave slamming, (b) Green water slamming, (c) Sloshing, (d) Wetdeck slamming, (e) bow-stem slamming, and (f) Wave run-up slamming (Drawings by the author).

2. In violent impact incidents, which may occur in a breaking wave impact, water entry, or sloshing, air in water as dispersed air bubbles or entrapped air packets influence the temporal and local distribution of the impact pressure, which in turn affects the response of the structure.

Simulating such complex problem with controlled processes like aeration, details of the flow, flow separation, structural vibrations, local cavitation and etc. in a physical model experiment is a very hard and expensive task. Such experiments, in addition to the costs and complications, have also inevitable limits in terms of capturing all the important details of the physical processes due to measurement and other technical constraints. On the other hand, scale has significant influence on the results of impact experiments with aerated water and scaling laws for such experiments still need to be developed (Bredmose et al., 2014; Kapsenberg, 2011).

Figure 1.3: Wave slamming damage examples (a) on a platform in Gulf of Mexico during Hurricane Ike (taken from https://www.offshore-mag.com), and (b) on a FPSO (taken from Buchner et al. (2004)).

The mixing of air bubbles in the fluid called aeration (Bredmose et al., 2014), may have an intertwined effect with the hydroelasticity on the slamming loads. To the author's knowledge, no research has been performed to comprehensively investigate the effects and feedback mechanisms of aeration and hydroelasticity, focusing on the characteristics of slamming evolution and structural response. Understanding the processes and interaction is still lacking, and it is not clear how and when complex processes like aeration/compressibility or hydroelasticity in slamming problems have to be taken into account for practical applications and design studies.

1.2 Objectives

The primary aim of this thesis is to improve the knowledge on the slamming phenomenon and the way its dynamics evolve and are affected by interacting processes such as aeration, local and global interaction of the structure with fluid. The generated knowledge reduces the uncertainties in the practice of determining and analyzing the slamming loads and local and global responses of the structure as the primary target variables for checking the design of the structure in different limit states.

The detailed specification of the objectives is presented at the end of chapter 2.

1.3 Methodology and Outline of the thesis

According to the defined objectives briefly stated above, the following methodology has been applied and reported in 6 chapters. The work starts with a survey of literature on slamming and the role of hydroelasticity and aeration, in particular documented in chapter

2. This study identifies the current knowledge gaps, based on which the core questions of this thesis and objective specifications are presented at the end of chapter 2. The process of developing a suitable numerical model and validation tests on the modeling methodology are addressed in chapter 3. The chapter starts with a review and analysis of the state-of-the-art modeling approaches in fluid-structure interaction, which leads to the selection of numerical methods and tools applied in this study. The chapter continues by describing the implemented numerical modeling algorithm and its validation. Chapters 4 and 5 present two systematic parameter studies on the investigation of the effects of local hydroelasticity and aeration on the characteristics of slamming loads and local responses of the structure. In chapter 4, the focus of the study is on elastic flat plates, where the setup and model concept of the comprehensive water entry slamming simulations with elastic flat plates along with the analysis of the results are described. Afterward, the documentation of a similar study on elastic cylindrical shells is presented in chapter 5. In chapter 6, a new simplified model is introduced to address the coupled interaction of global response of cylindrical structures with breaking waves. The model is validated by applying the data from large scale experiments conducted by Wienke (2001) in the large wave flume (GWK) of the Forschungszentrum Küste institute (FZK) (Schimmels et al., 2018) in Hannover, Germany. The chapter continues by reporting the results of a simulation series implemented with the new model in order to investigate the effect of global flexibility and aeration on the slamming loads and structural responses. Finally, the summarizing conclusion of this work, along with a proposed basic conceptual framework for dynamic analysis of structures under breaking wave slamming and a recommended outline for future research, are presented in chapter 7.

2 Review of the current knowledge

The most important slamming problems in offshore structures applications are the lateral breaking wave slamming and run-up deck slamming (Faltinsen et al., 2004). The reader is referred to Faltinsen et al. (2004), Sun (2007) and Van Nuffel (2014), in which they have very well explained different categories of slamming in the ship and ocean structure industries. Our focus here is on lateral wave slamming problems. The highly complex nature of the slamming phenomena caused the early researchers, among them the first and most significant were von Karman (1929) and Wagner (1932), to approach the problem through a basic model of vertical entry of a simple shaped object like a wedge or a cylinder into calm water (Figure 2.1), which can be analytically solved with certain simplifying assumptions such as rigid body, symmetric impact, incompressible fluid, irrotational flow, neglecting of gravity and no flow separation. Since Wagner, many analytical and semi-analytical studies extended Wagner's method to different shapes and applications (e.g., Korobkin (2006), Oliver (2007), Wienke and Oumeraci (2005)). Van Nuffel (2014) has reviewed and summarized those efforts to formulate the slamming force for basic shapes like plates and cylinders.

More general reviews on the slamming studies are presented in Mizoguchi and Tanizawa (1996), Faltinsen (2000), and Faltinsen et al. (2004). More recently, Kapsenberg (2011) reviewed the slamming research state-of-the-art from the ship design point of view. Chella et al. (2012) reviewed the studies on wave impact forces on fixed offshore structures in general and wind turbine substructures in particular. In their paper, they reviewed experimental and numerical investigations of wave slamming on cylindrical and truss structures, and additionally, they have summarized the recommendations from major design guidelines on dealing with wave impact loads on such structures. In the following, a review of the published works focusing on the central questions of current work is presented.
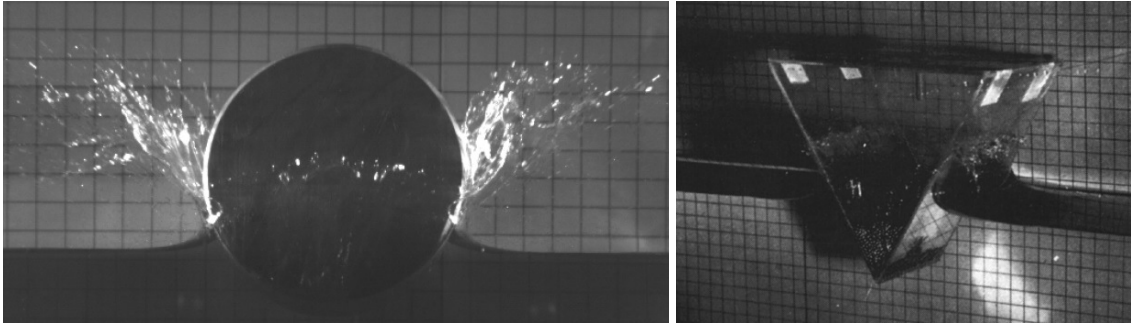
Figure 2.1: water entry of cylinder (Van Nuffel (2014), left) and wedge (Greenhow (1987), right).

2.1 Effect of hydroelasticity

The argument that structural responses and movements affect the hydrodynamic loads and vice versa is not newly known for the research community, particularly in the naval hydrodynamics area, and is named as "hydroelasticity effect" (Bereznitski, 2001; Chen et al., 2006; Faltinsen, 2000; el Moctar et al., 2017). In this section, the analytical, experimental, and numerical investigations on the role of hydroelasticity in the slamming phenomenon are reviewed.

2.1.1 Hydroelasticity theories

The terminology goes back to 1959 (Heller and Abramson, 1959), but the momentous development of the theories took place in the 1970s and 1980s (Chen et al., 2006; Hirdaris and Temarel, 2009). Developed only for one-hull ships, the early generation of hydroelasticity theories assumed the ship's hull as a non-uniform Timoshenko beam with a set of principal modes and natural frequencies and the fluid actions determined by means of strip theories (Bishop et al., 1986). To extend the theory to non-beam-like flexible structures, e.g., semi-submersibles or fixed offshore structures, general three-dimensional hydroelasticity theories have been developed, early begun by Wu (1984) and Bishop et al. (1986). Basically, three-dimensional hydroelasticity theories are based on a three-dimensional description of the structure moving *in vacuo*. The structural dynamics assumed to be linear, in which the displacements and deflections may be expressed as the sum of displacements in principal modes as previously shown by Bishop et al. (1986):

$$\boldsymbol{U} = \sum_{r=1}^{m} p_r(t)\boldsymbol{D}_r, \tag{2.1}$$

where $\boldsymbol{U}$ is the nodal displacement matrix, $\boldsymbol{D}_r(r = 1, 2, ..., m)$ are the eigenvectors of nodal displacement space, $p_r(r = 1, 2, ..., m)$ are a set of principal coordinates, and m is the total

number of degrees of freedom of dry structure. The nodal displacement matrix, hence, may
be express as

$$\boldsymbol{U} = \boldsymbol{Dp}, \tag{2.2}$$

with $\boldsymbol{p}$ being the vector $\boldsymbol{p} = [p_1(t); p_2(t); ...; p_m(t)]$. The coupled fluid-structure system,
which may be regarded as a monolithic system and referred to as the hydroelastic equation
of motion, is written in generalized matrix form in the frequency domain as

$$(\mathbf{a} + \mathbf{A})\ddot{\boldsymbol{p}}(t) + (\mathbf{b} + \mathbf{B})\dot{\boldsymbol{p}}(t) + (\mathbf{c} + \mathbf{C})\boldsymbol{p}(t) = \boldsymbol{E}, \tag{2.3}$$

Where $\boldsymbol{p}$ is the principal coordinate vector, $\mathbf{a}$, $\mathbf{b}$, and $\mathbf{c}$ are the generalized mass, damping
and stiffness matrices of dry structure respectively; $\mathbf{A}$, $\mathbf{B}$, and $\mathbf{C}$ are the generalized
hydrodynamic inertia, damping and restoring matrices and $\mathbf{E}$ is the linear generalized wave
exciting force. The matrices $\mathbf{A}$, $\mathbf{B}$, and $\mathbf{E}$ are defined by the integrals of incident, diffraction
and radiation potentials ϕ_I, ϕ_D, and ϕ_R over the mean wetted surface, by the assumption
that the fluid is inviscid, incompressible and irrotational and the motion amplitudes
and velocities are small enough so that the nonlinear terms at free surface and interface
kinematic and dynamic boundary conditions are neglected. As the radiation potential
induced by the deflections of the structure, which are expressed by linear combination of
principal modes, a similar expression should be adopted for them:

$$\phi_R(x, y, z, t) = \sum_{r=1}^{m} \phi_r(x, y, z, t) p_r(t). \tag{2.4}$$

There is no need in this context to go further in detail, which may be found, for instance,
in Wu and Cui (2009) or Bishop et al. (1986).

Having the fact that three-dimensional linear hydroelasticity theories have been significantly
helpful to determine the overall behavior of floating and offshore structures, there are
serious limitations rooted in the simplifying assumptions of these theories, among which
are as follows:

1. The flow characteristics in real life situations, particularly in breaking waves, are
   highly nonlinear, complex, and rapidly changing and may have compressibility effects;
   hence, the mentioned linearised models cannot accurately predict the behavior of
   such flows.

2. The mentioned models are not capable of capturing the detailed pressure distribution
   in slamming events and the corresponding local responses of the structure (Faltinsen
   et al., 2004; Kapsenberg, 2011)

2.1.2 Experimental and numerical studies on the hydroelasticity effect

All the studies on the hydroelasticity effect have been performed by water entry events, which are chronologically mentioned here. The first of such investigations was reported by Shibue et al. (1993), who experimentally studied the water entry of a cylindrical shell. They measured and analyzed the local strain and pressure values and found that the time integration of the pressure has more effect on the maximum strain than the maximum impact pressure.

The case of a flat plate slamming onto a calm water surface is appealing, mainly because it resembles cases in which the structural surface has a relatively small curvature and is nearly parallel to the water surface before the impact. There are a few studies on vertical slamming of an elastic plate, the first of which was implemented by Aarsnes (1994) and Faltinsen (1997). They studied the free-fall entry of flat aluminum and steel plates into calm water as well as regular wave crests with a variant curvature radius of 1.5 m to 21 m, which they intended to be relevant to wet-deck slamming on multi-hull vessels. The measurements consisted of bending strain, pressure, and acceleration in various locations of the plate span, drop velocity, and total force. The focus of their investigation was the plate responses in terms of bending strain. They found that, in contrast with the high scatter in maximum pressure values, the maximum strain shows much smaller scatter for a given value of impact velocity. In other words, the maximum pressure peaks show to have little importance in the deterioration of maximum strain in the plate. Their analysis of the experimental data also showed that the first vibration mode has a dominant effect on the maximum bending strain values.

Arai and Miyauchi (1998) carried out experimentally and numerically the water impact of a cylindrical shell. Their numerical model was based on a hydroelastic equation of motion, which applied the linear modal method. They concluded that hydroelasticity is important, and the structural strains calculated with loading based on rigid impact were significantly different from those based on hydroelastic impact.

Bereznitski (2001) studied the entry of two-dimensional wedges with low deadrise angles by means of commercial codes MSC-Dytran (MSC.Software, 2001) and LS-DYNA (Hallquist, 2001). He expressed that the ratio between the impact duration and the period of the first mode of vibration of the dry structure is the crucial factor in deciding when the solution of structural response should include hydroelastic effects.

Sun and Faltinsen (2006) developed a two-dimensional boundary element method (BEM) coupled with the modal structural analysis to simulate the impact of a cylindrical shell. They compared the results of their model with experimental results of Arai and Miyauchi (1998). Their numerical results show a clear difference between Wagner's method and Arai and Miyauchi's experiments.

Peseux et al. (2005) investigated the water entry of elastic wedges, both experimentally and numerically. Their numerical approach is a coupling of Wagner's asymptotic method with finite element models of elastic wedges with different deadrise angles and thicknesses. Comparing the distribution and evolution of pressure between experiments and numerical simulation shows an over-prediction of peak pressure values by their numerical model. Other similar studies on wedge impacts also has been performed by Allen and Battley (2015), Tenzer et al. (2015), and Shams and Porfiri (2015).

Panciroli et al. (2015) conducted water entry experiments on a flexible cylinder. The impact dynamics were studied by means of strain field monitoring, accelerometers, and high-speed imaging. Their results show significant differences in the impact dynamics with reference to the water entry of rigid bodies

2.1.3 Effect of global structural vibration characteristics

Since this is a very broad subject covering a diverse range of structural types, the focus of the present work is kept limited to cylindrical structures. Although there are hints in the literature suggesting the significant role of global hydroelasticity on the slamming load characteristics as well as structure response (Faltinsen et al., 2004; Hildebrandt, 2012), there is no published investigation on this matter for offshore structures.

In a hydroelastic interaction, slamming may excite the higher frequency modes of the structure, which may have significant implications for the fatigue life of the structure (Chella et al., 2012). On the other hand, this interaction may alter the slamming load's characteristics, such as rising time, peak force/pressure values, and duration. These aspects of slamming have been better addressed in the ship industry research (see Kapsenberg (2011), and el Moctar et al. (2017)), but the author could not find similar studies specifically carried out for offshore cylindrical structures, except for the work of Hildebrandt (2012), and Sagar et al. (2015).

In a part of his experimental investigation on the temporal and spatial variation of breaking wave impact pressures and forces exerted on a tripod model, Hildebrandt (2012) observed that in some breaking wave impact cases, a resonating excitation of higher natural frequencies in the structure occurred, which affected the characteristics of pressure evolution in the impact area. Such interactions were observed to be associated with 'audible acoustic shocks'. He also indicated that existing vibrations of the structure might significantly affect the magnitude and evolution of slamming pressures.

Sagar et al. (2015) applied a three-dimensional (3D) Finite Element (FE) model of monopile coupled with a numerical wave tank to investigate the hydroelasticity effects on the global responses of the monopile model structure subjected to regular, irregular, and focused waves. They found that the excitation of the monopile's second eigenfrequency due to impact incidents could significantly increase the structural response amplitudes.

2.2 Effect of aeration

In the process of fluid-structure interaction during a breaking wave impact onto a structure or a water entry incident, air may have two different roles. At the moment of contact between the water surface and the structure, there is a high chance that a pocket of air is trapped in the interface region (Hicks et al., 2012; Lange and Rung, 2011; Lin and Shieh, 1997; Van Nuffel, 2014; Wienke and Oumeraci, 2005). This entrapped air (for instance, see Figure 2.2) has an effect on the impact hydrodynamics called cushioning effect, which means that the air pocket, like a cushion, change the duration and intensity of the impact force. On the other hand, within the process of wave breaking or impact of a water body to a structure, air entrainment generates a mixture of water and dispersed air bubbles (Figure 2.3). Even a very slight amount of air bubbles can dramatically increase the water compressibility. For instance, adding 0.5% air bubbles into freshwater reduces the speed of sound in water by nearly an order of magnitude, from 1493 m/s down to 151 m/s, as given by Wallis equation (Murrone and Guillard, 2005):

$$\frac{1}{\rho c^2} = \frac{\beta}{\rho_a c_a^2} + \frac{(1-\beta)}{\rho_w c_w^2}, \tag{2.5}$$

where $\beta = V_b/V_f$, the ratio of air bubbles volume to the fluid, is the air fraction parameter, which is commonly used as a quantifying meter of aeration (Crawford, 1999; Lamarre and Melville, 1992; Walkden, 1999), and c, c_a, and c_w are the speed of sound in the mixture, pure air and pure water, respectively. An order of magnitude reduction in sound speed
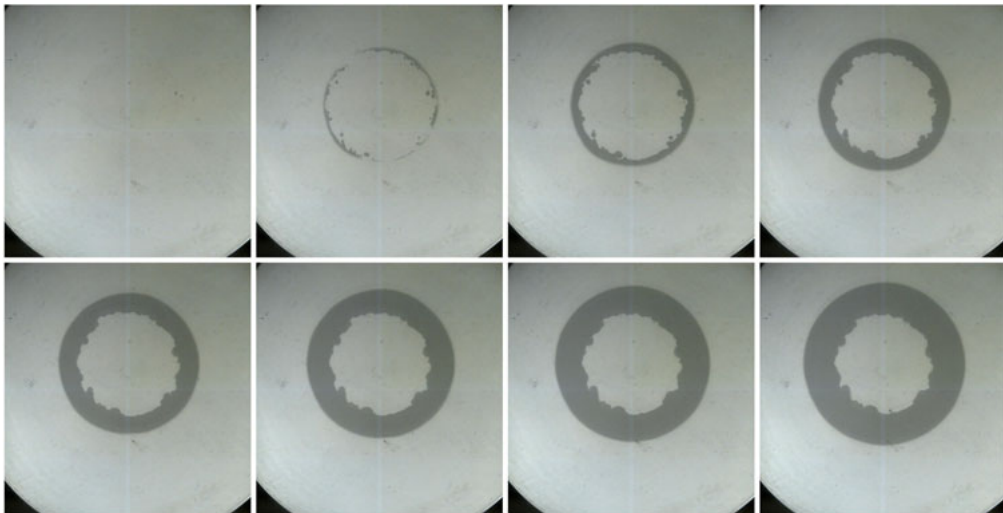
Figure 2.2: development of an air pocket during an entry of a sphere object into water (from Hicks et al. (2012)).

means a multiplication of compressibility ($\psi = 1/c^2$) by two orders of magnitude. Here also, the increased compressibility due to aeration may affect the impact dynamics significantly.

As can be seen in Figure 2.4, entrainment processes in seawater produce much finer bubbles (Katsir et al., 2015; Slauenwhite and Johnson, 1999), and coalescence of small bubbles is suppressed by the ionic repulsion in seawater (Cartmill and Yang Su, 1993; Slauenwhite and Johnson, 1999), which cause them to persist much longer below water surface by order of several wave periods (Scott, 1975). These phenomena enhance the importance of aeration in studying different water impact dynamics in ocean engineering problems, particularly breaking wave impacts.
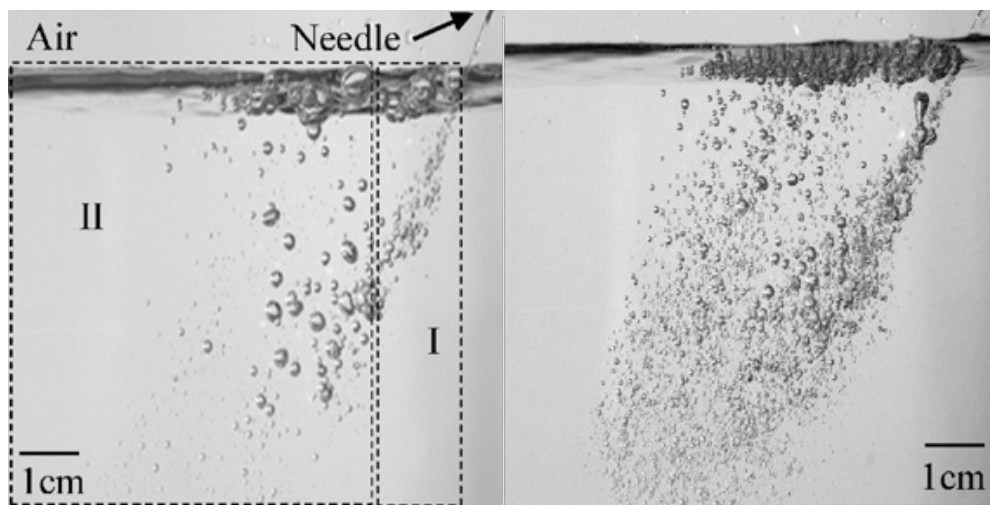
Figure 2.4: air entrainment during a water jet entry in fresh water (left) and saltwater (right) (from Katsir et al. (2015))
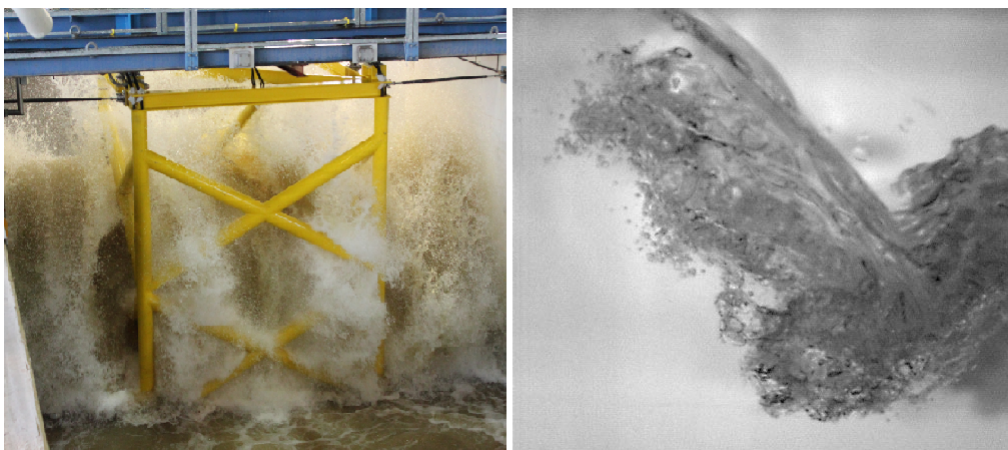
Figure 2.3: left: Air entrainment during wave impact into a model jacket structure (WaveSlam project, FZK, Hanover). right: Air entrainment during wave breaking process (from Deane and Stokes (2002)).

The role of aeration has been well investigated in the studies on breaking wave impact on rigid vertical walls, and several works can be cited like Oumeraci et al. (1993), Hattori et al. (1994), Crawford (1999), Wood et al. (2000), Bullock et al. (2007), Bredmose et al. (2009), Plumerault et al. (2012a) and Bredmose et al. (2015). However, no insight has been provided into the role of aeration in the hydrodynamics of wave impact on other types of marine structures like monopiles and jackets. Few research studies investigated the effects of aeration in the water entry problems. Two studies can be cited in this respect, implemented by Zhang et al. (2015) and Ma et al. (2016). Zhang et al. (2015) studied numerically the effect of fluid compressibility on the pick slamming pressures during the water entry of a rigid wedge, and Ma et al. (2016) investigated the entry of a rigid square flat plate into pure and aerated water, applying the results of experimental and numerical modeling. Both studies have shown that introducing aeration into the water can significantly reduce the local pressure and total forces.

2.3 Implications and specifications of the objectives and methodology

Obviously, approaching real-life simulation of breaking wave impact on a flexible structure is much more intricate than the water entry problem. To the author's best knowledge in all the previous studies, with one exception (Sagar et al., 2015), investigating experimentally and numerically the breaking wave impact on offshore structures, among which are Zhou et al. (1991), Chan et al. (1995), Irschik et al. (2004), Wienke and Oumeraci (2005), Arntsen et al. (2011), Christensen et al. (2005), Corte and Grilli (2006), Morgan and Zang (2010), Bredmose and Jacobsen (2010), Hildebrandt and Schlurmann (2012), and Choi et al. (2013), the structure was considered to be rigid, and the effects of aeration were neglected. According to the present review:

- The investigations on water entry of deformable objects have shown that the structural strain values calculated with loading based on slamming loads on rigid structures have differed significantly from those measured in elastic structural members.

- Variation of slamming pressure in time and space is more important than the peak pressure values for structural responses variation. Since aeration has been shown to have a significant effect on altering the spatial-temporal development of slamming pressure, it can be implied that both phenomena of hydroelasticity and aeration have intertwined roles in the slamming mechanics.

The present comprehensive review of the publications in the water entry and wave slamming studies showed that the intertwined roles of aeration and local/global hydroelasticity on the slamming load, its physical processes, and structural responses have never been investigated in detail before; Figure 2.5 illustrates an overview of the literature on this matter for visual help. The following questions are remained to be answered yet.

- How and when we need to consider the two-way local and global interaction of structure and fluid in the study of violent events of wave impact on marine structures?

- How aeration and the consequent change in the fluid's compressibility play a role in this process?
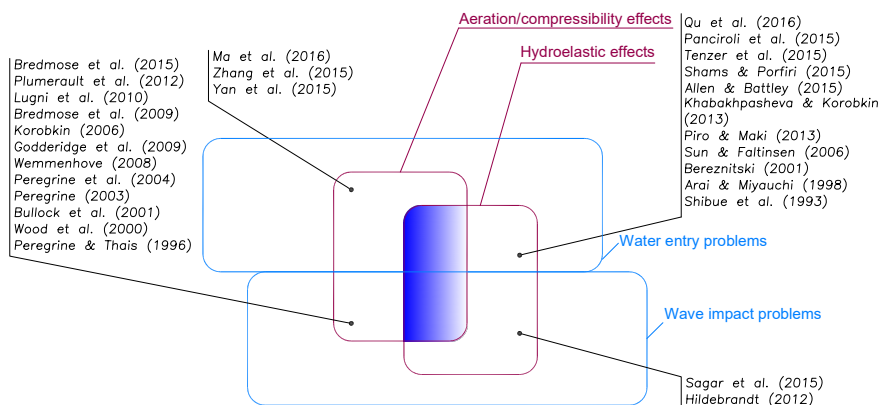
Figure 2.5: Summary of publications on water entry and breaking wave impact concerning the hydroelasticity and aeration effects (Drawing by the author).

Based on the raised questions above, the objectives of this thesis are as follows.

1. Developing and validating a numerical model capable of simulating the strongly coupled interaction of a flexible structure and water with free surface, which may be aerated;

2. Systematic numerical study of slamming of basic geometries to investigate in detail the interconnecting effects of aeration and local hydroelasticity on the evolution of impact pressures/forces and the local responses of the structures;

3. Develop a simple way to investigate the effects of global structural response interacting with aerated/pure fluid during the slamming event.

The above objectives are addressed for the first time in the marine industry. Together, fulfilling the above objectives will pave the way for developing a conceptual framework for studying the wave impact phenomena in marine structures' design process and answering the core questions.

The research project methodology planned to achieve the objectives mentioned above is an integration of six work packages (WP1 to WP6):

WP1: A proper numerical model that can adequately characterize the behavior of aerated fluid and structure in interaction is developed, which includes three major parts of coupling method, fluid domain discretization and solving method, and solid domain discretization and solving approach.

WP2: The numerical modeling tool is validated by applying the data available from water entry experiments.

WP3: A comprehensive set of plate entry simulations is implemented to create a database for the parameters study to investigate The interacting effects of local hydroelasticity and aeration on slamming and structural responses.

WP4: The methodology of WP3 is repeated for two-dimensional (2D) cylindrical shell objects.

WP5: A simplified numerical model for the interaction of a 1-DOF structure with braking waves is developed and validated.

WP6: The developed numerical model in WP5 is applied to investigate the effect of aeration and total structural deformation on breaking wave impact characteristics and structural responses.
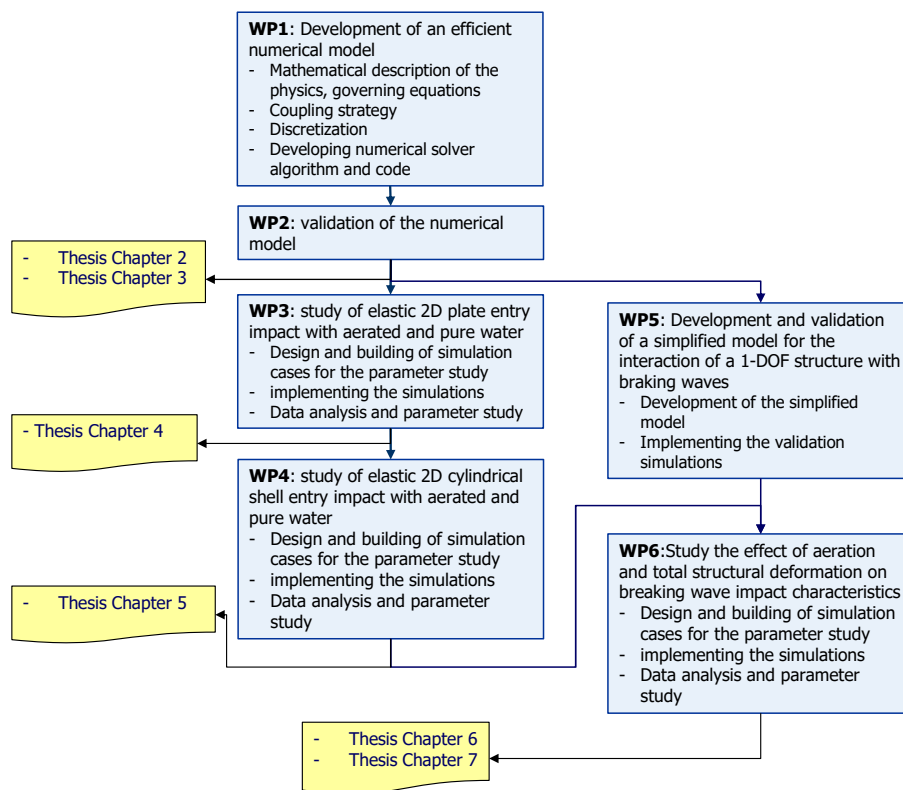
Figure 2.6: Illustrated overview of the current work methodology.

Summary chapter 2

- focusing on the wave slamming problems, a comprehensive review of the research literature carried out and presented in this chapter with the following summary:

  - The structural strain values calculated with loading based on slamming loads on rigid structures have been significantly different from those measured in elastic structural members.

  - Variation of slamming pressure in time and space is more important than the peak pressure values for structural responses variation. Since aeration has been shown to have a significant effect on altering the spatial-temporal development of slamming pressure, it can be implied that both phenomena of hydroelasticity and aeration have interrelating roles on the slamming mechanics.

  - The role of global hydroelasticity on slamming load characteristics and structural responses has not been addressed in detail for the offshore structures.

  - There is no study on the interrelating effects of aeration and hydroelasticity in the characteristics of slamming mechanics.

- based on the implications derived from the state of knowledge review, the following objectives, which are addressed for the first time in the offshore structures industry, were established for the current study:

  - Developing and validating a numerical model capable of simulating the strongly coupled interaction of a flexible structure and water with free surface, which may be aerated;

  - Systematic numerical study of slamming of basic geometries to investigate in detail the interconnecting effects of aeration and local hydroelasticity on the evolution of impact pressures/forces and the local responses of the structures;

  - Develop a simple way to investigate the effects of global structural response interacting with aerated/pure fluid during the slamming event.

3 Numerical methodology, implementation and validation

Development of a suitable numerical model for the current investigation is not a trivial task as many different factors should be considered to have both the required accuracy and cost/time efficiency. Therefore, a comprehensive review and analysis of the state-of-the-art Fluid-Structure Interaction (FSI) numerical modeling were carried out to find the most suitable numerical methods and tools to be applied in the study. As a result of the analysis, a package of numerical methods was assembled and implemented on the OpenFOAM platform (Weller et al., 1998). These efforts, along with the validation of the numerical methodology, are briefly explained in this chapter.

3.1 Fluid-Structure strong coupling

The fluid-solid interaction problem in this study is a two-field problem, the solid field (plate or cylindrical shell) and the fluid field (water and air), that share a common interface. At the interface, the following conditions should be satisfied (Wall, 1999).

$$\boldsymbol{u}_f = \boldsymbol{u}_s, \tag{3.1}$$

$$\dot{\boldsymbol{u}}_f = \dot{\boldsymbol{u}}_s, \tag{3.2}$$

$$\boldsymbol{\tau}_f + \boldsymbol{\tau}_s = \boldsymbol{0}, \tag{3.3}$$

where $\boldsymbol{u}$, $\dot{\boldsymbol{u}}$, and $\boldsymbol{\tau}$ are the displacements, velocities, and traction forces on the interface, respectively, with subscripts f and s denoting the variable's attribution to fluid and structure. In an FSI problem, three interrelating fundamental questions about the approach toward the solution should be answered (Felippa et al., 2001), which are

1. What kinematic description system is chosen for the domains,

2. Which coupling strategy to be applied, and

3. How the domains and equations are discretized.

Answering the above questions is highly related to the specific type of problem to be solved, and there are numerous combinations of choices in the literature. In the following, different ways to address each question are briefly reviewed, and the chosen methods for the current study are explained.

3.2 Kinematical description of the domains

Computational continuum mechanics usually apply one of the two classical descriptions of motion: the Lagrangian description and the Eulerian description. The Lagrangian description or material description characterizes the motion with respect to the material coordinates and time, while the Eulerian description or spatial description characterizes the motion with respect to spatial coordinates and time. A more detailed description of those systems is presented, for instance, in Holzapfel (2000). As solids' constitutive behavior is usually defined by applying the reference coordinates, the Lagrangian system is often preferred in solid mechanics. In contrast, due to the unavailability of reference coordinates in fluid materials, the Eulerian system is preferred widely in fluid mechanics studies. The FSI research community has developed various systems based on different combinations of those two fundamental descriptions for different classes of problems to exploit both methods' advantages and minimize their limitations. The most relevant and mature types of such frameworks are reviewed in the following.

3.2.1 Immersed boundary methods

Immersed boundary (IB) methods are the earliest approaches developed to fulfill the above-mentioned task (Wall et al., 2006), beginning with the work of (Peskin, 1972). He developed the method for the simulation of blood flow interaction with blood vessels. In the original work, the fluid domain variables are defined on a fixed Cartesian grid, and the solid is assumed to be thin-walled and massless, which could be defined by a curve function in 2-D space. The elastic curve is changing with time, independent of the grid, and its interaction with the fluid field is governed by a source term in the momentum equations of the fluid. The curve is discretized into finite number of Lagrangian nodes with material coordinates of $\boldsymbol{X}_k$, which are governed by the equations (Peskin, 1972):

$$\frac{\partial \boldsymbol{X}_k}{\partial t} = \boldsymbol{v}(\boldsymbol{X}_k, t), \tag{3.4}$$

where $\boldsymbol{v}(\boldsymbol{X}_k, t)$ is the velocity field at the coordinates of the kth membrane point. As noted above, the effect of the Immersed Boundary on the fluid is described by a source term

transferring the membrane stress by

$$\boldsymbol{f}(\mathbf{x}, t) = \sum_k \boldsymbol{F}_k(t) \delta(\mid \mathbf{x} - \boldsymbol{X}_k \mid), \tag{3.5}$$

where δ is the Dirac delta function, and $\mathbf{x}$ is the spatial coordinate vector. A smoother distribution function should replace the delta function in order to distribute the force over the points of the Cartesian grid. Thus, the forcing source term on each point in the grid may be calculated as

$$\boldsymbol{f}(\mathbf{x_i}, t) = \sum_k \boldsymbol{F}_k(t) \delta_h(\mid \mathbf{x_i} - \boldsymbol{X}_k \mid), \tag{3.6}$$

where δ_h is a distribution function.

Since Peskin, many studies carried out to suit the IB to more general types of problems, an overview of which can be seen in Peskin (2002), Mittal and Iaccarino (2005), and Hou et al. (2012). However, the current IB methods are still not suitable for high cases, and they still lack a satisfactory resolution near the interface (Hou et al., 2012). More importantly, the smoothed definition of the force term is a significant drawback toward developing fully implicit algorithms (Hou et al., 2012; Wall et al., 2006).

There are also other approaches like Distributed Lagrange Multiplier/Fictitious Domain (DLM/FD) methods (for instance: Baaijens (2001), Glowinski et al. (1999), van Loon et al. (2004)) or fully Eulerian methods as described in Dunne (2006) and Richter (2013), which have similarities with IB methods. Together with the IB, these methods are called fixed grid methods and have the same shortcomings as the IB approaches (Shahmiri, 2014; Wall et al., 2006).

3.2.2 Arbitrary Lagrangian-Eulerian description

The Arbitrary Lagrangian-Eulerian (ALE) is, by far, the most advanced and popular approach to describe the fields in FSI simulation. This method can be traced back to early works in the 60s and 70s like Noh (1963), Franck and Lazarus (1964), Hirt et al. (1974), and Donea et al. (1977). The method's fundamental idea is that a Lagrangian system describes the solid field, and an Eulerian system describes the fluid field. The particular characteristic of ALE is that the computational grid of fluid can be moved and defined in a Lagrangian manner depending on the movement of the fluid-solid interface.

The ALE system adds a third domain, the so-called referential configuration, to the material and the spatial configurations and use that domain, which identifies the grid domain, as reference. Figure 3.1 shows a sketch of the ALE system. The initial or material domain is named $\boldsymbol{\Omega}_X$, $\boldsymbol{\Omega}_x$ is set to be the spatial domain, and $\boldsymbol{\Omega}_\chi$ represents the reference or grid domain. The material domain description can be thought of as the domain on

which the material particles at time t_0 stand, those particles which cover the space $\boldsymbol{\Omega}_x$ at time t. The newly introduced, arbitrarily movable reference domain is only used to describe the kinematic process under consideration. The associated coordinates are referred to as reference coordinates $\boldsymbol{\chi}$. The changes in $\boldsymbol{\Omega}_x$ and $\boldsymbol{\Omega}_X$ domains are always considered with respect to the reference domain $\boldsymbol{\Omega}_\chi$. As can be seen in figure 3.1, these motions are given by the maps $\boldsymbol{\Phi}_t$ and $\boldsymbol{\Psi}_t$, respectively, which are symbolically represented by (Donea et al., 2004):

$$
\begin{aligned}
\boldsymbol{\Phi}_t : \boldsymbol{\Omega}_\chi \times [t_0, t[&\longrightarrow \boldsymbol{\Omega}_x \times [t_0, t[\\
(\chi, t) &\longmapsto \boldsymbol{\Phi}(\chi, t) = (\boldsymbol{x}, t)
\end{aligned}
\tag{3.7}
$$

and

$$
\begin{aligned}
\boldsymbol{\Psi}_t : \boldsymbol{\Omega}_\chi \times [t_0, t[&\longrightarrow \boldsymbol{\Omega}_X \times [t_0, t[\\
(\chi, t) &\longmapsto \boldsymbol{\Psi}(\chi, t) = (\mathbf{X}, t)
\end{aligned}
\tag{3.8}
$$

A physical property ϕ can now be expressed with respect to each of the introduced domains (Donea et al., 2004):

$$
\phi(\boldsymbol{x}, t) = \phi^*(\chi, t) = \phi^{**}(\mathbf{x}, t).
\tag{3.9}
$$
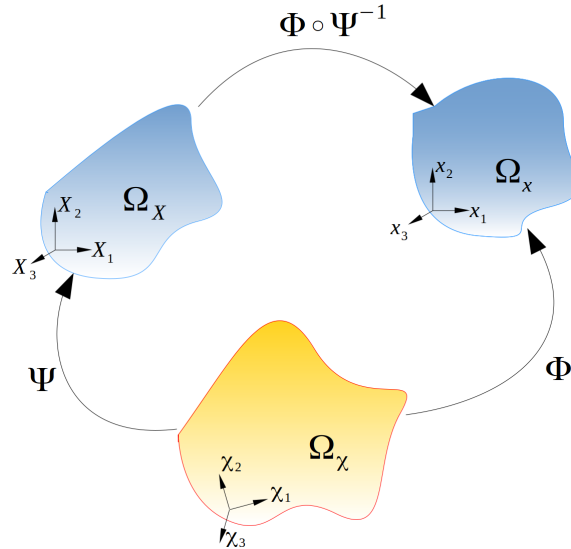
Figure 3.1: Material domain , spatial domain , and reference domain and their corresponding transformations in ALE approach (concept from Wall (1999) redrawn by the author)

According to the definitions of the mappings we can write (Donea et al., 2004):

$$\phi^*(\chi, t) = \phi \circ \mathbf{\Phi} = \phi(\mathbf{\Phi}(\chi, t)), \tag{3.10}$$

and

$$\phi^{**}(\boldsymbol{x}, t) = \phi \circ \mathbf{\Phi} \circ \mathbf{\Psi}^{-1} = \phi(\mathbf{\Phi}(\mathbf{\Psi}^{-1}(\boldsymbol{x}, t))). \tag{3.11}$$

Material, spatial, and referential time derivatives in ALE

The material time derivative $\frac{D(.)}{Dt}$ the differentiation of a (scalar, physical) property of a particular material particle (i.e., $\boldsymbol{X} = const.$) by time can be expressed with respect to the reference domain by application of the chain rule in (Wall, 1999):

$$\frac{D\phi}{Dt} = \frac{\partial \phi^{**}}{\partial t}(\boldsymbol{X}, t)\Big|_{\boldsymbol{X}} = \frac{\partial \phi^*}{\partial t}(\chi, t)\Big|_{\chi} + \frac{\partial \phi^*}{\partial \chi}(\chi, t)\frac{\partial \chi}{\partial t}\Big|_{\boldsymbol{X}}. \tag{3.12}$$

Applying the chain rule and substituting the variables, the relationship between material and referential time derivation, which can also be referred to as the ALE basic equation (Wall, 1999), may be written as

$$\frac{D\phi}{Dt} = \frac{\partial \phi^*}{\partial t}(\chi, t)\Big|_{\chi} + \boldsymbol{c}\,\frac{\partial \phi}{\partial \boldsymbol{x}}(\boldsymbol{x}, t), \tag{3.13}$$

in which, The ALE convective velocity $\boldsymbol{c}$, can be introduced as the difference between the material velocity and the mesh velocity.

3.2.3 Fully Lagrangian particle methods

A rather new approach in FSI is to describe the whole domains in fully Lagrangian manner. Gingold and Monaghan (1977) and Lucy (1977) carried out the earliest development of the concept to be applied in astrophysical dynamics. They named the method Smoothed Particle Hydrodynamics (SPH). In 1990s the method drew the researchers interest in other fields like continuum solid and fluid mechanics.

The main idea in the SPH and other particle methods is that the physical domain is represented by a finite number of particles, which posses the properties of the material they represent. Any vector or scalar property of a particle can be approximated by the summation of relevant quantities of the neighboring particles (Liu and Liu, 2010):

$$\phi(\mathbf{x}_i) = \sum_j \phi(\mathbf{x}_j) W(\mid \mathbf{x}_i - \mathbf{x}_j \mid, h) dV_j, \tag{3.14}$$

where j is the index of neighboring particles for particle i, $\mathbf{x}_i$, $\mathbf{x}_j$ are position vectors, W is

the kernel function, h is the smoothing length, determining the maximum neighborhood radius, and dV_j is the volume of particle ($dV_j = \frac{m_j}{\rho_j}$). More details about the approach and its history can be found in Monaghan (2005), Gomez-Gesteira et al. (2010), and Liu and Liu (2010).

The SPH method and other similar mesh-free methods are still in the early stages of their maturing process, and there are major drawbacks yet which make them infeasible for the current study; they are listed as follows.

- In contrast with the grid-based methods, the implementation of either Dirichlet or Neumann boundary conditions is not straightforward, which could be a source of inconsistencies in the field boundaries and it is still under investigation (Liu, 2002; Monaghan, 2005; Nguyen et al., 2008);

- The accuracy and stability of the method, especially for pressure field, has been so far a challenging topic (Agertz et al., 2007; Fang et al., 2009; Graham and Hughes, 2008; Liu and Liu, 2010);

- Due to their explicit nature, SPH-type methods could be computationally expensive, particularly when applied to large domains like in coastal process simulations (Gomez-Gesteira et al., 2010; Monaghan, 2005; Price and Federrath, 2010).

The present study needs very high-resolution data on the pressure field, water free surface, and fluid-solid interface, particularly in the impact area. According to the comprehensive review that was briefly outlined above, the ALE approach is very closer to the present study's requirements. The review revealed that the other two classes of methods still have intrinsic drawbacks, particularly in capturing the pressure field with high resolution and accuracy.

3.3 Coupling strategy

In the most general point of view, there are two principal ways to solve a multi-physics problem like fluid-solid interaction, *monolithic* (Bazilevs et al., 2013; Hübner et al., 2004) and *partitioned* (Deparis et al., 2006; Felippa et al., 2001; Matthies and Steindorf, 2002) approaches. In a monolithic approach, the whole domains are treated in a single system of equations, and all the entities advance in time simultaneously. On the other hand, each field is modeled and march in time separately in a partitioned approach. The interaction between fields in the partitioned approach governs the fields by communicating the interface information between fields using prediction, substitution, and synchronization techniques. Figure 3.2 depicts the two method groups presenting $\mathbf{F}$ as a differential operator, and ζ and ξ as variable systems for two domains.

Both techniques have their advocates, and neither is superior over the other in technical terms and outcome. However, in the present work, the partitioned approach is favored
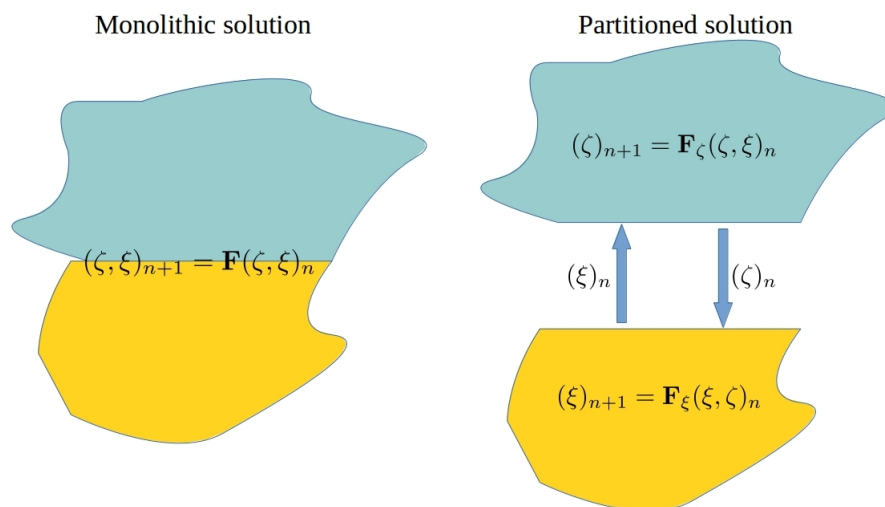
Figure 3.2: Monolithic and Partitioned methods description (drawing by the author).

because of its "modularity", as phrased by Felippa et al. (2001). it means we can choose for each field separate formulation, discretization, meshing, and solving techniques that fit best to each domain. Therefore in the following, the focus is spent on the partitioned methods.

3.3.1 Partitioned techniques:

In terms of data transfer between the two fields via the interface, partitioned methods can be divided into two main categories, *Algebraic* and *Deferential* methods (Kassiotis, 2009). Algebraic methods couple the fields through algebraic constraints. Algebraic constraining implemented applying *Lagrange Multipliers* or *Penalty Factors*. More details can be seen, for instance, in Felippa et al. (2001), Park et al. (2001), and Ross et al. (2008). In differential partitioning approaches, the difference between shared variables in the interface is minimized. To reach the equilibrium state on each time step, the shared interface variables have to be transferred between partitions. The information transfer could be at least on time in each time step, called the staggered scheme or explicit scheme, or it could be an iterative process of data exchange until convergence.

In algebraic methods, we face a third virtual field, which should also be discretized and solved. Ross et al. (2009) carried out a simplified comparison between algebraic and differential approaches to solving an FSI problem. They show that the algebraic method is at least 4.5 times more computationally expensive than the differential approach. Hence the algebraic approach will be off the choice for the current work. In differential methods, the staggered scheme or explicit scheme is a weakly coupled method, in which the results from one computation are given to the next one without any feedback. Since this method does not apply to the present work's specific problem, We continue in the following with the iterative schemes.

The iterative solving process of an FSI problem for each time step is to find the interface displacement $\boldsymbol{\lambda}$, which satisfies equation (3.3). The other two interface conditions (3.1) and (3.2) are enforced by the no-slip boundary condition in the fluid domain. The method could be expressed further utilizing the Steklov-Poincaré operators (Deparis et al., 2006). Each domain's solver, regardless of its details, can be associated with a Steklov-Poincaré operator as presented in Deparis et al. (2006) such that

$$S_f(\boldsymbol{\lambda}) = \boldsymbol{\tau}_f, \tag{3.15}$$

$$S_s(\boldsymbol{\lambda}) = \boldsymbol{\tau}_s. \tag{3.16}$$

Each of both operators also has an inverse so that any given traction force associates the interface displacement. This description of the inverse operator in the solid domain is associated with the solid domain solver, in which the traction forces are the boundary conditions and the outputs are the displacements. Using the above formulation, we can rewrite the condition (3.3) as

$$S_s^{-1}(-S_f(\boldsymbol{\lambda})) = \boldsymbol{\lambda}. \tag{3.17}$$

Gauss-Seidel algorithm

regarded as a fixed-point method, the Gauss-Seidel algorithm solves (3.17) with the following iteration:

$$\boldsymbol{\lambda}^{k+1} = \boldsymbol{\lambda}^k + \omega^k(\boldsymbol{\lambda}^* - \boldsymbol{\lambda}^k), \tag{3.18}$$

where

$$\boldsymbol{\lambda}^* = S_s^{-1}(-S_f(\boldsymbol{\lambda}^k)), \tag{3.19}$$

and ω^k is the relaxation parameter calculated for each iteration step, usually with Aitken's method, which is proved to be an effective scheme in accelerating the convergence (Küttler and Wall, 2008). The Gauss-Seidel scheme convergence is unconditional with small enough time steps. Details about the convergence of the method can be seen in Steindorf (2002) and Matthies et al. (2006).

Block-Newton and Quasi-Newton algorithms:

Newton-Raphson based methods may speed up the convergence in exchange for the expensive computation of Jacobians. In a Block-Newton method, the following linear

system of equations must be solved (Deparis et al., 2006; Matthies and Steindorf, 2003):

$$\left[\boldsymbol{J}(\lambda^k) - \boldsymbol{I}\right] \Delta \boldsymbol{\lambda}^k = -\left[S_s^{-1}(-S_f(\boldsymbol{\lambda}^k)) - \boldsymbol{\lambda}^k\right],$$
$$\boldsymbol{\lambda}^{k+1} = \boldsymbol{\lambda}^k + \omega^k \, \Delta\boldsymbol{\lambda}^k, \tag{3.20}$$

where the $\boldsymbol{J}(\lambda)$ is the Jacobian of $S_s^{-1}(-S_f(\boldsymbol{\lambda}^k))$ in $\boldsymbol{\lambda}$:

$$\boldsymbol{J}(\lambda^k) = -\left[\boldsymbol{D}_\lambda(S_s^{-1}(-S_f(\boldsymbol{\lambda}^k)))\right]^{-1} \cdot \boldsymbol{D}_\lambda S_f(\boldsymbol{\lambda}^k), \tag{3.21}$$

in which $\boldsymbol{D}_\lambda$ is the partial derivation operator with respect to $\boldsymbol{\lambda}$.

To ease the expense of Jacobian computation, inexact Newton methods have been developed which apply the finite difference approximations of the Jacobian (Gerbeau and Vidrascu, 2003; Matthies et al., 2006; Matthies and Steindorf, 2003).

Applied implicit algorithm

The Block-Gauss-Seidel method is the most applied implicit method in the FSI literature because of its simplicity and relatively less expensive approach. The cost of Jacobian computation often diminishes the advantage of the Newton-type methods in terms of fast convergence (Kassiotis et al., 2011; Küttler and Wall, 2008). von Scheven and Ramm (2011) compared three implicit schemes of block-Gauss-Seidel with and without dynamic relaxation and the approximate Newton method. They show that with increasing the ratio of solid to fluid density, the difference between those methods in convergence time becomes significantly less (Figure 3.3). As in this research, the material in the structural domain has a much higher density than water, the difference between convergence rates of Newton or quasi-Newton methods and enhanced fixed point methods like block-Gauss-Seidel will be insignificant. On the other hand, the expense of Jacobian computation in Newton methods makes them much less attractive choices. The block-Gauss-Seidel method with dynamic relaxation is shown to be an efficient and robust method and easy to implement (Habchi et al., 2013; Küttler and Wall, 2008; Wall et al., 2007) and therefore, in this study, it is a suitable choice.
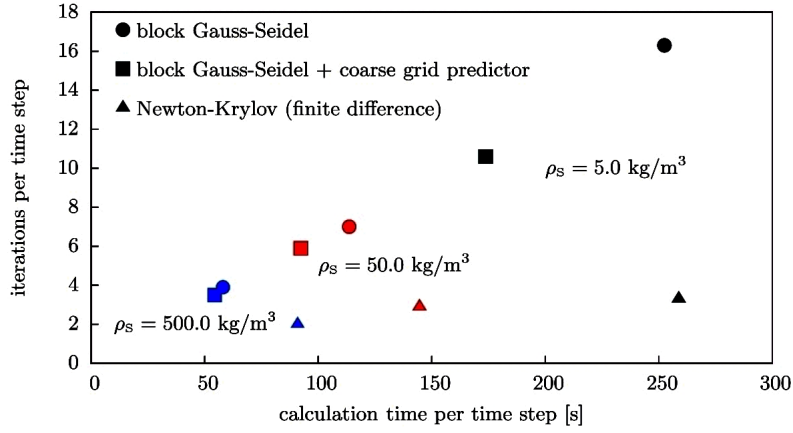
Figure 3.3: Comparison of average calculation time and number of iterations in a time step for three coupling methods (taken from von Scheven and Ramm (2011)).

3.4 Domain governing equations, discretization and solving algorithms

3.4.1 Fluid domain

Fluid domain mathematical model

In the current study, the fluid domain consists of air and water, which may be aerated. The Navier-Stokes equations still govern the behavior of such kind of fluid, but for the description of the bubbly water, different approaches are available. The *aggregated fluid* approach or *homogenized fluid* model, as is called more commonly in the literature, is by far the most examined and applied in similar studies like Wood et al. (2000), Bullock et al. (2007), Bredmose et al. (2009), and Plumerault et al. (2012b) because it is numerically much less expensive and more stable and easy to work with. Therefore this model will be applied in this work in the simulation of the fluid domain. In the homogenized fluid model, aeration is quantified with a specified uniform air fraction $\beta = V_b/V_f$, where V_b is the volume of bubbles dispersed in the aerated fluid volume V_f. In this way, modeling bubbly water is performed by changing the physical properties of the water phase. The most influential physical parameter of the mixture is the speed of sound, which is calculated by the Wallis equation (Murrone and Guillard, 2005):

$$\frac{1}{\rho c^2} = \frac{\beta}{\rho_a c_a^2} + \frac{(1-\beta)}{\rho_w c_w^2}, \tag{3.22}$$

where c, c_a, and c_w are the speed of sound in the mixture, pure air, and pure water, respectively. The two-phase fluid domain is assumed to consists of two immiscible phases, aerated/pure water and air, with no-slip between phases. Hence, it is suitable to treat both phases as one aggregated fluid with a single velocity field, and therefore, to solve one single momentum equation for the whole domain, which is numerically much less expensive and

simpler to work with comparing to the two-fluid approach. In this approach, the properties of the fluid, like density, will be defined as an averaged quantity (Bredmose et al., 2009; Wemmenhove, 2008):

$$\rho = \alpha_1 \rho_1 + \alpha_2 \rho_2, \tag{3.23}$$

where α_a, α_2, ρ_1 and ρ_2 are the liquid and gas phase volume fraction and densities, respectively. Such averaging scheme is also conducted on other varying properties like viscosity, molar weight, thermal conductivity, etc. The volume fractions are also constrained to the algebraic relationship

$$\alpha_1 + \alpha_2 = 1. \tag{3.24}$$

The integral form of the mass equation in an ALE grid may be written as

$$\frac{\partial}{\partial t} \int_V \rho dV + \int_{\partial V} \rho(\boldsymbol{v} - \hat{\boldsymbol{v}}).\boldsymbol{dS} = 0, \tag{3.25}$$

Where $\hat{\boldsymbol{v}}$ is the mesh velocity, and ρ is defined as in (3.23). The integral form of the fluid momentum equations in the ALE framework is applied as

$$\frac{\partial}{\partial t} \int_V \rho \boldsymbol{v} dV + \int_{\partial V} \rho \boldsymbol{v}(\boldsymbol{v} - \hat{\boldsymbol{v}}).\boldsymbol{dS} = \int_V (\nabla.\boldsymbol{T} + \boldsymbol{b}) dV, \tag{3.26}$$

where the stress tensor $\boldsymbol{T}$ is a linear function of the strain rate and is given by

$$\boldsymbol{T} = \mu \left[\nabla \boldsymbol{v} + (\nabla \boldsymbol{v})^T \right] - \left[\frac{2}{3} \mu (\nabla.\boldsymbol{v}) + p \right] \boldsymbol{I}, \tag{3.27}$$

and $\boldsymbol{b}$ is the volumetric force source term:

$$\boldsymbol{b} = \rho \boldsymbol{g} + \sigma \kappa \nabla \alpha, \tag{3.28}$$

where the first term is the gravity force, and the second term is the volumetric force representing the surface tension acting near the interface zone (Brackbill et al., 1992).

The present work's focus is on investigating the aeration induced compressibility effect on hydrodynamic impact loading and the corresponding structure responses. Therefore, we assume that the fluid flow undergoes an isothermal process, for which the equation of state is given by:

$$\rho_i = \psi_i p + \rho_{i0} \, , \ \psi_i = \frac{1}{c_i^2} \tag{3.29}$$

where c is the speed of sound inside the fluid; ψ is the compressibility parameter and

subscript i denotes each phase. The speed of sound in the air phase is $340m/s$, in pure water is $1490m/s$, and in the aerated water is calculated by (3.22).

Description of the free surface is modeled in this work using the Volume-of-Fluid (VOF) method derived for compressible flow as (Weller, 2008)

$$\frac{\partial}{\partial t}\int_V \alpha_1 dV + \int_{\partial V}\alpha_1(\boldsymbol{v}-\hat{\boldsymbol{v}}).\boldsymbol{dS} + \int_{\partial V}\alpha_1(1-\alpha_1)(\boldsymbol{v}-\hat{\boldsymbol{v}}).\boldsymbol{dS} = \int_V S_\alpha \alpha_1 dV, \quad (3.30)$$

where the source term S_α is

$$S_\alpha = (1-\alpha_1)\left(\frac{\psi_2}{\rho_2}-\frac{\psi_1}{\rho_1}\right)(\frac{\partial p}{\partial t}+\boldsymbol{v}\cdot\nabla p)+\nabla\cdot\boldsymbol{v}. \qquad (3.31)$$

The third term on the left-hand side of (3.30) is called the interface compression term added as an anti-diffusion term to the equation in order to increase the interface resolution by steepening the gradient of the volume fraction (for details see Rusche (2003); Weller (2008)).

Discretization and solving algorithm of the fluid domain equations

Summarizing section 3.4.1, we have three differential equations, namely the momentum, mass continuity, and the volume fraction equations, and three algebraic equations for determining the six field unknown variables: α_1, α_2, ρ_1, ρ_2, $\boldsymbol{v}$, p. The solving algorithm in this study is a pressure-based procedure; therefore, the governing equations need to be reformulated in order to have an explicit equation for the pressure field. The derivation of the pressure equation is performed by expanding the mass balance by replacing the density with pressure using the equation of state. Details of the derivation may be found in Miller et al. (2013).

Well-written elaboration of finite volume discretization may be found in Jasak (1996), and since the same techniques are used here, only important aspects of the discretization as applied in this study are described in the following.

In the finite volume method, space is divided into control volumes or cells, which should cover all the domains. Therefore space is transformed into a network of control volumes or cells, which is also called mesh (Figure 3.4).

Each cell inside the mesh has a finite number of flat faces, and Neighboring cells should share only one single face. The geometry of each cell is defined by its vertices. A typical cell P and one of its neighboring cells N are depicted in figure 3.5. the two cells are bounded by face f. the center of the cell, which is considered as the computational point and stores

Physical domain   FV mesh
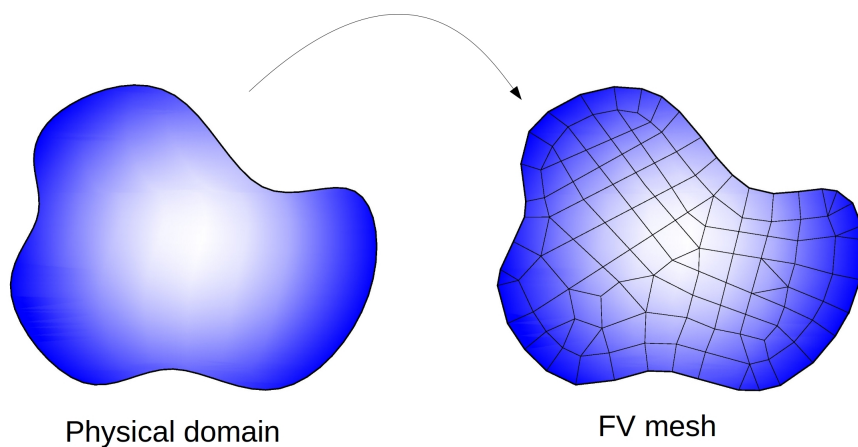
Figure 3.4: Discretization of physical space into FV mesh (drawing by the author).

the variable values, is defined as (Jasak, 1996)

$$\int_{V_p} (\mathbf{x} - \mathbf{x}_p)dV = 0. \tag{3.32}$$

Any cell face f can be either between two neighboring cells (internal face) or in boundaries of the domain (boundary face). The face area vector $\boldsymbol{S}$ is normal to the face pointing out of the cell of interest P to the neighboring cell N, and its magnitude is equal to the area of the face. In the collocated FV grid, the values of all field variables are stored in the cell centers, and with the assumption of linear variation inside the cell,

$$\phi(\mathbf{x}) = \phi_P + (\mathbf{x} - \mathbf{x}_p)(\nabla\phi)_P. \tag{3.33}$$

volume integrals over a cell volume is evaluated as

$$\int_{V_p} \phi(\mathbf{x})dV = \phi_P V_P \tag{3.34}$$

The time is simply discretized into finite number of time-steps, which may be constant or varying in order to optimize the computational resource usage. The main basis for determining the upper limit of the time-steps is the Courant-Friedrichs-Lewy (CFL) condition (Courant et al., 1928), in which

$$\Delta t \leqslant \frac{\Delta x}{c} \tag{3.35}$$

where c is the characteristic velocity, which due to the hyperbolic nature of compressible fluid equations, should be equal to sound velocity in the current medium (LeVeque, 2002).
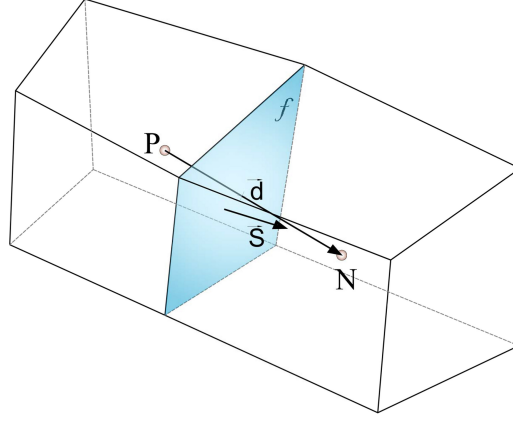
Figure 3.5: Neighbouring cells and their important parameters (drawing by the author).

Discretization of convection terms in ALE framework: Unlike its simple-looking form, The convection terms have complex behavior in discretized form, which has been the subject of numerous studies since the last decades extending to the present (Moukalled et al., 2015). The discretization of convection for a general property in the ALE grid is conducted with the approximation of the surface integral into the below summation highlighted by (Jasak and Tukovic, 2006).

$$\int_{\partial V_p} \phi(\boldsymbol{v} - \hat{\boldsymbol{v}}).\boldsymbol{n}dS = \sum_f \phi_f(\boldsymbol{v}_f - \hat{\boldsymbol{v}_f}).\boldsymbol{S}_f = \sum_f \phi_f(F_f - \hat{F}_f), \tag{3.36}$$

where f subscript indicates the values on the faces of the cell, F_f fluid flux, and $\hat{F}_f$ is the mesh flux resulting from the mesh movement. The main issue here is how the face values are interpolated from the cell center values, which are described below.

Interpolation of field values in cell faces The interpolation method has a very crucial role in the outcome of solving algorithms. The interpolation scheme should have both boundedness and stability properties and lead to nearest to real results. Among the available methods, the second-order upwind scheme is chosen. The *second-order upwind scheme (SOU)* interpolate any quantity ϕ at the face cell as

$$\phi_f = \phi_p^{upwind} + (2\nabla\phi_p^{upwind} - \nabla\phi_f).\boldsymbol{d}_{Pf}, \tag{3.37}$$

where ϕ_p^{upwind} is the value of ϕ in the upstream cell center, and $\boldsymbol{d}_{Cf}$ is the difference of cell center and face center position vectors:

$$\boldsymbol{d}_{Pf} = \mathbf{x}_P - \mathbf{x}_f \tag{3.38}$$

The gradient terms are calculated by applying a combination of orthogonal differencing and the Green-Gauss method.

Discretization of the momentum equation: The fluid momentum equation (3.26) has a nonlinear convection term $\int_{\partial V_p} \rho \boldsymbol{v}(\boldsymbol{v} - \hat{\boldsymbol{v}}).\boldsymbol{n}dS$, the semi-discretised form of which may be written as

$$\int_{\partial V_p} \rho \boldsymbol{v}(\boldsymbol{v} - \hat{\boldsymbol{v}}).\boldsymbol{n}dS = \sum_f \rho_f (F - \hat{F})_f \boldsymbol{v}_f. \tag{3.39}$$

 The above is a nonlinear term. The remedy for this complication, as applied here, is to linearize the term by using the existing fluxes from the previous iteration/time-step. Hence, we may write the discretized form of the fluid momentum equation as

$$\frac{\rho_P^* \boldsymbol{v}_P^{(n+1)} V_P^* - \rho_P^{(n)} \boldsymbol{v}_P^{(n)} V_P^{(n)}}{\Delta t} + \sum_f \rho_f^* (F - \hat{F})_f^* \boldsymbol{v}_f^{(n+1)} + \sum_f \mu^* (\nabla \boldsymbol{v}^{(n+1)})_f.S_f^* = \\ -\sum_f p_f \boldsymbol{S}_f^* + \sum_f \mu (\nabla \boldsymbol{v})_f^T.S_f^* - \frac{2}{3} \sum_f \mu (\nabla . \boldsymbol{v})_f S_f^* + \boldsymbol{b}_p V_p^*, \tag{3.40}$$

where the superscript $(n+1)$ denotes the current value, superscript (n) means the value from the last time-step, and $(*)$ superscript is used to indicate the latest available value. As seen above, the right-hand side of equation (3.40), which involves the pressure, is evaluated explicitly in order to arrange an iterative coupling with other equations.

Discretization of the pressure equation: As mentioned before, the pressure equation is evolved from the mass balance equation. The discretized form of pressure equation may be expressed as

$$\left(\frac{\alpha_1 \psi_1}{\rho_1} + \frac{\alpha_2 \psi_2}{\rho_2} \right)^* \left(\frac{p_P^{(n+1)} V_p^* - p_P^{(n)} V_p^{(n)}}{\Delta t} + \sum_f (F - \hat{F})_f p_f^* - p_P^* \sum_f (F - \hat{F})_f^* \right) \\ + \sum_f (F - \hat{F})_f^* = 0. \tag{3.41}$$

Discretization of the volume fraction equation: With the same process as above, the discrete version of the volume fraction equation is

$$\frac{(\alpha_1)_P^{(n+1)} V_p^* - (\alpha_1)_P^{(n)} V_p^{(n)}}{\Delta t} + \sum_f (\alpha_1)_P^{(n+1)} (F - \hat{F})_f^* = (S_\alpha)_P^* V_P^*. \tag{3.42}$$

Keeping the sharpness of the fluid/air interface is important here. An effective solution developed by Ubbink (1997) is to add an anti-diffusion term to the left-hand side of equation (3.42) to increase the interface resolution by steepening the gradient of volume fraction (for details, see Ubbink (1997), Rusche (2003), and Weller (2008)). The additional term, which is called the interface compression, is $\sum_{f} (\alpha_1)_f (1 - \alpha_1)_f (F_c - \hat{F})_f{}^*$. As it can be observed from the formulation, the compressive term is activated only in the interface areas where $0 < \alpha_1 < 1$. the *artificial compression flux* F_c is defined as (Weller, 2008)

$$F_c = min\left(C_\alpha \frac{|F_f|}{|\boldsymbol{S}_f|}, max\left[\frac{|F_f|}{|\boldsymbol{S}_f|}\right]\right)(\boldsymbol{n}_f \cdot \boldsymbol{n}_f),$$ (3.43)

where C_α is a user-tuned coefficient usually larger than and close to 1, and $\boldsymbol{n}_f$ is the face-centered interface normal vector given by

$$\boldsymbol{n}_f = \frac{\nabla(\alpha_1)_f}{|\nabla(\alpha_1)_f|}$$ (3.44)

Solution algorithm in the fluid domain   The fluid domain solution procedure applied in this study is a compressible two-phase flow version of PISO-type (Issa, 1986) methods, which is developed by (Weller, 2008). The algorithm consists of two outer and inner corrector loops. The outer loop is for correcting the momentum and volume fraction and the inner loop, which is also called the PISO-loop (Rusche, 2003), corrects the pressure and fluxes.

3.4.2 Solid domain

Solid domain mathematical model

Since the focus of the proposed numerical model is to study the effect of coupled interaction and fluid aeration on the hydrodynamic forces, and there is no intention to study the possible structural failure modes and the effects of nonlinear elastic or plastic behavior of the material, the simplest structural model that can fulfill the objectives of the model with acceptable accuracy will be applied to minimize the calculation costs.

As we suppose that there is no thermodynamic process in the solid domain, we need just the momentum balance for the solid domain.

The solid domain is described with Lagrangian configuration in the ALE system. The balance of linear momentum in the material description for an elastic solid can be written as follows.

$$\int_{V_0} \rho_{s_0} \frac{\partial}{\partial t}\left(\frac{\partial \boldsymbol{u}}{\partial t}dV\right) = \int_{\partial V_0} \boldsymbol{n} \cdot (\boldsymbol{\Sigma} \cdot \boldsymbol{F}^T)dS + \int_{V0} \rho_{s_0}\mathbf{f}dV$$ (3.45)

where $\mathbf{f}$ is the solid body force, $\boldsymbol{\Sigma}$ is the second Piola-Kirchhoff stress tensor, $\boldsymbol{F} = (\boldsymbol{\nabla}_0\boldsymbol{u}+\boldsymbol{I})^T$ is the deformation gradient, $\boldsymbol{u}$ is the solid displacement vector and subscript 0 indicates that the quantities are with respect to the reference configuration. The St.Venant-Kirchhoff constitutive law relating the second Piola-Kirchhoff stress tensor to the Green strain tensor:

$$\boldsymbol{\Sigma} = \lambda_s(tr\boldsymbol{E})\boldsymbol{I} + 2\mu_s\boldsymbol{E} \tag{3.46}$$

closes the system of equations, where λ_s and μ_s are the Lamé coefficients and the Green strain tensor $\boldsymbol{E}$ is related to the displacement vector by

$$\boldsymbol{E} = \frac{1}{2}\left[\boldsymbol{\nabla}_0\boldsymbol{u} + (\boldsymbol{\nabla}_0\boldsymbol{u})^T + (\boldsymbol{\nabla}_0\boldsymbol{u}).(\boldsymbol{\nabla}_0\boldsymbol{u})^T\right] \tag{3.47}$$

Discretization and solving algorithm of the solid domain equations

In order to avoid complications when using different discretization techniques in two domains, the solid domain equations are also discretized with a cell-centered finite volume method, which has been shown to be both effective and accurate (Fallah, 2004; Jasak and Weller, 2000; Slone et al., 2003; Tsui et al., 2013; Tuković et al., 2015). The details of the procedure are not discussed here, but can be found in Tuković et al. (2015) and Jasak and Weller (2000).

By using equations 3.45, 3.46, and 3.47, we may have the following integral form of momentum equation for the solid domain (Jasak and Weller, 2000):

$$\int_{V_p} \rho_{s_0} \frac{\partial^2(\boldsymbol{u})}{\partial t^2}dV - \int_{\partial V_p} \mu_s\nabla\boldsymbol{u} \cdot \boldsymbol{dS} =$$
$$\int_{\partial V_p} [\mu_s(\nabla\boldsymbol{u})^T + \lambda_s tr(\nabla\boldsymbol{u})\mathbf{I} + \mu_s\nabla\boldsymbol{u} \cdot (\nabla\boldsymbol{u})^T + \frac{1}{2}\lambda_s tr[\nabla\boldsymbol{u} \cdot (\nabla\boldsymbol{u})^T]\mathbf{I} + \boldsymbol{\Sigma} \cdot \nabla\boldsymbol{u}] \cdot \boldsymbol{dS}$$
$$+ \int_{V_p} \rho_{s_0}\mathbf{b}dV. \tag{3.48}$$

The surface integral in the right-hand side of equation (3.48) consists of the non-linear and inter-component coupling terms, which are treated explicitly in the solution procedure. Jasak and Weller (2000) showed that adding the diffusive term $\int_{\partial V_p} -(\mu_s + \lambda_s)\nabla\boldsymbol{u} \cdot \boldsymbol{dS}$ to both sides of the equation significantly improves the convergence of the solution. This

modification gives

$$\int_{V_p} \rho_{s_0} \frac{\partial^2 (\boldsymbol{u})}{\partial t^2} dV - \int_{\partial V_p} (2\mu_s + \lambda_s) \nabla \boldsymbol{u} \cdot d\boldsymbol{S} =$$

$$\int_{\partial V_p} [\mu_s (\nabla \boldsymbol{u})^T + \lambda_s tr(\nabla \boldsymbol{u})\mathbf{I} + \mu_s \nabla \boldsymbol{u} \cdot (\nabla \boldsymbol{u})^T + \frac{1}{2}\lambda_s tr[\nabla \boldsymbol{u} \cdot (\nabla \boldsymbol{u})^T]\mathbf{I} + \boldsymbol{\Sigma} \cdot \nabla \boldsymbol{u}] \cdot d\boldsymbol{S}$$

$$+ \int_{V_p} \rho_{s_0} \mathbf{b}\, dV$$

$$(3.49)$$

Unlike the finite element method, we discretize the solid part in a segregated style, where like the fluid domain, each component of the solid displacement vector is solved separately with separate matrices, and the inter-component terms are evaluated explicitly. This method leads to a well-behaving iterative solver saving significant computer memory (Jasak and Weller, 2000; Tuković et al., 2015).

To discretize the temporal term of equation 3.66, we apply the first-order backward Euler scheme, which is bounded without causing nonphysical stress fluctuations. Rearranging the explicit and implicit terms, the discretized form of equation (3.49) would look like below.

$$\frac{\rho_p \boldsymbol{u}_p^{(n+1)}}{\Delta t^2} - (2\mu_s + \lambda_s) \sum_f (\nabla \boldsymbol{u})_f . \boldsymbol{S}_f^{(n+1)} = \frac{2(\rho \boldsymbol{u})_p^{(n)} - (\rho \boldsymbol{u})_p^{(n-1)}}{\Delta t^2} +$$

$$\mu_s \sum_f (\nabla \boldsymbol{u})_f^T . \boldsymbol{S}_f^{(n)} - (\mu_s + \lambda_s) \sum_f (\nabla \boldsymbol{u})_f . S_f^{(n)} + \lambda_s \sum_f tr(\nabla \boldsymbol{u})_f \boldsymbol{S}_f^{(n)} + \qquad (3.50)$$

$$\rho_s \boldsymbol{f}_p V_p^{(n)} - \sum_f \boldsymbol{S}_b p_b^{(n)} + \sum_f |\boldsymbol{S}_b| \boldsymbol{t}_b^{(n)}.$$

The two last terms in equation (3.50) are the pressure and tangential stress, which are exerted on the solid cell faces in boundaries of the solid domain.

The solution algorithm of the solid domain is more straightforward than that of the fluid domain. As mentioned above, a segregated solution procedure is applied in the solving algorithm of the solid domain, in which all inter-component values are calculated explicitly using the latest available displacement field. A fixed point Gauss-Seidel iteration will converge the solution on each time step.

3.4.3 Mesh motion

The mesh deformation should follow the movement of the fluid-solid interface. To address this, the Laplace smoothing equations (Löhner and Yang, 1998), which have been demonstrated to be robust in large deformations and computationally efficient (Kassiotis, 2008),

were chosen to solve the mesh motion in this study. The Laplace smoothing equations to be solved along with the fluid and solid equations are defined as follows:

$$\nabla.(\gamma\nabla\hat{\boldsymbol{v}}) = 0, \tag{3.51}$$

where $\hat{\boldsymbol{v}}$ is the grid velocity field; and γ is a mesh diffusion coefficient. In order to maintain the mesh quality, and prevent mesh distortion and deterioration due to large displacements, particularly near the moving boundary, the following variable mesh diffusion coefficient is applied:

$$\gamma(r) = \frac{1}{r^2}, \tag{3.52}$$

where r is the distance to the nearest interface point.

3.4.4 Boundary conditions

In order to reduce the computational time, a symmetry plane boundary condition is applied in all of the simulations. The boundary conditions for all variables are summarized in Table 3.1.

Table 3.1: Boundary conditions for solid and fluid variables.

Boundary name	$\boldsymbol{u}_s$	$\boldsymbol{v}_f$	p	α_1	α_2
Wall	-	Fixed value, $\boldsymbol{0}$	Zero gradient	Zero gradient	Zero gradient
Solid-fluid interface	Traction-displacement	$\dot{\boldsymbol{u}}_s$	Zero gradient	Zero gradient	Zero gradient
Atmosphere	-	Free inlet/outlet	Fixed value, $10^5 Pa$	Zero gradient	Zero gradient

3.5 Implementation and validation of the numerical method

3.5.1 Implementation

In order to simulate the water entry events with the methodology summarized above, a new FSI solver package was developed on the open-source numerical coding platform of OpenFOAM (Weller et al., 1998). OpenFOAM is a C++ library of numerical continuum mechanics developed since 1998. It has a genuine object-oriented approach toward implementing tensor algebra and computational PDEs, making it appropriate for understanding and further development by the users. Further details on this platform can be found, for instance, in Weller et al. (1998) and Jasak et al. (2007). Figure 3.6 depicts the currently developed FSI package concept, which shows its three main components and their data exchange directions. The original contribution of the present work for the solver package development is described as follows.

- The FSI coupling module named `entryFsiFoam` was developed based on the `fsiFoam` solver (Tuković et al., 2018). `entryFsiFoam` can handle the case of a moving solid with an initial velocity and automatic time-stepping based on the CFL number.

- A two-phase compressible flow solver module named `compressibleInterFlow` was developed. The solver is a single `C++` class that is developed based on the OpenFOAM fluid solving package `compressibleInterFoam`.

- The existing solid solver class `unsTotalLagrangianSolid` is modified to be able to set lumped mass and initial velocity in the solid body.

The FSI solver procedure for the water entry simulations is summarized in the algorithm 3.1.

Algorithm 3.1: the `entryFsiFoam` solution algorithm for water entry events.

---

while *t < maximum duration* **do**
    adjust time step based on the maximum CFL number of the last time step;
    if *t = 0* **then**
        initiate the solid domain with initial velocity ;
        calculate the solid displacement ;
        update the interface displacement;
        interpolate the solid interface motion to the fluid mesh boundary ;
    else
        while *displacement residual > tolerance* **do**
            move the fluid mesh by solving the mesh motion equation ;
            evolve the fluid domain with the fluid domain solver;
            update the force on the solid interface;
            evolve the solid domain with the solid domain solver;
            update the interface displacement;
            calculate the interface displacement residual;
            interpolate the solid interface motion to the fluid mesh boundary ;
        end
    end
end

3.5.2 Mesh sensitivity study

A mesh sensitivity study was performed for a typical water entry simulation case, which showed that the impact pressure peak becomes insensitive to the mesh fineness when the near-wall cell dimensions are less than 0.4 mm (Figure 3.7). For such a fine mesh, the total number of grid cells in the present 2D fluid domain is close to 150000. Simulating an FSI water entry case, in which both fluid phases (air and water) are compressible, for an impact duration of 0.03 seconds, costs 63 hours of computation time using 12 Xeon X5670 @ 2.93
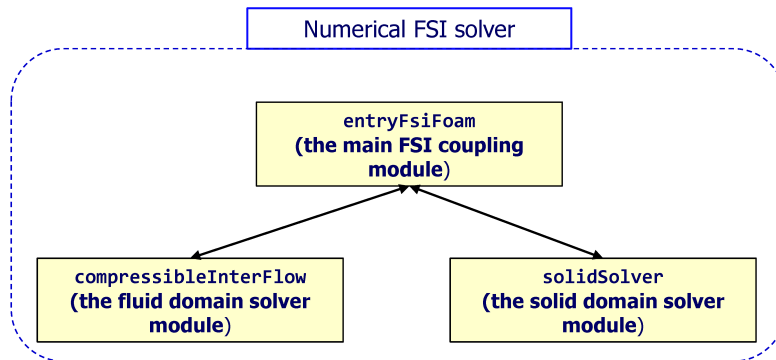
Figure 3.6: Conceptual diagram of the numerical fluid-structure solver developed in the present work; The arrows show the data exchange directions between the components of the solver package

GHz CPUs. Accordingly, the current parameter study with nearly 120 simulation cases would not have been feasible to be done in full 3D form, and therefore all the simulation cases, including the validation tests, were carried out in 2D form.
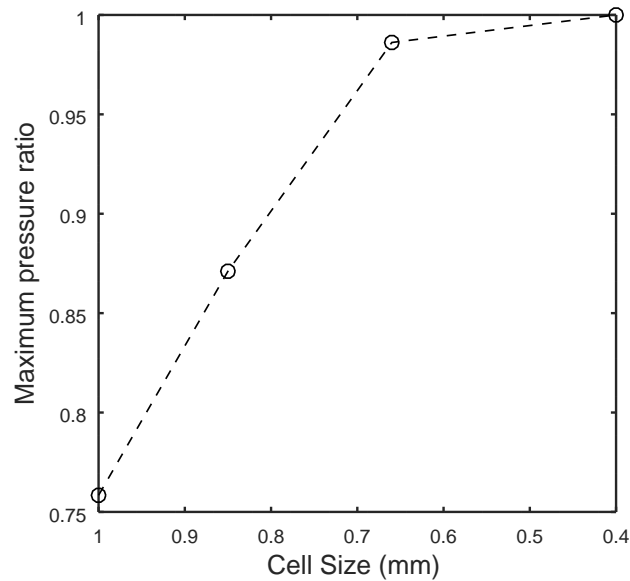
Figure 3.7: Ratio of peak pressure to the peak pressure of the finest mesh model versus the fluid cell size near the interface obtained from the present mesh sensitivity study.

3.5.3 Validation of the numerical implementation

There is no experimental data available on the interaction of aerated water with a flexible structure. Therefore, the published results of two different experiments were used to test the performance of numerical model: experiments reported in Faltinsen et al. (1997)

involved the interaction of a flexible square plate with pure water in drop impacts, and Ma et al. (2016) experiment investigating entry of rigid square plate into aerated and pure water.

Validation test 1, flexible plate water entry

In their physical experiments, Faltinsen et al. (1997) studied the free-fall water entry of a flat rectangular steel plate with $1000mm \times 500mm \times 8mm$ dimensions. The plate was attached at the two ends of its $500mm$ span to ballast weight plates. The end connections had a controlled rotating stiffness. The total mass of the drop rig, including the plate and attached mass, was $500kg$. The plate was dropped against calm water as well as regular wave crests with a variant curvature radius from $1.5m$ to $21m$. The available measurement data was from the drop tests against wave crests of a $10.2m$ curvature radius. However, as Faltinsen et al. (1997) reported, the measurement results of drop tests against a water surface with such a large curvature radius were significantly close to that of the ones carried out against calm water. However, in order to approximate better the experimental condition, the initial water surface in the current simulation was set to curvature with a 10.2 m radius, while the whole fluid domain's initial velocity was set to zero. Since the whole simulation occurs in a very short time-span of nearly 0.03 s, the water surface's deformation before the impact due to gravity force is negligible. The 2D numerical model of the dropping rig is depicted in Figure 3.8. One numerical pressure probe and one numerical strain gauge mounted at the middle of the bottom of the plate bottom recorded the evolution of the time-dependent pressure and strain. Like the physical model, two ends of the plate are connected to a stiff plate at the top, which is also used as an attached mass to set the total mass of the dropping rig model per unit area to $1000kg/m^2$, which is the same as in the experiment. The thickness and length of the connecting plates of the model were determined in a way to give end conditions to the model in the same way as in the experiment. The impact velocity of the dropping simulation was $3m/s$.
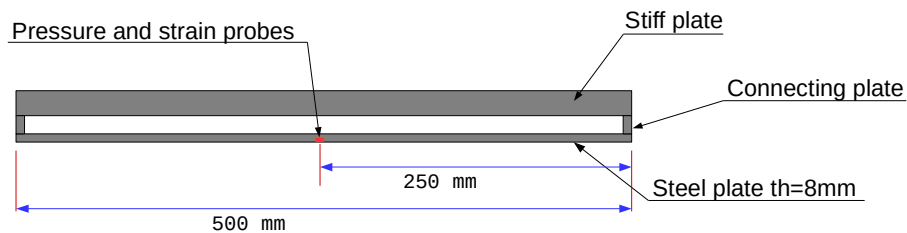
Figure 3.8: The 2D plate model in the numerical simulations according to the experiments of Faltinsen et al. (1997).

Figure 3.9 illustrates a comparison of the results from the experiment report and present

numerical simulation. The pressure evolution at the middle of the plate's bottom is depicted in the left plot and the middle plate bending strain time series are drawn in the right plot. In the pressure time series of experiments, a very sharp peak can be noticed at first sight, which has a very short duration of 0.2 milliseconds. The numerical model did not capture this sharp peak. However, Faltinsen et al. (1997) remarked that these very sharp pressure peaks "can not be treated deterministically," and they are not relevant in the prediction of maximum strains. Apart from this sharp peak, the numerical model has generally fair agreement with the experimental data, and overall duration and values of impact load and the subsequent negative pressure loading are reasonably similar in both results.

Concerning the strain time series, the strain values of the first half period in both numerical and experimental results are in good agreement, and numerical simulation has predicted a maximum strain value close to the experimental data. The duration of the second half period in the experimental result becomes shorter than the first half period. The difference may be explained by the effect of cavitation and ventilation, as stated by Faltinsen et al. (1997). In the present numerical model, as may be seen in Figure 3.10, a relatively large volume of air is trapped beneath the plate at the time of the plate's touchdown, and the plate's deformation along with the two-dimensional setup has intensified this phenomenon in the simulation. Therefore, a relatively large pocket of air is compressed and expands again on the second half period of the plate's oscillation and does not let the plate to oscillate on its own natural period. This can be seen obviously in the flat part of the negative side of strain time history in numerical data.
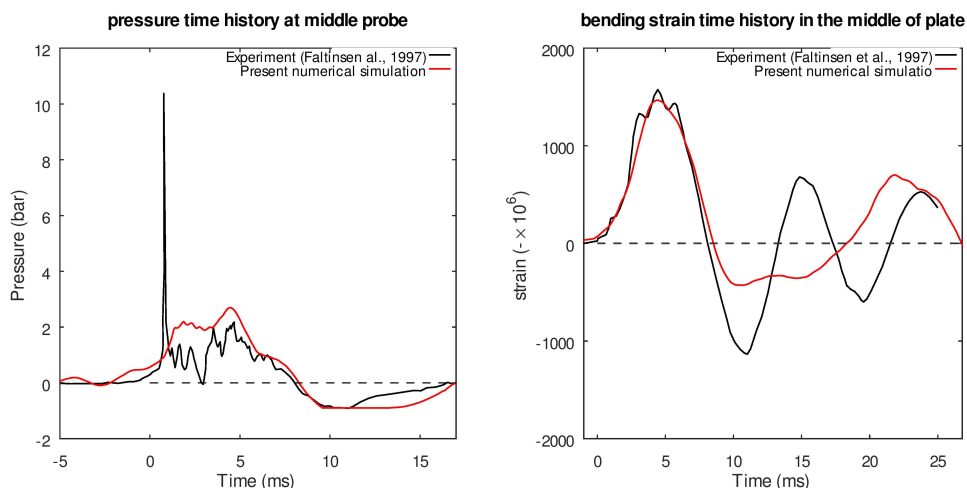
Figure 3.9: Comparison of Faltinsen et al. (1997) experimental pressure time series (left) and strain time series (right) to experimental results with own numerical simulations of this study.

Figure 3.10: Formation of air cushion at the beginning of impact in numerical model. The scenes are from (a) 2 ms before the impact, (b) at the time of impact, and (c) 8 ms after the impact.

Validation test 2, aerated and pure water entry of a rigid flat plate

This set of simulations were performed in the second validation work in order to check the results of the model when the water is modeled as a bubbly fluid. We tried to simulate the physical experiments carried out by Ma et al. (2016). In their setup (Figure 3.11), a mass composed of a $0.25m \times 0.25m$ rigid flat plate and two driver plates was dropped freely into a water tank. Five miniature pressure transducers on the impact plate, one in the center and four in $15mm$ distance from the middle of plate sides, measured the pressure values during impact incidents. Here in the numerical simulation, the setup is two-dimensional. The mass of the impactor per unit area is set to $512kg/m^2$, which is equal to the impactor mass of $32kg$ in the experiment. The impact velocity is set to $5.5m/s$. At the bottom of the experiment tank, under the dropping area, a bubble generator was installed to produce homogeneous aerated water with the determined air fraction values. In the numerical simulations similar to the experiments, the water was modeled as pure as well as aerated with an air fraction of $\beta = 0.008$.

First, the two numerical flow models are examined in the event of plate entry into pure water. Figure 3.15 presents the pressure time series at middle and side probes in the numerical model and experimental data. Ma et al. (2016) observed that in the impact
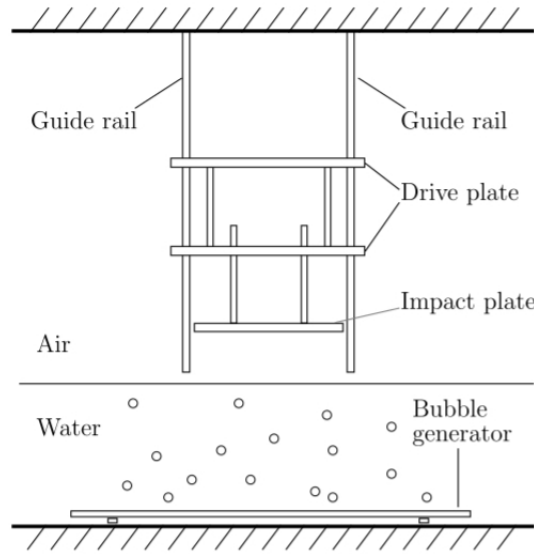
Figure 3.11: Flat plate water entry experimental set-up (from Ma et al. (2016)).

pressure evolution, three stages could be noticed, particularly in the middle of the plate, (i) first a high-pressure loading, (ii) fluid expansion induced low sub-atmospheric pressure, and (iii) a weaker secondary loading. That whole process is happening in a very short time span of fewer than *10* milliseconds. This trend is also remarkably noticeable in the pressure time series resulted from the numerical model (Figure 3.12). In the middle probe, numerical pressure starts to rise earlier and reaches a plateau of about 0.55 *bar* for near *0.5 ms* before rising to the high-pressure loading. This primary loading happens because the plate is initially positioned at the lowest possible elevation near the still water surface ($d_I = 2\,cm$) in order to lower the effects of mesh deterioration due to the movement of the plate and subsequent mesh deformation. However, this has not affected the actual shock loading process and is tolerable. As Table 3.2 shows, the numerical model has a high-pressure shock loading with a peak value significantly close to the experimental results at middle and side probes. The table shows the average peak pressures of the 4 side probes in the experiment. The life-span of the shock loading is nearly 20% wider in the numerical model.

Table 3.2: The peak pressures and duration of shock loading at middle and side probes in pure water entry case.

	Mid. probe p_{max} (bar)	Side probe p_{max} (bar)	Impact pressure time span at mid. probe (ms)	Impact pressure time span at side probe (ms)
Numerical simulation	22.4	10.2	2.4	2.3
Experiment	22.2	9.0 (average)	2 (average)	1.6 (average)

After the high-pressure loading, the compressed trapped air starts to expand, which causes
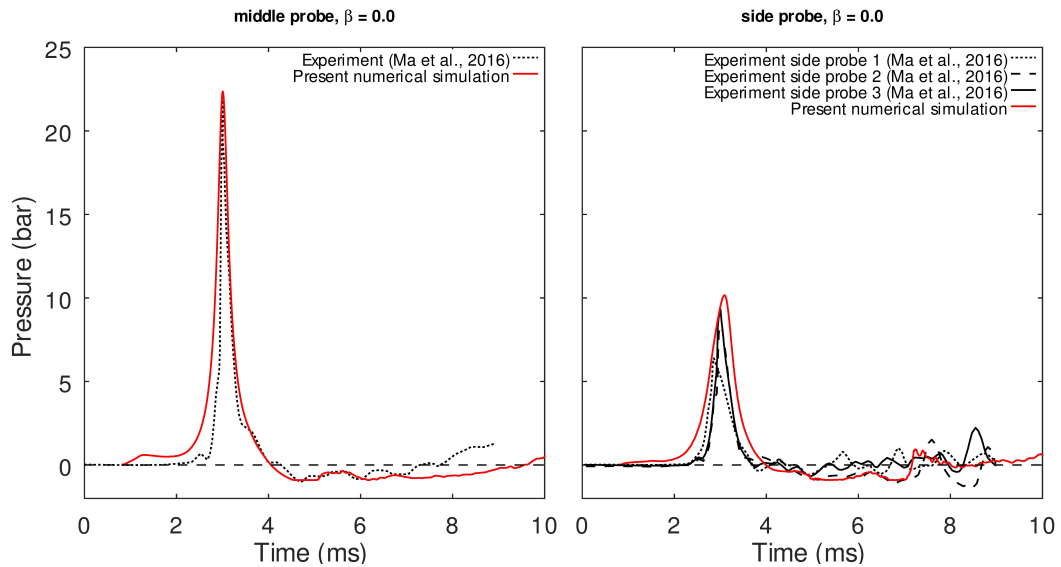
Figure 3.12: Pressure time-series at middle probe (left) and side probe (right) for pure water entry.

a sub-atmospheric pressure underneath the plate. This low-pressure loading at the middle probe lasts for 3.5 ms to 3.7 ms in the experiments and 5.5 ms in the numerical simulation. The duration of fluid expansion loading at side probes was 3.7 ms in the experiment and 3.2 ms in the numerical simulation.

In figure 3.13, the simulation results with aerated water of 0.8% air fraction are compared with the experimental data. In the middle probe, the peak pressure values are very close, but the numerical model's rising time is significantly higher. In the middle probe, the peak pressure value resulted from the numerical model is reasonably close to that of the experiment. The significant difference is that in the middle probe, the pressure rise time is significantly longer; This can be explained by the fact that in the numerical model, the position of the plate is exactly horizontal and that in addition to the two-dimensional set-up increase the effect of air cushioning which reduce the peak pressure and increase the rising time. The values of peak impact pressures and their time spans are listed for aerated water entry cases for numerical and experimental models in Table 3.3. The significant point is that the time series of side probes in the experiments is not synchronous and displays different variations due to water surface disturbance and other practical conditions. However, the numerical model's average peaks and duration have a fair agreement with the experimental data. Another crucial point is that the sub-atmospheric pressure loading is much weaker in the aerated water entry experiment and the numerical model also captures this trend.

Table 3.3: Peak pressures and duration of impact loading at middle and side probes in aerated water entry case.

	Middle probe p_{max} (bar)	Side probe p_{max} (bar)	Impact pressure time span at middle probe (ms)	Impact pressure time span at side probe (ms)
Numerical simulation	5.0	4.5	3.0	3.6
Experiment	6.3	5.3 (average)	4.1 (average)	3.2 (average)
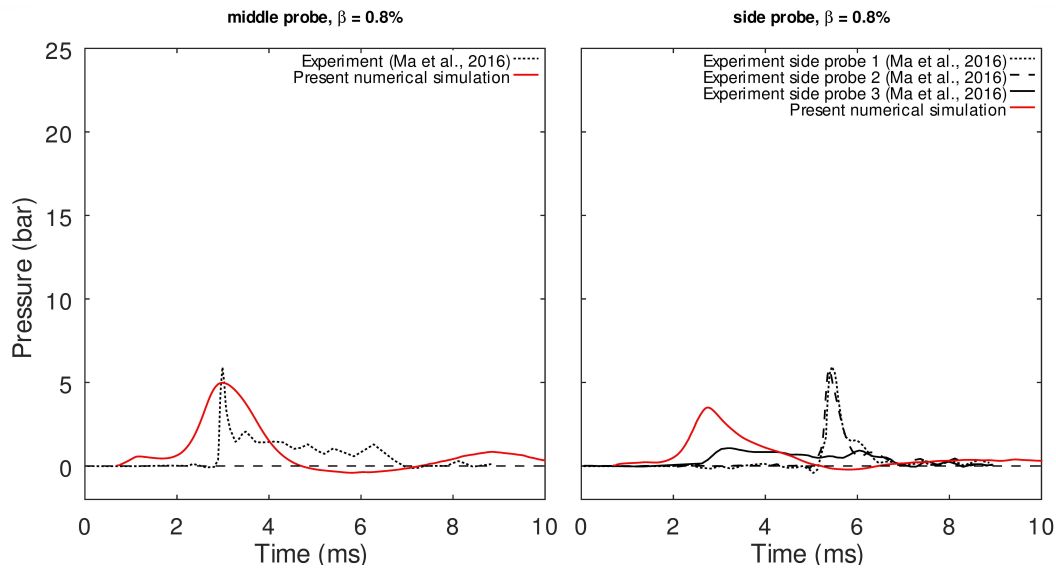
Figure 3.13: Pressure time series at middle probe (left) and side probes (right) for aerated water entry with 0.8% air fraction.

Conclusion on validation

In the first try of applying the present numerical implementation in water entry simulations, a mesh sensitivity study was carried out, which has shown that the variation of pressure field requires a very fine mesh in order of $0.4\,mm$, to obtain accurate results. This is predictable since water entry incidents have induced very steep pressure variations both in time and space in experimental investigations (Ma et al., 2016). The mesh sensitivity study revealed a significant limitation for the current work to carry out 3D simulations. Therefore, the validation simulations were performed in 2D domains.

In the first validation case, the numerical model's performance to capture the physics of hydroelasticity during a water entry simulation was studied. The present numerical model has shown reasonable agreement with the experimental data on essential trends of the evolution of strain and pressure, such as the duration of impact, maximum strain, overall pressure amplitudes, duration, and value of negative-pressure loading. The 2D setup of the

simulation enhanced the volume of the entrapped air between the plate and water surface, which altered the plate's response during the expansion phase of the impact, after the main slamming load phase. The plate end conditions in the setup have also enhanced the air entrapment, and if the model plate had free ends, this adverse effect would be much less intense.

In the second validation case, the present numerical implementation successfully showed the three stages of impact loading in case of pure water entry (the shock load, sub-atmospheric loading, and second pressure peak). It has also successfully captured the major effects of aeration, which were observed in the experimental investigation of Ma et al. (2016), such as elongation of impact span, reduction of the peak, and expansion loading. The time spans and pressure values were also in good agreement with the experimental results. Here, the adverse effects of excessive air entrapment were not observed since the plate model was rigid.

Both validation cases showed that the overall capabilities of the present numerical tool to capture the roles of aeration and fluid-structure interaction in the physical evolution of slamming are acceptable, and it can be applied for implementing the next work packages of the present study.

Summary chapter 3

- A comprehensive review and analysis of the state-of-the-art numerical methods were carried out, and a combination of proper numerical methods was selected and implemented on the C++ numerical platform of OpenFOAM. This is the first time that such an application tool is developed to simulate the interaction of elastic objects with compressible fluid (aerated/pure water) with a free surface, particularly in water entry slamming.

- A mesh sensitivity study and two validation cases were implemented. The mesh sensitivity study revealed that the numerical grid near the impact area should be as thin as 0.4 mm to obtain accurate data of the fluid variables, which lead to the decision to implement the simulations in a 2D setup.

- In the first validation case, the numerical model's ability to capture the physics of hydroelasticity during a water entry simulation was investigated. The numerical model has shown reasonable agreement with the experimental data on essential trends of the evolution of strain and pressure during the impact time, with some negligible differences occurring in the second half period for the strain time series, which can mostly be attributed to the 2D set-up of the simulation. In the second water entry case, the numerical model successfully showed the three stages of impact loading in the case of pure water entry (shock load, sub-atmospheric loading, and second pressure peak), and the overall capability of the numerical tool to capture the effect of aeration on the fluid-solid interaction problem seems acceptable.

4 Numerical study of pure/aerated water entry of elastic plates

As explained in chapter 2, the case of a flat plate slamming onto a calm water surface is similar to the local effects of slamming cases in the real world, in which the solid body and the water surface are nearly parallel to each other before the impact. Chapter 4 presents the first set of numerical investigations carried out in this study, focusing on the interconnected effects of hydroelasticity and aeration on the characteristics of impact pressure and forces as well as the responses of a flat plate during pure and aerated water entry slamming events. In the following section, the set-up of the systematic parameter study is presented, and the results of the performed simulations and following data analysis are discussed next. Finally, the main conclusions from the investigation are drawn in the last section of the chapter.

4.1 Numerical simulation setup

A comprehensive set of 114 numerical simulations was designed and implemented to study the feedback mechanism of hydroelasticity and aeration on the impact loading and structural responses of flat plates during a water entry incident. The simulations consist of an elastic flat plate with an initial velocity and zero deadrise angle entering an initially calm water tank in a free-fall mode (Figure 4.1). The water may be pure or aerated. The simulations were configured in five series S1-5 with individual impact velocity v_I, length of impact plate l, and mass per unit area m_a for each series, as listed in Table 4.1. Within each series, four different aeration ratios $\beta = 0.0\%$, 0.5%, 5.0%, and 10.0%, and six plates with 1st dry eigenfrequencies of the order of 152 Hz, 202 Hz, 254 Hz, 300 Hz, 502 Hz, and 3100 Hz were investigated. The eigenfrequency was varied by changing the plate's thickness representing the degree of plate flexibility, and the plate with the highest eigenfrequency can be assumed as a semi-rigid plate. All the plates had the same material properties of steel (Modulus of elasticity $E = 2.1 \times 10^{11} Pa$, Poisson's ratio $\nu_s = 0.3$). The plates' end conditions were free, as the results of the first validation case showed that the pinned end condition significantly increases the volume of entrapped air, and the resulting cushioning effect might overshadow the effect of aeration.

The slamming loads and plate responses were recorded utilizing the following numerical probes

1. An array of pressure probes at plate bottom with 1 cm intervals recorded the local pressure values at every step of the simulations.
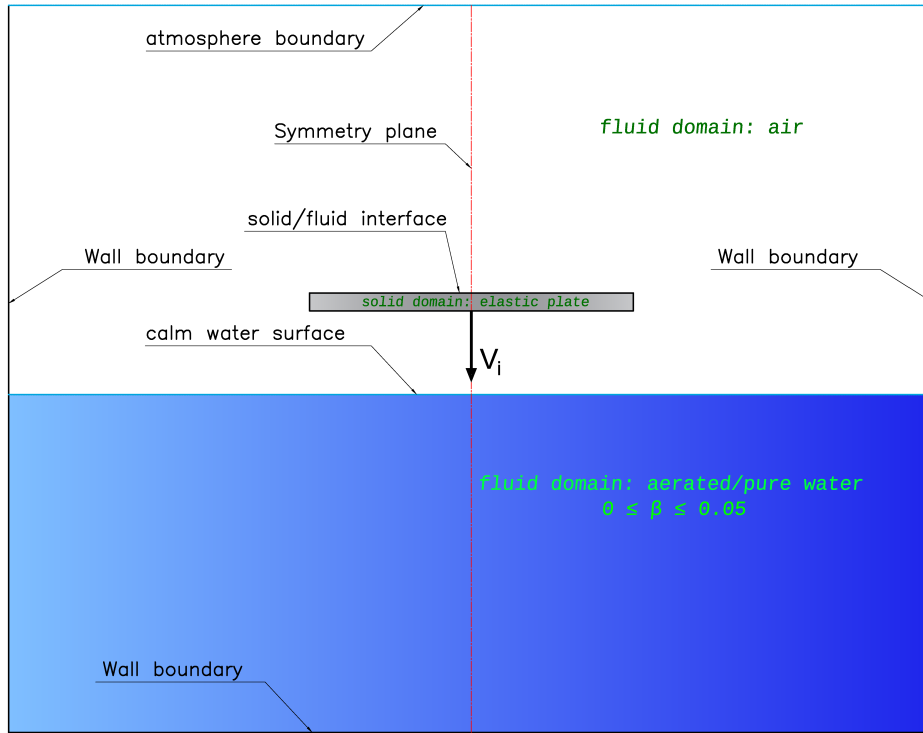
Figure 4.1: Schematic representation of 2D water entry of a flat plat including initial and boundary conditions.

Table 4.1: Simulation series and their constant parameters.

Series name	v_I (m/s)	m_a (kg/m^2)	l (mm)	Dry eigenfrequencies (Hz)	Aeration level β $(\%)$
S1	1.5	300	250	152, 202, 254, 300, 502, 3100	0, 0.5, 5, 10
S2	3.5	300	250	152, 202, 254, 300, 502, 3100	0, 0.5, 5, 10
S3	5.5	300	250	152, 202, 254, 300, 502, 3100	0, 0.5, 5, 10
S4	5.5	300	400	152, 202, 254, 300, 502, 3100	0, 0.5, 5
S5	7.5	300	250	152, 202, 254, 300, 502, 3100	0, 0.5, 5, 10

2. The total force probe recorded the total force calculated from the integral of pressure around the plate.

3. The plate response was recorded through a bending strain probe in the middle of plate bottom.

Boundary conditions and numerical schemes

To reduce the computational time, a symmetry plane boundary condition was applied in all the simulations (cf. Figure 4.1). The boundary conditions for all variables are summarized in Table 4.2.

Table 4.2: Boundary conditions for solid and fluid variables.

Boundary name	$\boldsymbol{u}_s$	$\boldsymbol{v}_f$	p	α_1	α_2
Wall	-	Fixed value, $\boldsymbol{0}$	Zero gradient	Zero gradient	Zero gradient
Solid-fluid inter-face	Traction-displacement	$\dot{\boldsymbol{u}}_s$	Zero gradient	Zero gradient	Zero gradient
Atmosphere	-	Free inlet/outlet	Fixed value, $10^5 Pa$	Zero gradient	Zero gradient

The applied temporal and spatial discretization schemes as well as solving algorithm of domains are the same as described in detail in section 3.4.

4.2 Analysis of the impact loads

Figure 4.2 presents the time histories of pressure in the middle of the plates during the impact incident. Each plot illustrates the time histories for three plates with different natural frequencies, the most flexible plate (f = 152 Hz), the semi-rigid plate (f = 3100 Hz), and one plate with a medium eigenfrequency (f = 300 Hz). The left plots result from pure water entry simulations, while the right plots are the results of aerated water entry cases with a 0.5 % aeration level. Results are provided for series S1, S3, and S4 in order to analyze the effect of impact velocity (S1 and S3) and plate length (S3 and S4). The pressure time histories resemble those of the experiments of Ma et al. (2016), showing a single peak followed by a sub-atmospheric loading and a secondary minor peak. It can be noticed that only a small amount of aeration (0.5 %) causes a significant drop (up to 73 %) in the peak pressure for all cases. The mean peak impact pressure in non-aerated cases of series S3 is 25 times higher than that in series S1, while these ratios are considerably lower (9.8) in the aerated cases. This will be discussed further down below in this section.

Another mattering point is the effect of the plate flexibility on the peak pressure. To have a better view on that, the relative peak pressure, normalized with the corresponding semi-rigid case, is drawn against the plate eigenfrequency for all cases with $\beta = 0\%$, $\beta = 0.5\%$, and $\beta = 5\%$ in Figure 4.3. One major feature noticeable observing the plots is that with the involvement of aeration, the effect of plate flexibility on peak pressure declines significantly to the degree that with $\beta = 5\%$ (Figure 4.3, right), the difference between ratios becomes negligible. Considering the pure water entry (Figure 4.3, left), in all series except for series S5, the peak pressures generally increase with decreasing flexibility, and there seems to be a linear trend in the relation between the peak pressure and the logarithm of the natural frequency. In series S5, the impact velocity of plates ($v_I = 7.5\,m/s$) is considerably higher than for the other series', and it seems that in high-speed vertical entry slamming, the plate's flexibility is relatively insignificant for the impact peak pressures. The variability of the peak pressure due to plate stiffness variation is considerably higher in simulation series
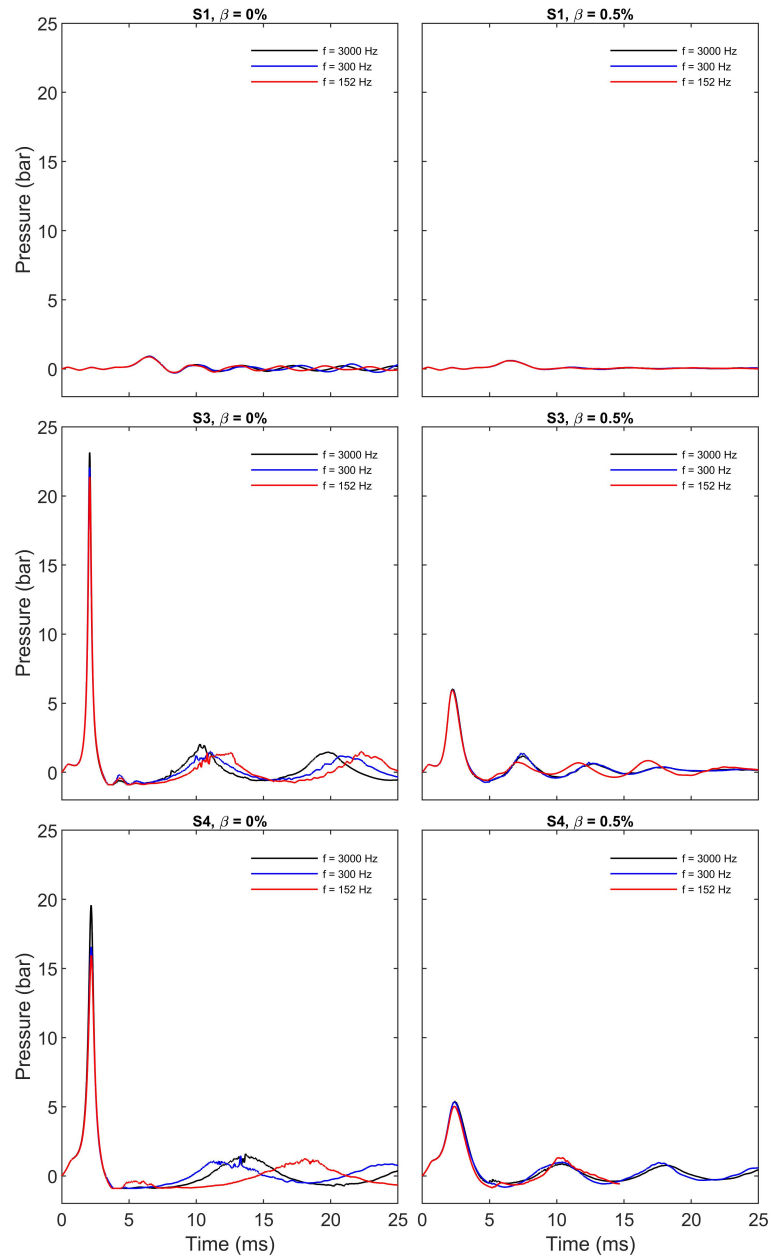
Figure 4.2: Pressure time histories at middle probe for pure and 0.5 % aerated water entry.

S4, in which the length of plates was 60 % larger than in the other series. This implies that the plate length plays a significant role in determining the share of hydroelasticity in water entry impact loads.
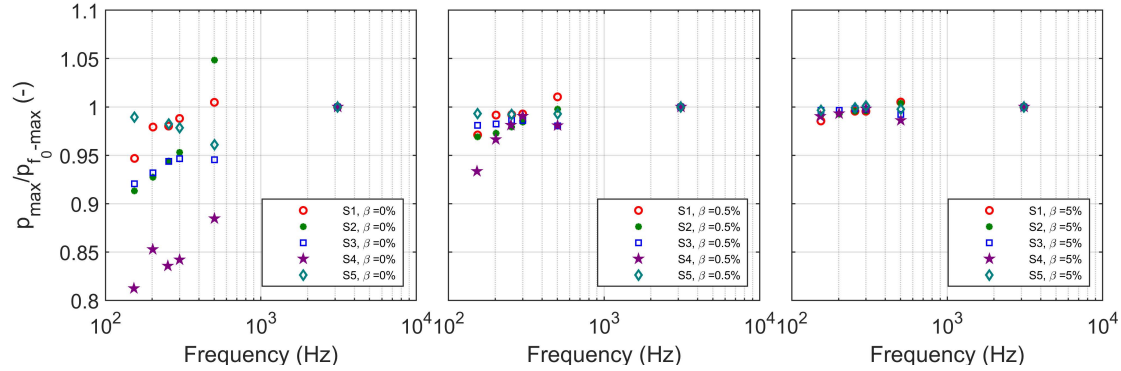
Figure 4.3: Ratio of peak pressure values of all cases to the corresponding semi-rigid case as a function of 1st eigenfrequency, for cases with non-aerated water, $\beta = 0.0$ (left), and aerated water with $\beta = 0.5\%$ (middle), and $\beta = 5\%$ (right).

In Figure 4.2, further points of interest are the duration and magnitude of negative pressure and the secondary pressure peak, which could affect the response of plates after the first period of vibration, as will be discussed later in section 5.2. The negative pressure duration in pure water entry cases varies considerably with the plate stiffness and generally, with decreasing stiffness the negative pressure time increases. It should be mentioned in this context that, for the sake of numerical stability, the minimum absolute fluid pressure had to be limited to 10^4 *Pa* (i.e. -0.9 *bar* relative to atmospheric pressure), which can be observed in the plots, particularly for the pure water entry in series S4, where the pressure does not go beneath this value. In series S4, the variation of secondary pressure peak due to the variation of eigenfrequencies is significant, while it is trivial in the S3 series. Since plate length is the only parameter that varies between the two series, it could be assumed that this higher variation of the second pressure peak results from the increasing plate length.

Another important aspect of water entry of a horizontal flat plate in the presence of aeration and hydroelasticity is the dependence of peak pressures and forces on impact velocity, which can be seen in Figure 4.4. In the left graph, the peak pressure values of all simulations, with pure water as well as aerated water, are plotted against impact velocity. Some variations are noticeable for the same impact velocities due to the different plate flexibilities, as discussed above. Despite these variations, a clear trend of increasing peak pressure with increasing impact velocity can be observed for all aeration levels, indicating a functional relationship between them. This is determined by an interestingly simple power-law function, taking the compressibility parameter and the speed of sound into

account in order to consider the effect of aeration:

$$p_{max} = k_p \rho v_I^{1/3 \ln c}, \tag{4.1}$$

where c is the speed of sound inside the aerated water (Equation 4.1); ρ is the water-air mixture density; and k_p is a coefficient defined by:

$$k_p = 21.27 + 12.46 e^{-32.098\beta}. \tag{4.2}$$

As the same trend can also be observed for the peak slamming forces per unit area, which are shown in the right graph of Figure 4.4, a similar power-law function can be defined here:

$$F_{max} = k_f \rho v_I^{1/3 \ln c}, \tag{4.3}$$

where F_{max} is the maximum value of the impact force per unit area and the coefficient k_f depends on the aeration level in the following form:

$$k_f = 24.3 - 45.7\beta. \tag{4.4}$$

Since certain parameters, such as plate length, mass, etc., are excluded here, the above expressions may not be regarded as a general relationship for plates.
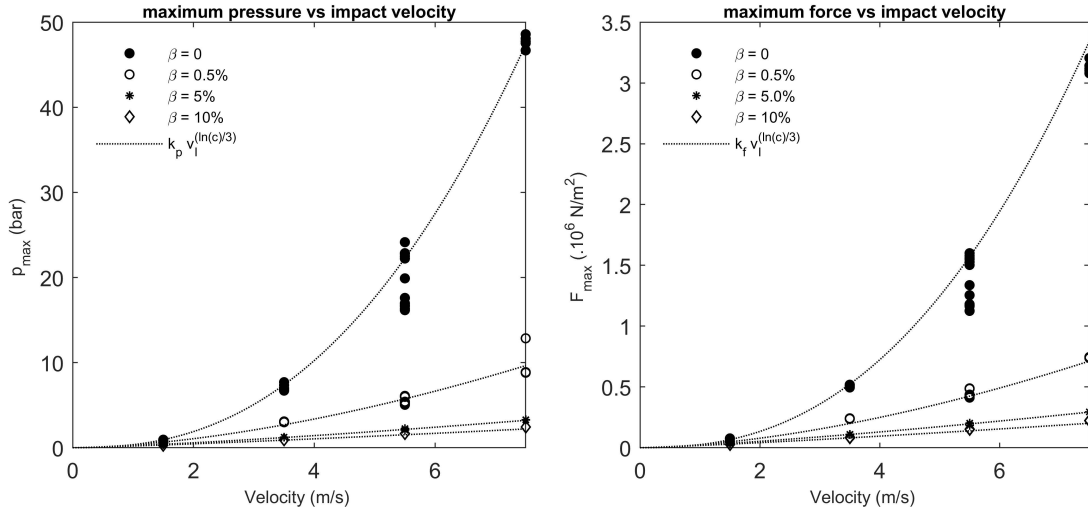
Figure 4.4: Peak slamming pressures (left) and peak slamming forces (right) as a function of impact velocity for all cases with pure and aerated water. The new suggested power-law approximation curves are drawn for every aeration level.

The evolution of the impact pressure distribution along the half length of the plate is

examined next, which is plotted in Figure 4.5 for series S1 and S3 (low and medium impact velocity) with the same aeration rates ($\beta = 0\%$ and $\beta = 0.5\%$) and the same flexibilities ($f = 150\ Hz$, $300\ Hz$, and $3000\ Hz$), as shown in Figure 4.2. The plots in the odd columns of Figure 4.5 represent the non-aerated cases, while the plots in the even columns are the results of simulations with aerated water ($\beta = 0.5\%$). For all cases, the high slamming pressures in the shock loading are very concentrated in a time span of approximately 1 to 2 ms, and in pure water cases, the maximum pressure occurs at virtually all points simultaneously along the length of the plate, while the contours are less symmetric in the aerated cases.

Another noteworthy difference between the results of series S1 and S3 is the effect of aeration on the rising time and drop time of the peak pressure. For series S1, practically no difference in rising time and drop time between the aerated and non-aerated cases can be discerned from the plots in Figure 4.5; whereas, for series S3, both rising and drop time exhibit a significant increase when the water is aerated. One can also see that the expansion of the drop time due to aeration is much larger than the rate of increase in rising time. The mean rising time in series S3, for instance, increases by 28% (from 0.64 ms to 0.82 ms), while the drop time increases by 56% (from 0.9 ms to 1.38 ms).
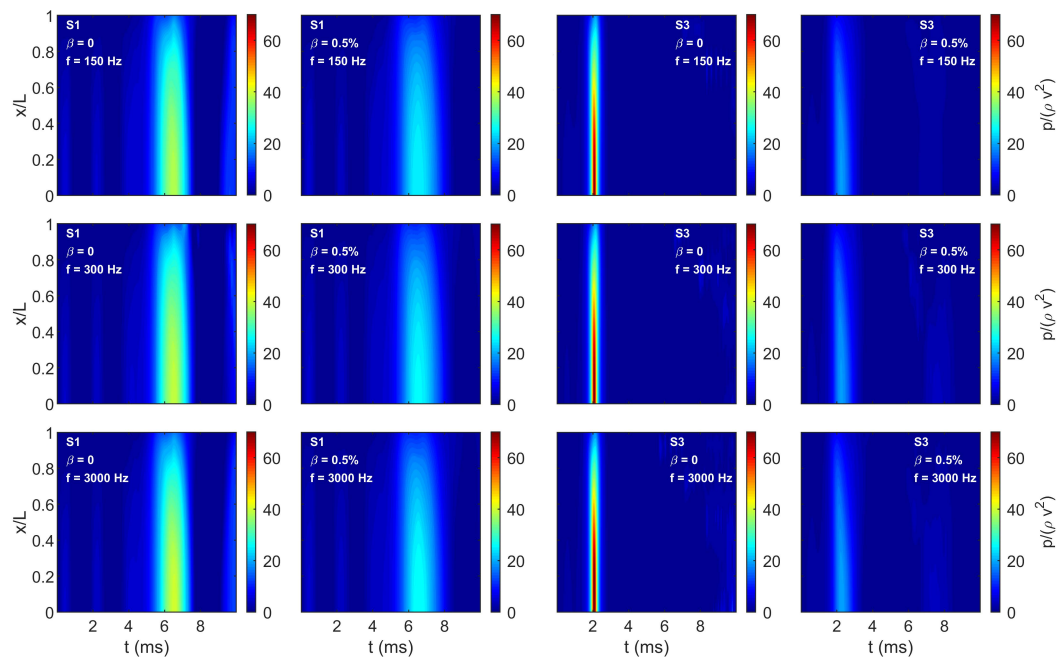
Figure 4.5: Variation of pressure distribution along the half length of the plate in time. The results of water entry of three plates with low middle and high eigenfrequencies in two simulation series are shown. The simulation series, air fraction level and plate eigenfrequencies are marked on each plot.

Figure 4.6 depicts the distribution of dimensionless pressure ($p/(\rho v_I^2)$) along the half length of the plate at the time near to the peak slamming load for all five series with pure water entries (left) and aerated water entries (right) of plates with low, medium and high eigenfrequency. The figure shows that in pure water cases the gradient of the pressure along the half length of the plate is much steeper than in the aerated cases. The trend that was observed in Figure 4.2 is also noticeable here, as in aerated cases the pressure curves of different plates are almost indistinguishable, which implies that the impact forces in the aerated water entry cases are insensitive to the elasticity of the plate. In order to examine this further, the maximum values of the dimensionless slamming forces ($C_s = F_{max}/(\rho v_I^2)$) are plotted against the first eigenfrequencies in Figure 4.7. From the plot, it is obvious that, in the aerated cases, the variation of C_s is very small and negligible. On the other hand, for the pure water cases, the smaller eigenfrequencies show higher variation of C_s and this effect increases with the plate length, as seen by the results of series S4.

Figure 4.6 depicts the distribution of dimensionless pressure ($p/(\rho v_I^2)$) along the half-length of the plate at the time near to the peak slamming load for all five series with pure water entries (left) and aerated water entries (right) of plates with low, medium and high eigenfrequency. The figure shows that in pure water cases, the gradient of the pressure along the plate's half-length is much steeper than in the aerated cases. The trend that was observed in Figure 4.2 is also noticeable here, as in aerated cases, the pressure curves of different plates are almost indistinguishable, which implies that the impact forces in the aerated water entry cases are insensitive to the elasticity of the plate. In order to examine this further, the maximum values of the dimensionless slamming forces ($C_s = F_{max}/(\rho v_I^2)$) are plotted against the first eigenfrequencies in Figure 4.7. From the plot, it is evident that, in the aerated cases, the variation of C_s is tiny and negligible. On the other hand, for the pure water cases, the smaller eigenfrequencies show a higher variation of C_s, which increases with the plate length, as seen by the results of series S4.

The peak dimensionless slamming force and the force durations at high-pressure and low-pressure loading intervals for all considered tests cases are summarized in Table 4.3 and Table 4.4, respectively. From Table 4.3, it is obvious that the variation of the peak C_s values due to the different plate flexibilities is greatly reduced in the aerated cases, which follows the same pattern as that observed for the pressure values above. The maximum C_s values are also reduced, on average, by 59% when small aeration of 0.5% is added to the pure water. However, as shown in Table 4.4, at the same time, the duration of the impact loads (T_h) significantly increase between 32% and 54%. This implies that the force impulse, defined as the time integral of the force over the impact duration ($\int_{T_h} F dt$), is probably less affected by the aeration. Figure 4.8 confirms this assumption, presenting the relative force impulse values (force impulse value (I_F) / mean corresponding non-aerated water entry force impulse ($\bar{I}_{F,\beta=0}$)), together with the relative slamming coefficients ($C_s/\bar{C}_{s,\beta=0}$), for the simulation series S1-3. The large reduction of the slamming coefficient, occurring
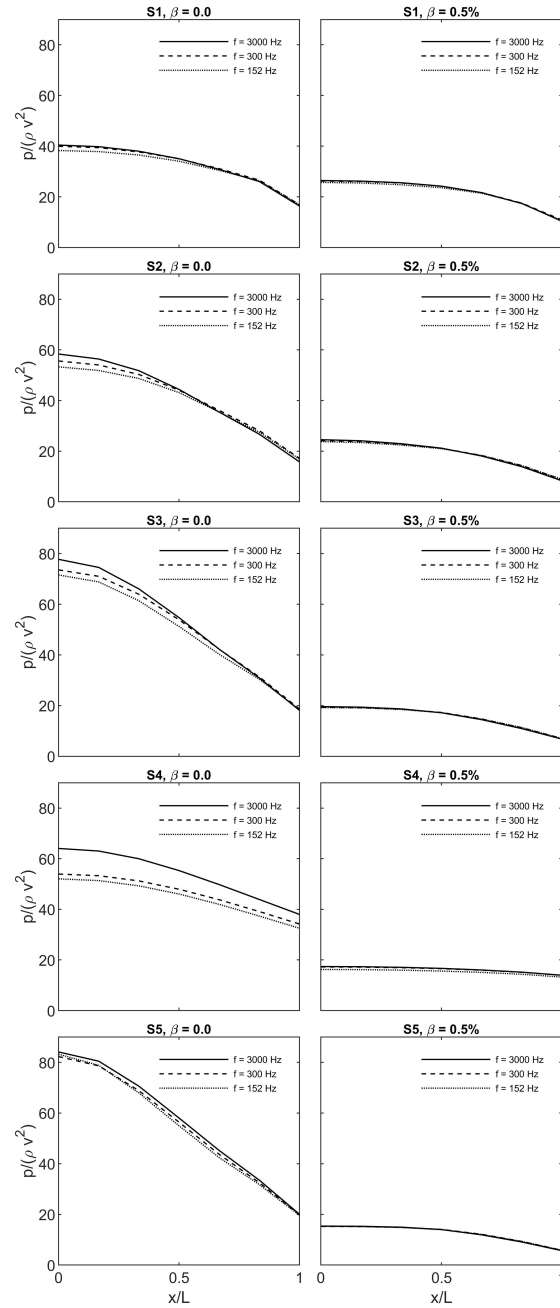
Figure 4.6: Distribution of pressure beneath the plate at the time of peak pressure for simulation series S1 to S5 in cases with $\beta = 0$ (left) and $\beta = 0.5\%$ (right).
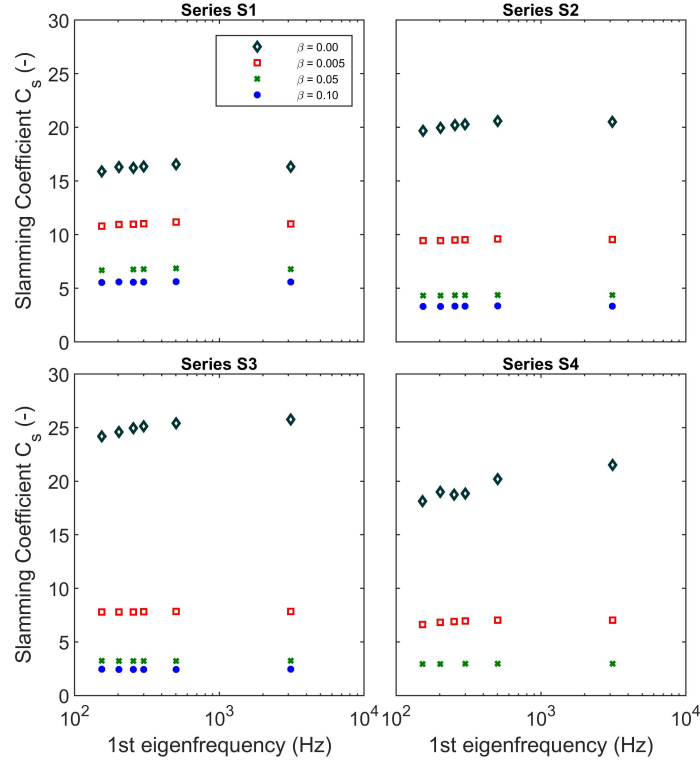
Figure 4.7: Peak slamming force coefficient vs. plate eigenfrequency for series S1 – S4.

at the lowest aeration level, is significantly less for the force impulse values (13% - 25%). Table 4.4 also summarizes the post-impact low-pressure phase lifespans ranges within each simulation series for all of the performed simulations. The duration of the low-pressure phase lasts $1.28 - 1.49$ ms in the S1 series, while it increases to $6.73 - 11.21$ ms in the S5 series, in which the slamming pressure is 57 times higher on average than that in the S1 series. This higher pressure leads to greater contraction of trapped air, which increases the expansion time and makes it more intense.

Table 4.3: Ranges of peak dimensionless slamming force C_s for all simulation series. The values within parentheses show the proportional changes of mean value with reference to the corresponding non-aerated case.

Series name	$\beta = 0$	$\beta = 0.5\%$	$\beta = 5\%$	$\beta = 10\%$
S1 ($v_I = 1.5$ m/s)	$15.9 - 16.3$	$10.8 - 11.1$ (-32%)	$6.7 - 6.8$ (-58%)	$5.5 - 5.6$ (-65%)
S2 ($v_I = 3.5$ m/s)	$19.0 - 20.6$	$9.4 - 9.6$ (-53%)	$4.3 - 4.4$ (-78%)	3.3 (-83%)
S3 ($v_I = 5.5$ m/s)	$24.0 - 25.7$	7.8 (-69%)	3.2 (-87%)	2.4 (-90%)
S4 ($v_I = 5.5$ m/s)	$18.1 - 21.5$	$6.6 - 7.0$ (-65%)	$2.9 - 3.0$ (-85%)	NA
S5 ($v_I = 7.5$ m/s)	$26.7 - 28.7$	$6.4 - 6.5$ (-77%)	2.5 (-91%)	1.9 (-93%)

Table 4.4: Ranges of high-pressure and low-pressure loading duration for all simulation series. T_h and T_l are the durations of high-pressure impact force and sub-atmospheric post-impact force, respectively. The values within parentheses show the percent changes of mean value with reference to the corresponding non-aerated case.

Series name	Variable	$\beta = 0$	$\beta = 0.5\%$	$\beta = 5\%$	$\beta = 10\%$
S1 ($v_I = 1.5$ m/s)	T_h (ms)	$3.1 - 3.2$	$4.1 - 4.2$ (+32%)	$8.6 - 8.8$ (+176%)	$11.3 - 12.3$ (+275%)
	T_l (ms)	$1.3 - 1.5$	$0.3 - 0.7$ (-63.1%)	$0 - 0.4$ (-84%)	$0.17 - 0.49$ (-76.2%)
S2 ($v_I = 3.5$ m/s)	T_h (ms)	2.2	2.9 (+32%)	$7.4 - 8.3$ (+256%)	$10.1 - 11.1$ (+382%)
	T_l (ms)	$3.2 - 3.8$	$1.9 - 2.1$ (-43.5%)	$0.0 - 0.3$ (-96%)	0.0 (-100%)
S3 ($v_I = 5.5$ m/s)	T_h (ms)	1.8	$2.6 - 2.7$ (+47%)	$7.0 - 7.5$ (+303%)	$9.3 - 11.4$ (+475%)
	T_l (ms)	$4.9 - 6.1$	$2.1 - 2.2$ (-61.5%)	0.0 (-100%)	0.0 (-100%)
S4 ($v_I = 5.5$ m/s)	T_h (ms)	2.7	$3.5 - 4.0$ (+39%)	$10.2 - 10.4$ (+274%)	NA
	T_l (ms)	$6.0 - 11.0$	$3.2 - 3.7$ (-59%)	$3.7 - 4.2$ (-53.6%)	NA
S5 ($v_I = 7.5$ m/s)	T_h (ms)	$1.6 - 1.7$	$2.5 - 2.6$ (+54%)	$7.3 - 7.6$ (+351%)	$9.5 - 12.7$ (+573%)
	T_l (ms)	$4.8 - 7.2$	$1.9 - 2.2$ (-66%)	$0.0 - 0.46$ (-96%)	0.0 (-100%)
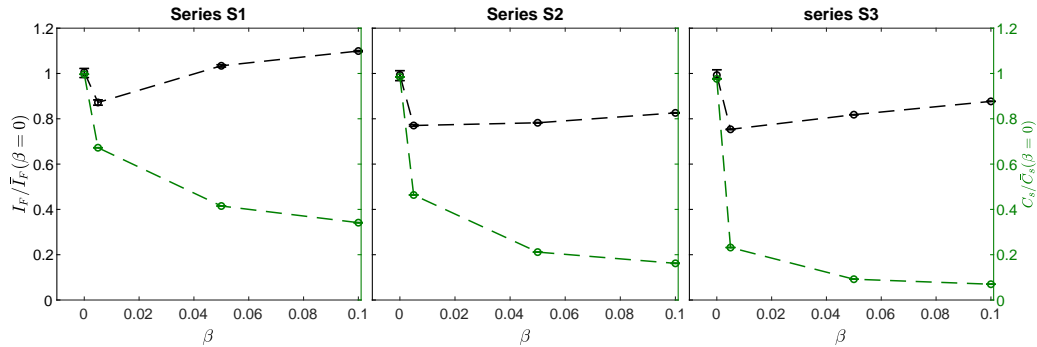
Figure 4.8: Dependence of relative mean impact force impulse I_F and impact force coefficient C_s on aeration level for series S1 – S3.

4.3 Analysis of response strain

The discussion in this section over plate responses focuses on the bending strain in the middle of the plate, where the plate's maximum response during the entry incident occurs. In Figure 4.10, the time series of the bending strain for different aeration levels and different eigenfrequencies are plotted exemplarily for series S3. The other series results are not presented here as they show the same trends and do not add anything to the following discussion. In all cases, the oscillation period does not change by adding aeration, but a phase shift delay is observable in aerated cases, which increases with higher values of air

fraction. It is noteworthy that the maximum absolute strain in pure water cases does not occur necessarily in the first oscillation period. This could be explained by the effect of after-shock pressure oscillations occurring due to the oscillation of trapped air beneath the plate and its interaction with the plate. Aerated water has expectedly a damping effect on the plate oscillation, which increases with increasing the level of aeration. This causes the strain oscillations to dissipate faster than in pure water cases and reduces the maximum strain amplitude. However, in less aerated cases, the maximum strain values are still very close to those in pure water cases in contrast to the ratio of the slamming forces examined above. For instance, the average maximum slamming force for series S3 is reduced by 68.7 %, at only 0.5 % aeration (cf. Figures 4.7 and 4.8), while the average maximum strain is reduced by only 37.5 %. This phenomenon becomes more pronounced with increasing plate flexibility. To better view that, the ratio of the maximum absolute strain in aerated cases to that in pure water cases is plotted as a function of the plate eigenfrequency in Figure 4.9. The highly aerated water entry cases ($\beta = 10\%$) have been omitted as the strain and slamming force ratios are substantially small in those cases. The important point about Figure 4.9 is that in low aerated cases, the aeration may not necessarily cause a reduction in structural responses of plates and other structural forms in general. The main reason may be due to the fact that although the maximum values of the slamming force reduce significantly in an aerated water entry, the duration of the impact load is longer at the same time. This implies that the impact energy may not be reduced as large as the peak pressures and forces in a water entry event.
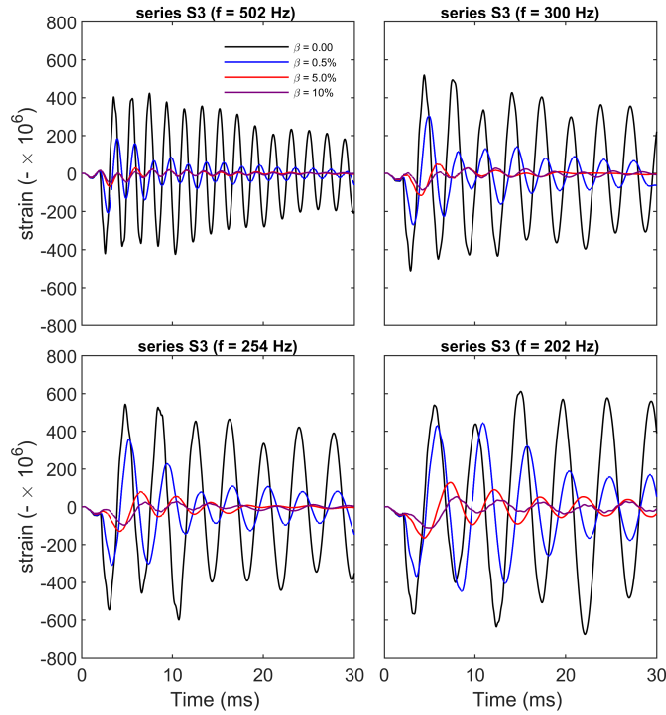
Figure 4.9: Strain ϵ_{xx} time histories in 4 models of series S3 simulations.
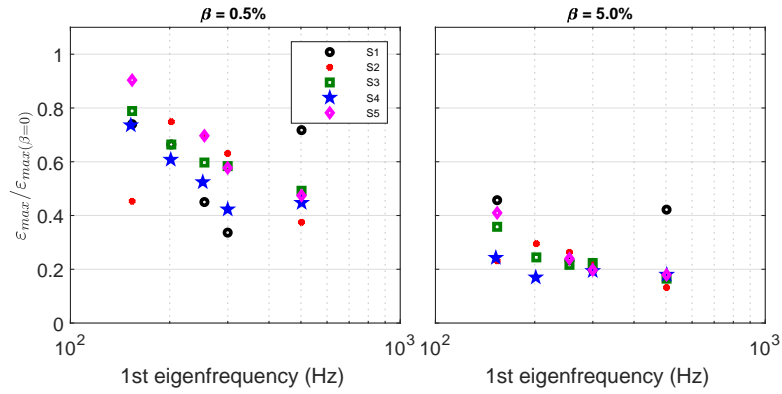
Figure 4.10: Dependence of the ratio of maximum strain in aerated water entry cases to that of the corresponding pure water entry cases to plate flexibility for $\beta = 0.5\%$ (left) and $\beta = 5\%$ (right).

4.4 Conclusions

In the present chapter applying the validated numerical tool, a comprehensive numerical study has been implemented to investigate the interlinked effects of aeration inside water and hydroelasticity on the hydrodynamic impact loading and structural responses during a water entry of flat flexible plates. Observation of the simulation results on the hydrodynamic

loading side reveals that the plate flexibility affects the slamming loads, particularly when the plate's length increases. Another finding in this respect is the effect of aeration on hydrodynamic loads. Aeration has shown to affect the impact loading in two different ways:

1. Only a slight amount of aeration in water reduces the maximum slamming forces significantly, but also elongates the duration of loading, which implies that the impact force impulse may not be affected as much as the maximum forces.

2. The effect of plate flexibility on slamming loads significantly reduces in aerated water and almost vanishes for aeration levels over 5%. This may have important implications for modelling, as it seems in such situations in which water is aerated, e.g., in breaking wave load impact, that there may be no need to use a strong coupling for accurate assessments of hydrodynamic loads.

The peak impact forces/pressures depend on the impact velocity, but also on the compressibility of water, which changes significantly with aeration level. Consequently, a new functional relation in terms of a rather simple power-law approximation has been derived, which fits very well to the present data.

The structural response of a plate in terms of bending strain in the middle of the plate expectedly reacts directly to hydrodynamic loads for stiff structures. With increasing flexibility, resonating effects occur with increasing strain rates and less influence of aeration. This suggests that the significant computational effort of using a strongly coupled numerical model, such as the one proposed here, is also not required for assessments of structural response if the structure is rather rigid.

Summary chapter 4

- This chapter presents a comprehensive numerical study of the impact of aeration and hydroelasticity on slamming loads and elastic plates' structural response during a water entry event.

- An extensive parameter investigation revealed that the structural flexibility of a plate exerts a noticeable effect on slamming loads for pure water entry cases, which almost completely disappears when the water is aerated. This confirms that aeration and hydroelasticity have intertwined effects on the slamming of flat plates.

- The effect of aeration on slamming loads is quite significant. With only 0.5 % air fraction, aeration can substantially reduce the peak slamming forces, but as the load duration increases simultaneously, the force impulse remains almost constant.

- In terms of strain rates, the structural response reacts directly on the hydrodynamic loads for stiff plates and exhibits resonating effects and less influence on aeration levels at higher flexibilities. This suggests that the structural performance in a slamming event must be carefully considered and directly related to loads for very stiff structures. For this purpose, a new functional relation between peak impact forces/pressures and impact velocity in the presence of aeration is suggested within the present study.

5 Numerical study of pure/aerated water entry of elastic cylinders

Cylindrical shell sections, prevalent shapes in marine and coastal applications, have been a major subject of interest in slamming studies reviewed in chapter 2. The feedback mechanism of local hydroelasticity and aeration has been shown to play an essential role in the slamming forces and response of plates in water entry simulations reported in chapter 4. Apart from flat plates, as stated in chapter 2, literature does not offer enough knowledge in this matter when one studies the slamming of cylindrical shell sections. As aimed in chapter 2, the present chapter reports the comprehensive numerical study conducted on the slamming of flexible cylindrical shell sections during aerated/pure water entry events. This chapter starts by describing the set-up of numerical simulations. The data analysis is focused on three major fields, i.e. (i) impact pressure around the cylinder during the slamming event, (ii) inline impact force exerted on the cylinder, and (iii) the response of the cylinder to slamming quantified with the bending strain at the outer surface of the cylinder. The interacting effects of aeration and hydroelasticity on the development of the mentioned fields are investigated in three sections 5.2, 5.3, and 5.4, and finally, the concluding remarks are presented in section 5.5.

5.1 Numerical simulation setup

To study the role of aeration and local hydroelasticity parameters on the slamming loads and local responses of cylindrical shell objects, four groups of 2-dimensional water entry simulations (in total 75 simulation cases) were designed and implemented. The water entry was set to be a free fall incident simulation starting with the cylinder placed at an initial distance d_I from the still water surface and moving with the initial vertical velocity v_I downward toward the water surface. The duration of simulations covered the essential time span of the impact, including the peak loading and the cylinders' peak responses. Figure 5.1 presents the simulation domain concept. Recording the loads and responses during the simulations were implemented by three types of numerical probes described as follows:

1. Pressure probes; The pressure probes were arrayed around the surface of the cylinders from the lowest point 0° to 60°. The angular sequence of pressure probe positions was set to 1° for the interval of 0° to 10°, and 2° for the interval of 10° to 60°.

2. The total force probe recorded the total force resulting from the integral of fluid pressure around the cylinder-fluid interface. The magnitude of shear forces was negligible compared to the pressure forces.

3. Strain gauges; two strain gauges, one at the lowest point of the cylinders and one at 90° point, recorded the cylinder's local responses to the fluid dynamics.
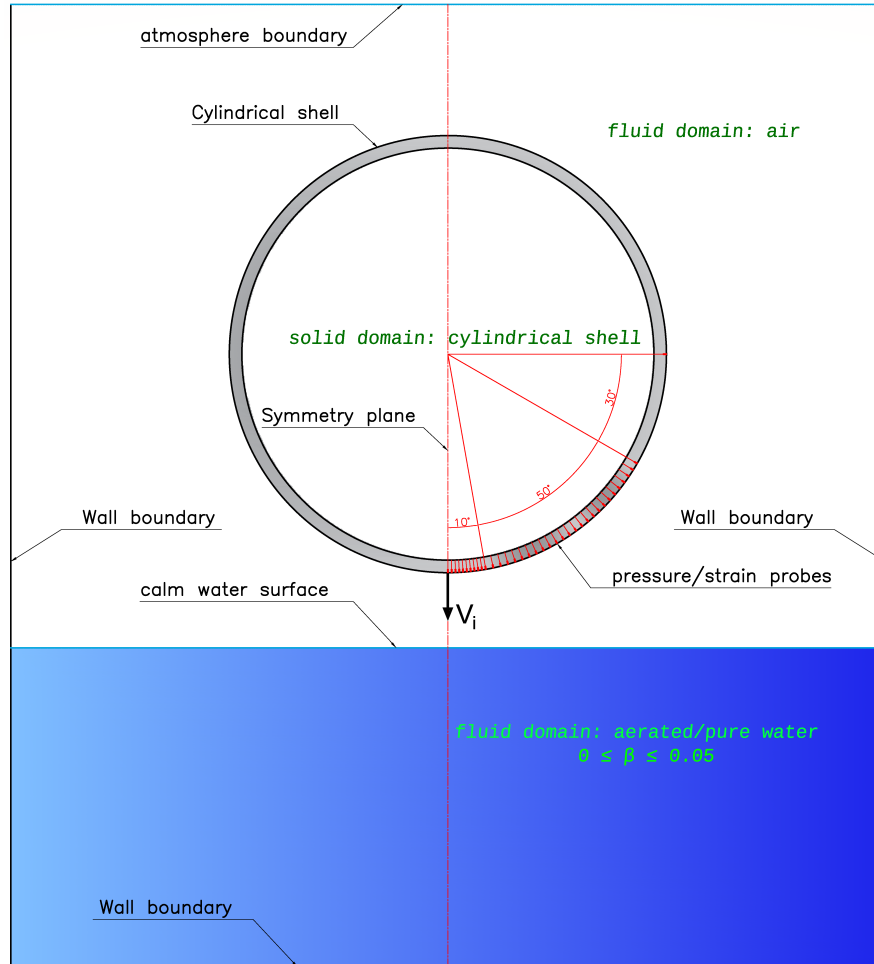
Figure 5.1: Simulation domain concept for elastic cylindrical shell water entry.

The effect of the cylindrical object mass was not in the scope of this work, and therefore the values of mass per length of specimens were kept constant with 100kg/m value. Cylinder diameter (350 mm) was also constant in all simulation cases. The main parameters studied in these series of simulations are the flexibility of cylinders, represented by the first natural frequency (f_1), the impact velocity magnitude (v_I), and the level of aeration (β). The role of the local hydroelasticity is quantified by changing the cylinder's degree of flexibility. To have a broader range of flexibility, a more compliant material, compared to steel, was selected for the cylinders. The cylinders' material properties, which were assumed to be homogeneous, are listed in table 5.1.

In each simulation series, cylindrical specimens with different eigenfrequencies dropped

Table 5.1: Material properties of cylindrical shell specimens applied in the numerical water entry simulations.

Material	Young's modulus (GPa)	Poisson's ratio (-)
Fiberglass	33.2	0.28

into calm water surface with the group's characteristic initial impact velocity v_I. The simulations for each series were implemented with pure water ($\beta = 0\%$) as well as aerated water with three different aeration ratios ($\beta = 0.5\%, 5\%, 10\%$). Table 5.2 presents the specifications of the simulation series. Series S1, S2, and S4 were implemented with five specimens with a broad range of first eigenfrequencies. The cylinders with the highest first eigenfrequency (3060 Hz) can be assumed as semi-rigid cases. To have more detailed data on the flexibility range, four additional cylinder models were used in simulation series S3. It should be noted that the aerated water entry simulations with a 10% aeration level were implemented only with semi-rigid cylinders.

Table 5.2: Simulation series and their constant parameters.

Series name	v_I (m/s)	Number of specimens	Dry eigenfrequencies (Hz)	Aeration level β (%)
S1	1.5	5	28, 68, 117, 400, 3060	0, 0.5, 5, 10
S2	3.5	5	28, 68, 117, 400, 3060	0, 0.5, 5, 10
S3	5.5	9	28, 46, 68, 91, 117, 144, 221, 400, 3060	0, 0.5, 5, 10
S4	7.5	5	28, 68, 117, 400, 3060	0, 0.5, 5, 10

Boundary conditions and numerical schemes

Conditions of the boundaries in the numerical domain (Figure 5.1) are the same as applied in chapter 4 and are given in table 5.3. To reduce the computational time, a symmetry plane boundary condition was applied in all the simulations. The numerical schemes applied in this chapter's simulations were the same as that in the simulations in chapter 4 and are described in chapter 3.

Table 5.3: Boundary conditions for solid and fluid variables.

Boundary name	$\boldsymbol{u}_s$	$\boldsymbol{v}_f$	p	α_1	α_2
Wall	-	Fixed value, $\boldsymbol{0}$	Zero gradient	Zero gradient	Zero gradient
Solid-fluid interface	Traction-displacement	$\dot{\boldsymbol{u}}_s$	Zero gradient	Zero gradient	Zero gradient
Atmosphere	-	Free inlet/outlet	Fixed value, $10^5 Pa$	Zero gradient	Zero gradient

5.2 Analysis of impact pressures

5.2.1 Evolution of pressure distribution

Figure 5.2 shows the important processes that occurred at the early stage of entry impact. The snapshots are taken at time steps of semi-rigid entry simulation in series S3, which had a medium-high impact velocity of 5.5 m/s.
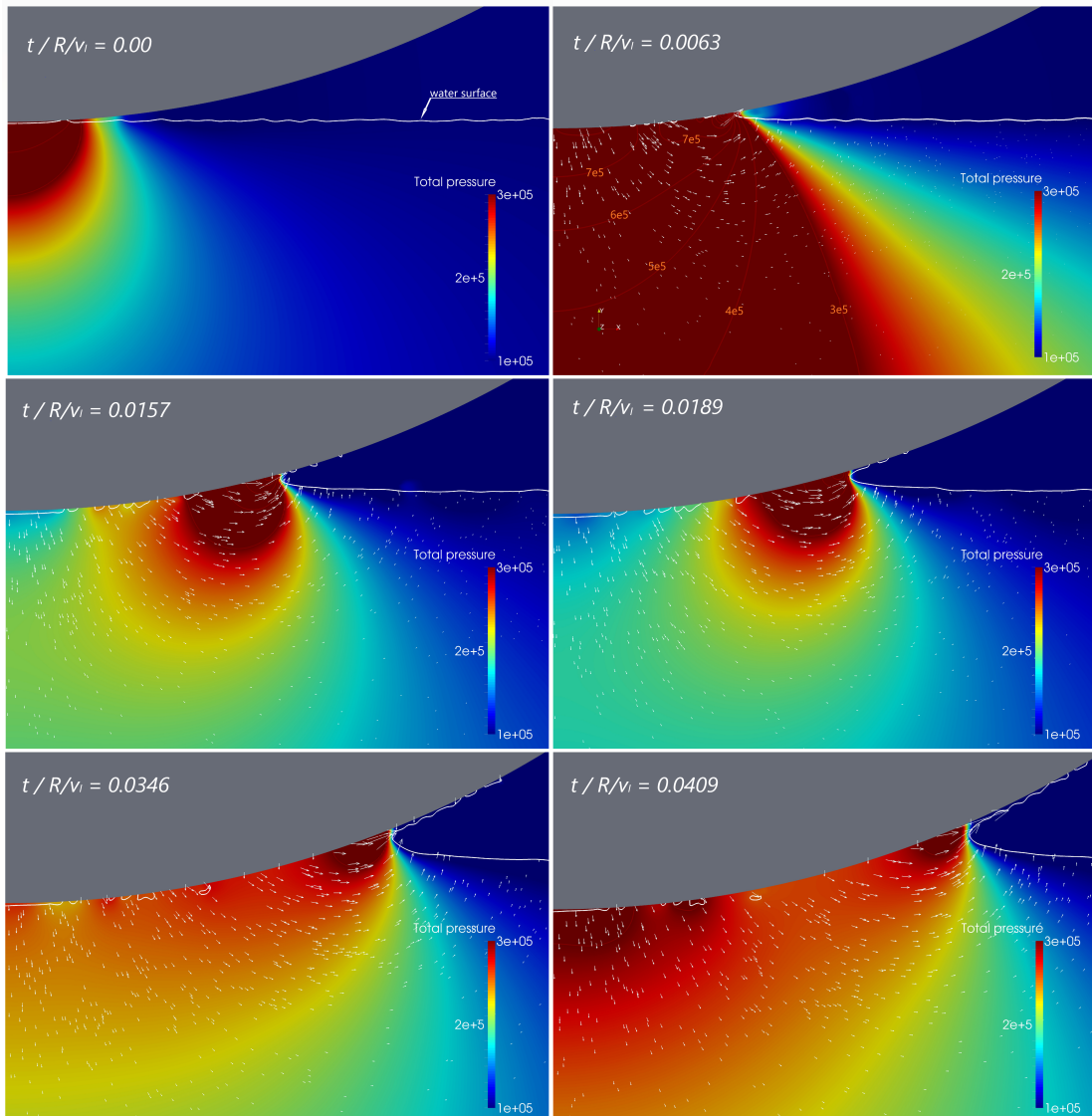
Figure 5.2: Pressure and velocity field and water-air interface in the impact area at different time steps showing important processes of early stage of slamming event, such as peak pressure, formation of water jet beneath the cylinder and contraction/expansion of trapped air beneath the cylinder. Plots are generated by the results of semi-rigid entry model in series S3 with the impact velocity of 5.5 m/s.

The first snapshot in Figure 5.2 (at $t = 0.0R/v_I$) shows the pressure field and water-air interface at the time very close to the first encounter of the cylinder surface with the surface of the water body. As is observable in that snapshot, an entrapped air region is formed beneath the cylinder in a region between 0° and 3° (measured for half section) and compressed by the pressure build-up of the collision. Although the entrapment of air during the impact of cylindrical objects into a water body surface is reported in the literature (such as in Van Nuffel (2014)), there is no quantification available to compare the results of the present numerical simulation with relevant experimental data. However, due to the 2D setup of the numerical models, it can be expected that the volume of entrapped air is higher than that in a 3D setup in real physical conditions.

The second snapshot of Figure 5.2, taken at $t = 0.0063R/v_I$, shows the state of peak impact pressure occurrence. The time interval between the second and first snapshots is $0.2\,ms$. During this very short time, the span of the cylinder-water interface extends from 3° to 10°, and a jet of high-speed water is formed at the tip of that interface. One can also see that the trapped air volume is completely compressed at the peak pressure time. The other four plots show that trapped air volumes oscillate between contraction and expansion, which causes high-frequency oscillation in the hydrodynamic impact force on the cylinder. Oscillatory slamming pressure induced by the contraction-expansion of air bubbles is a physical phenomenon and has been reported by Chan et al. (1995), Lin and Shieh (1997), Hildebrandt (2012), and Van Nuffel (2014). The snapshot at $t = 0.0189R/v_I$ was taken at the time of maximum expansion of the largest trapped air pocket, while the second contraction after the first one is captured in snapshots at $t = 0.0346, 0.0409R/v_I$. Another remarkable phenomenon noticeable in the plots is that the highest pressure value on the cylinder-water interface is always situated at the water jet's root.

The effects of hydroelasticity and aeration on the evolution of pressure distribution can be well observed in Figures 5.3 and 5.4, where the variations of pressure distribution around the cylinder perimeter in time are presented using the simulation results of non-aerated as well as aerated water entry of the semi-rigid cylinder ($f_1 = 3060\,Hz$) and compliant cylinder ($f_1 = 28\,Hz$). The effect of trapped air is also noticeable in all plots, particularly in the plots corresponding to the non-aerated cases. The cushioning effect of the trapped air has flattened out the pressure time histories at the perimeter angle interval of 0° to 5°, where the highest pressure peak is expected to occur according to Wagner (1932) and von Karman (1929) theories as well as experimental results reported by Van Nuffel (2014). After the tip of the water jet passes the perimeter angle of 6°, the impact pressure profile shows a narrower peak profile and higher contrast, and the peak slamming pressure appears at perimeter angles about 9°, which may also be seen in Figure 5.2 at $t = 0.0083\,R/v_I$.

Figures 5.3 and 5.4 also reveal that aeration parameter exhibits a significant curbing effect on the magnitude of peak pressures. To have a better quantitative overview, table 5.4 presents the values of maximum slamming pressure exerted on the semi-rigid cylinder and
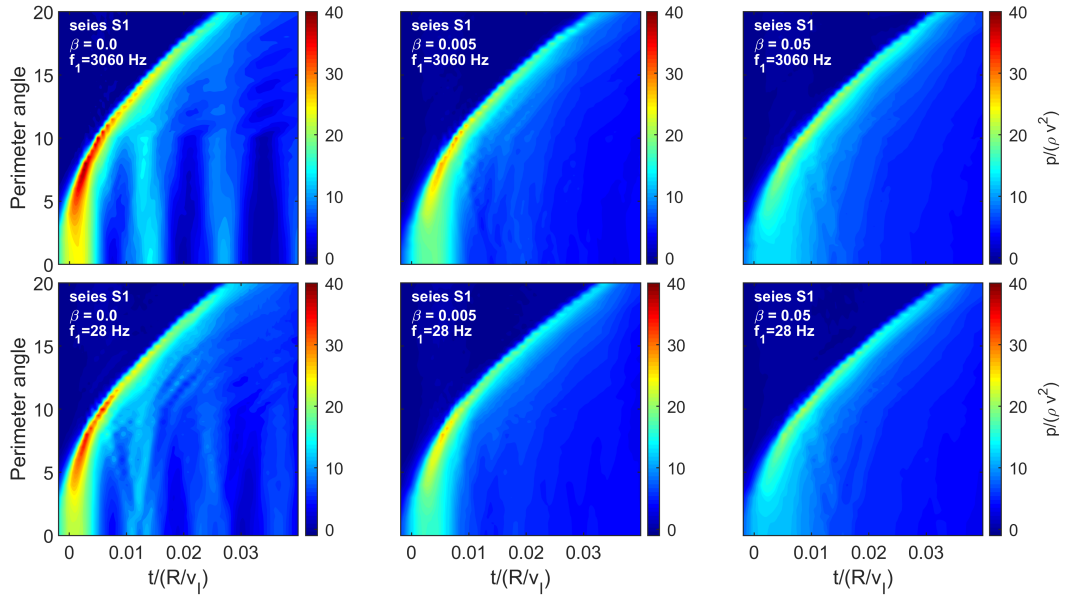
Figure 5.3: Variation of pressure around the perimeter of the cylinder half in time resulted from pure as well as aerated water entry of the semi-rigid cylinder (up) and the most flexible cylinder with dry eigenfrequency of 28 Hz (down) in simulation series S1; The pure water entry cases ($\beta = 0.0$) are shown in the left plots.
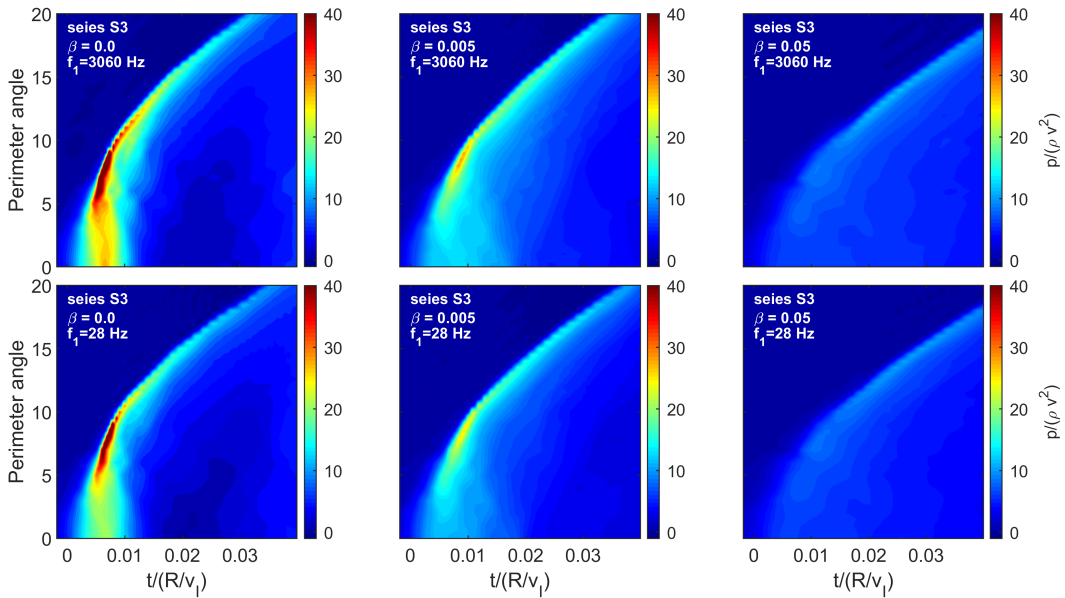
Figure 5.4: Variation of pressure around the perimeter of the cylinder half in time resulted from pure as well as aerated water entry of the semi-rigid cylinder (up) and the most flexible cylinder with dry eigenfrequency of 28 Hz (down) in simulation series S3; The pure water entry cases ($\beta = 0.0$) are shown in the left plots.

the most compliant cylinder for all entry simulations. The percentages of reduction in peak slamming pressures in aerated cases with reference to corresponding non-aerated cases are also shown beside peak pressure values. Entry simulations with 0.5% aerated water show 23.1% to 68.3% reduction of peak impact pressures, such that the highest reduction rate corresponds to the highest impact velocity. The relation between the peak pressure and the impact velocity and aeration level is discussed further later. In all simulation series, Peak impact pressure values of compliant cylinder entry are lower than that of corresponding semi-rigid cylinder entry. This difference is higher for the pure water entries and increases with higher impact velocities. For instance, in the S1 series ($v_I = 1.5\,m/s$), the peak pressure exerted on the semi-rigid specimen is 9.8% higher than that occurred in the water entry of the most compliant cylinder, while in the S4 series ($v_I = 7.5\,m/s$), the peak pressure is 18.7% higher for the rigid cylinder entry case. Similar to what was observed in the flat plate entry cases, here, it might be noticed that the difference between peak impact pressures of cylinders with different flexibility decreases considerably when the water is aerated. This phenomenon is discussed in more detail later.

Table 5.4: Peak impact pressure values occurred on aerated and pure water entries of semi-rigid cylinder and the most compliant cylinder ($f_1 = 28\,Hz$) for all simulation series. The values within parentheses show the percent changes of aerated case value with reference to the corresponding non-aerated case.

Series name	β	Semi-rigid cylinder		Compliant cylinder ($f_1 = 28\,Hz$)	
		$p_{max}(bar)$	$p_{max}/(\rho v_I^2)$	$p_{max}(bar)$	$p_{max}/(\rho v_I^2)$
	0.000	0.9	39.5	0.8	35.4
S1 ($v_I = 1.5$ m/s)	0.005	0.7 (-23%)	30.2	0.6 (-23%)	27.33
	0.050	0.5 (-42%)	23.0	0.5 (-39%)	21.75
	0.000	5.9	46.8	5.0	39.8
S2 ($v_I = 3.5$ m/s)	0.005	3.9 (-33%)	31.0	3.5 (-30%)	27.90
	0.050	1.9 (-68%)	14.8	1.8 (-65%)	14.00
	0.000	19.6	63.2	16.1	51.7
S3 ($v_I = 5.5$ m/s)	0.005	8.8 (-55%)	28.5	8.0 (-50%)	25.90
	0.050	3.6 (-81%)	11.7	3.3 (-79%)	10.74
	0.000	49.9	86.3	40.5	70.1
S4 ($v_I = 7.5$ m/s)	0.005	15.8 (-68%)	27.3	13.5 (-67%)	23.45
	0.050	5.0 (-90%)	8.6	4.8 (-88%)	8.23

Figure 5.5 presents the evolution of pressure distribution in more detail, where the profiles of pressure around the cylinder at perimeter angles of 0° to 20° are drawn for pure and aerated ($\beta = 0.5\%$) water entry of the semi-rigid cylinder as well as the most compliant cylinder ($f_1 = 28Hz$) at eight time steps. The dashed line in each plot shows the pressure

profile at the moment of theoretical touchdown, which is when the lowest point of the cylinder travels the initial distance to the water surface (d_I). The six dotted lines present the pressure profiles at constant time increments of $0.001R/v_I$, and the solid line shows the profile of pressure at the time of peak pressure. Qualitatively similar to what has been reported by Hicks and Purvis (2013), the trapped air shifts the peak pressure point from $0°$ to a perimeter angle between $5°$ to $10°$. The pressure profiles at $t/T_i = 0$ are displaying the pressure of trapped air and showing much higher values in series S1 cases. Similar to the simulations with flat plates, the reason lies in the deformation of the water surface. Since the water surface's deformation is larger in higher impact velocities, the pressure build-up starts later than the theoretical touch-down time. The exact time of peak pressures for each case is also displayed in the plots, which reveals that, in general, both aeration and flexibility cause a delay in a peak pressure moment. Increased compressibility and lower sound speed seem to dampen both the intensity and progress of the impact pressure wave around the cylinder in aerated cases.

5.2.2 Effect of aeration and hydroelasticity on the peak impact pressure

Figure 5.6 presents an inclusive view of the relation between the peak impact pressure and the aeration level. The non-dimensional value of peak pressure in pure water entry cases greatly increases from series S1 to S4, which shows that, in relation to velocity, the peak pressure varies with higher than quadratic order. This will be discussed in more detail later. The plots show that a great deal of drop in peak pressure occurs with the lowest aeration level of 0.5%, and the declining trend resembles an exponential function. This type of trend has been seen in the experimental results presented by Ma et al. (2016), which implies that the present numerical model has effectively captured the principal processes through which the air content affects the evolution of pressure in the impact incident.
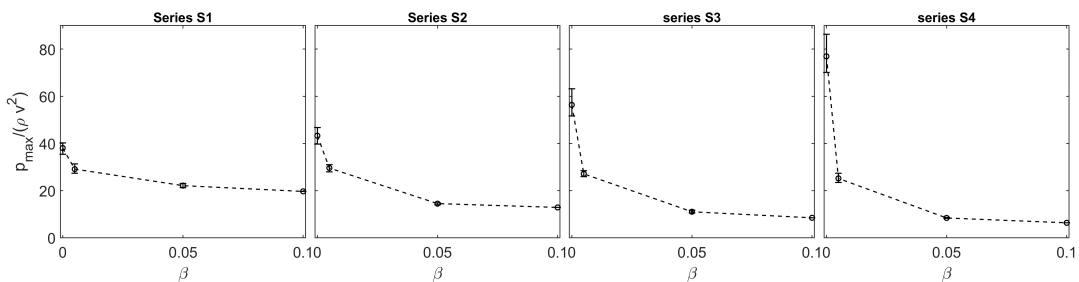
Figure 5.6: Variation of peak impact pressures in all cases with respect to aeration level. The circles show the mean values and the error bars display the variation of peak pressure due to cylinder's flexibility.

Another interesting point is that the higher the impact velocity, the deeper the peak pressure drops in response to 0.5% aeration. The error bars in the graphs of Figure 5.7 show the variability of peak pressure with respect to variation in the cylinder's flexibility. It
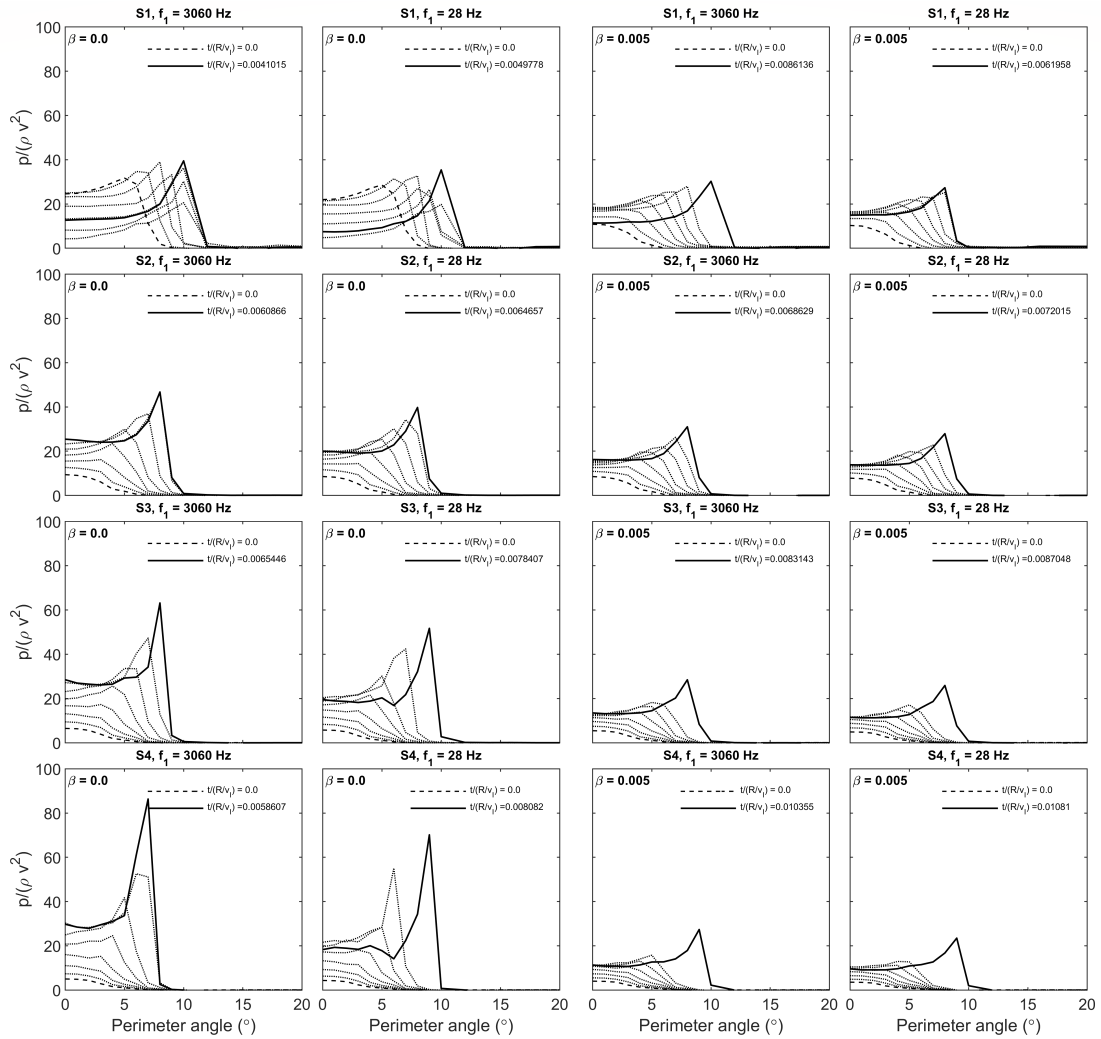
Figure 5.5: Profiles of pressure around the cylinder at $t/T_i = 0.0$ (dashed line), $t/T_i = 0.001 - 0.006$ (dotted lines with intervals of 0.001), and at the moment of peak pressure (solid line) resulted from pure and aerated ($\beta = 5\%$) water entry of semi-rigid and compliant ($f_1 = 28Hz$) cylinders.

is noteworthy that the variability of peak pressure expands with increasing impact velocity, and similar to what was seen in simulations with flat plates in the last chapter, aeration seems to cause this variability to diminish significantly.

The relation between cylinder's flexibility and peak pressure can be observed in Figure 5.7, where, in order to be able to compare the results of all simulation series with each other, the ratio of each case's peak pressure to its corresponding value from semi-rigid cylinder entry is drawn against cylinder's eigenfrequency. The points at the far right of the plots with ratios of 1.0 represent the semi-rigid cases. Except in series S1, the highest peak

pressure values belong to the semi-rigid cases, and it seems that the peak pressure value in all three graphs increases quasi-linearly with respect to the growth of eigenfrequency in logarithmic scale. The variation range of peak pressure is reduced considerably from up to 20% in pure water entry cases to less than 10% in aerated cases with a 5% air fraction. The rate of reduction in sensitivity of peak pressure values to flexibility is less than what was seen in simulations with flat plates. However, similar to chapter 4, it may be concluded that aeration reduces the sensitivity of peak impact pressure on cylinder shells' flexibility in slamming events.

Aeration level and compressibility of water are two parameters identified in chapter 4 to have an essential role in the relation between peak pressure and impact velocity. Figure 5.8 (left) presents the values of peak pressure for all simulations as functions of impact velocity with the same purpose. The quadratic fitting curve drawn for the data points of pure water entry simulations seems to be poorly fitted with the data, while the power-law approximation displays an excellent correlation with the data in all cases. Like the plate entry cases of the previous chapter, the approximation functions displayed by dotted curves in the plot may be written as

$$p_{max} = k_p \rho v_I^{0.36 \ln c}, \tag{5.1}$$

where ρ is the density of pure/aerated water, c is the speed of sound in the pure/aerated water, and k_p is a coefficient calculated as

$$k_p = (15.75 - 105.46\beta)\beta^{(-0.001 \ln(\beta+\epsilon))} + 22, \tag{5.2}$$

in which β is the air fraction value or aeration level and ϵ is a very small number of the order of 10^{-50}. The above formulation is implemented only to show the trends in the problem, and more extensive experimental and numerical investigations are needed to
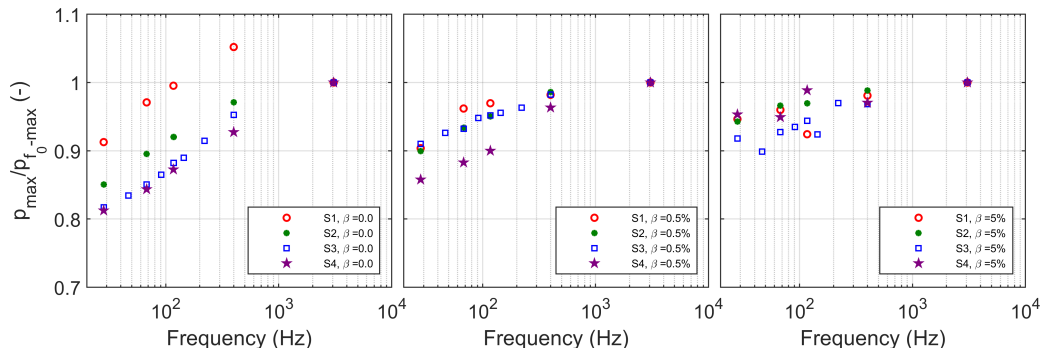
Figure 5.7: Ratio of peak pressure values of all cases to the corresponding semi-rigid case of their own series as a function of 1 st eigenfrequency, for cases with non-aerated water, $\beta = 0.0$ (left), aerated water, $\beta = 0.5\%$ (middle), and $\beta = 5\%$ (right).

find a valid general rule. However, it is useful to compare the calculation of Equation (5.1) with available experimental data. In Figure 5.8 (right), mean values of peak impact pressure measured at two points at perimeter angles 0° and 5° around the cylinders in water entry experiments carried out by Van Nuffel (2014) are drawn against the cylinder impact velocity along with the dotted curve drawn using Equation (5.1). The calculated peak pressure values are, on average, 37% lower than their corresponding measured peak pressures at 0°, and the difference between the two data-sets remains in the same order. As argued earlier, the trapped air volume is larger than what has been reported in real laboratory conditions. Therefore, the enhanced effect of trapped air cushioning can be considered the leading cause of this underestimation. However, on average, the calculated peak pressures are 26% higher than their experimental counterparts at a 5° perimeter angle. As shown in Figure 5.5, the peak pressure occurs at a perimeter point between 5° to 10°, which means that the numerical model seems to overestimate the peak impact pressure at this range.
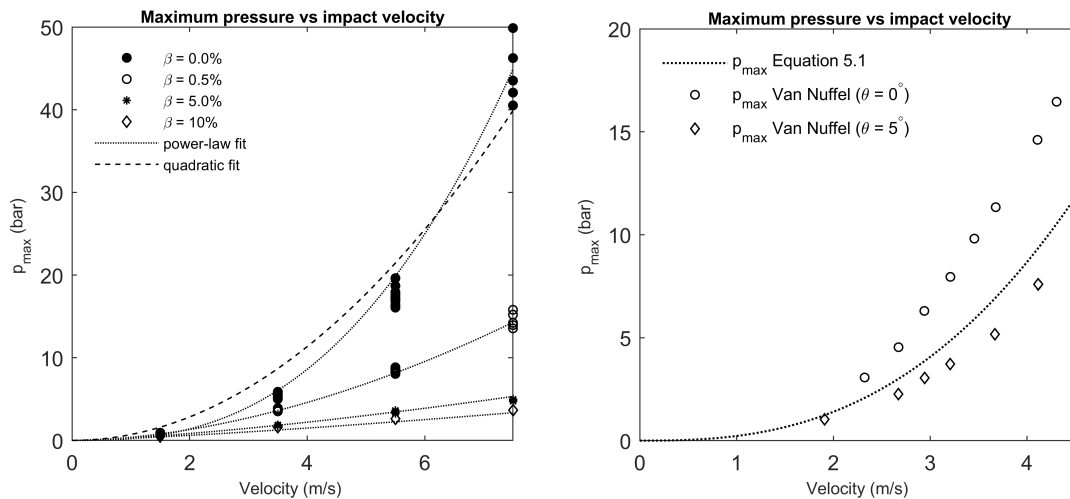
Figure 5.8: Left: Peak slamming pressure values as functions of impact velocity resulted from all simulations with pure water as well as aerated water. The quadratic and power-law approximation curves are added to the graphs to show better the trends. Right: peak impact pressure as function of velocity resulting from Equation (5.2) in comparison with the experimental data presented in (Van Nuffel, 2014). The experimental data points show the mean values of measured at perimeter angles 0° and 5° (right).

5.3 Analysis of impact inline force

5.3.1 Characteristics of impact force during non-aerated water entry

Figure 5.9 (left) presents an example of the slamming force time history obtained from the semi-rigid cylinder entry into pure water with 5.5 m/s entry velocity (series S3). It

can be observed that the impact force rises very quickly to a sharp peak, which lasts for about 0.9 ms. After the first peak, the force signal does not drop to zero and oscillates around a decaying average. The force's amplitude of oscillation is near 10% of the peak force value. The oscillation of the force signal can be interpreted as the effect of repetitive cycles of compression and expansion of the trapped air beneath the cylinder, as shown in Figure 5.2. To examine this suggestion, the power spectra of both pressure and force time series are plotted together in Figure 5.10. The pressure spectrum is the average spectral density of recorded pressure at probes located between 0° to 10° perimeter angles. Both spectra have peaks near $500 \, Hz$, which is the major oscillation frequency in the force signal. As mentioned earlier, this kind of oscillation has been observed in water entry experiments on cylinders. The difference between the present simulation results and similar experiments is that higher intensity and significantly lower decay rate can be seen in the present force signals' oscillations. Part of this difference can be caused by the 2D setup of the present model and the fact that the trapped air volume is considerably larger than in real conditions. Moreover, applying a linear equation of state instead of solving an energy conservation equation may also significantly affect the higher than real life-span and intensity of the pressure oscillations.

Figure 5.9 (right) exhibits a comparison of above mentioned simulated force time history with (i) the most recent available experimental data of Van Nuffel (2014), (ii) the time series calculated by the theoretical formulation of Wienke and Oumeraci (2005), and (iii) the empirical formula proposed by Miao (1988). The forces are presented in the form of
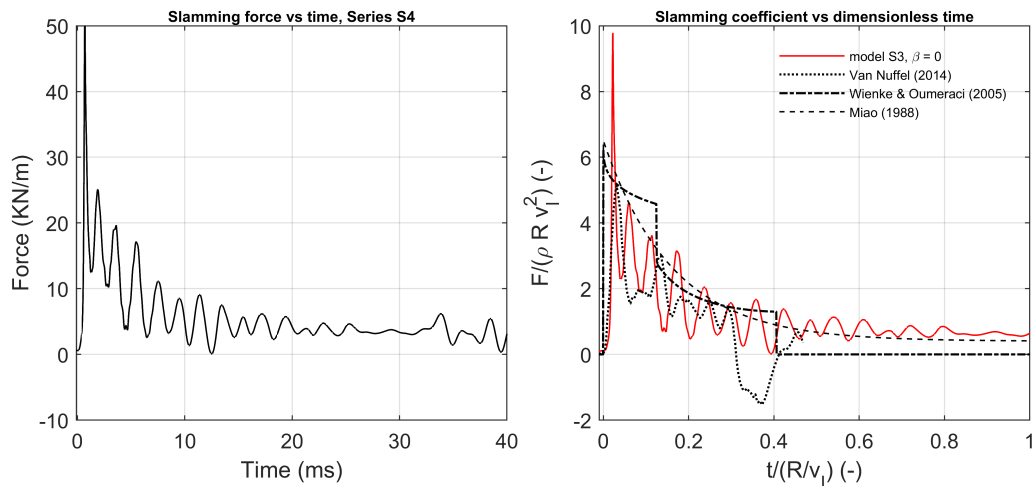
Figure 5.9: Left: time history of impact force recorded in the pure water entry of the semi-rigid cylinder in series S3 simulations. Right: time history of dimensionless force derived from the same data as in the left graph in comparison with the experimental data presented by Van Nuffel (2014), theoretical model of Wienke and Oumeraci (2005), and empirical formulation of Miao (1988).

the dimensionless slamming coefficient ($C_s = F/(\rho R v_I^2)$) as functions of time in the form of the dimensionless submergence. The peak slamming coefficient is 9.7 in the present numerical model, which is considerably higher than the corresponding values obtained by Van Nuffel experiments (nearly 5.2), Wienke & Oumeraci theory (about 6.28), and Miao formula (6.5). Arguably, it is not clear if the peak slamming coefficient of the present model is nonphysical. This is based on the fact that the Wagner method, which is the base for Wienke's formula, does not consider the compressibility of water, and on the other hand, all the experimental demonstrations of the slamming force are based on the response of the force transducers and not the real slamming force. Apart from the peak impact force, the force time-history's overall trend in the present numerical model seems to be reasonably consistent with the reference experimental and theoretical results.

5.3.2 The role of aeration and hydroelasticity

Figure 5.11 compares impact force time histories in the semi-rigid cylinder water entry cases with different aeration levels. Similar to the previous figure, the datasets are obtained from the series S3 simulations. The first noticeable distinction between the non-aerated and aerated cases is that the oscillation disappears in the aerated cases. This can be explained by the fact that the compressibility of water greatly increases in aerated cases, which consequently reduces the compression of trapped air. Peak force values show a reduction rate similar to peak pressure values.

Another interesting characteristic in Figure 5.11 is the variation of rising time due to aeration. It seems that the rising time in the non-aerated and the low-aerated (0.5% aeration) cases are in similar orders, while the cases with higher aeration levels (5% and 10%) have much higher rising times. To have a better view, values of peak impact force, in terms of slamming coefficient (C_s), and the rising time of the impact forces on the semi-rigid cylinder as well as the most compliant cylinder for all simulation series are presented in Table 5.5.

As table 5.5 shows, both semi-rigid and compliant cylinder entries have near-identical rising times in all simulation series. On the other hand, the pure water entry slamming coefficients in compliant cylinder entries are 10.5% to 21% less than their corresponding values in semi-rigid cylinder entries. Furthermore, the difference in slamming coefficients reduces but does not vanish in aerated cases, contrasting to what was seen in the plate entry simulations (Please note that for $\beta = 10\%$, the simulations were carried out only for the semi-rigid cylinder). The slamming coefficient rate of reduction due to aeration is also less intense than that observed in the plate entry cases, though still significant (up to 51% reduction in 0.5% aerated water entries). Variation of peak slamming force in the form of slamming coefficient as a function of aeration level is drawn for all simulations in Figure 5.12. The trends are similar to that in peak pressure values depicted in Figure 5.6, with a noticeable distinction, i.e., mean C_s values in pure water entries seems to be almost
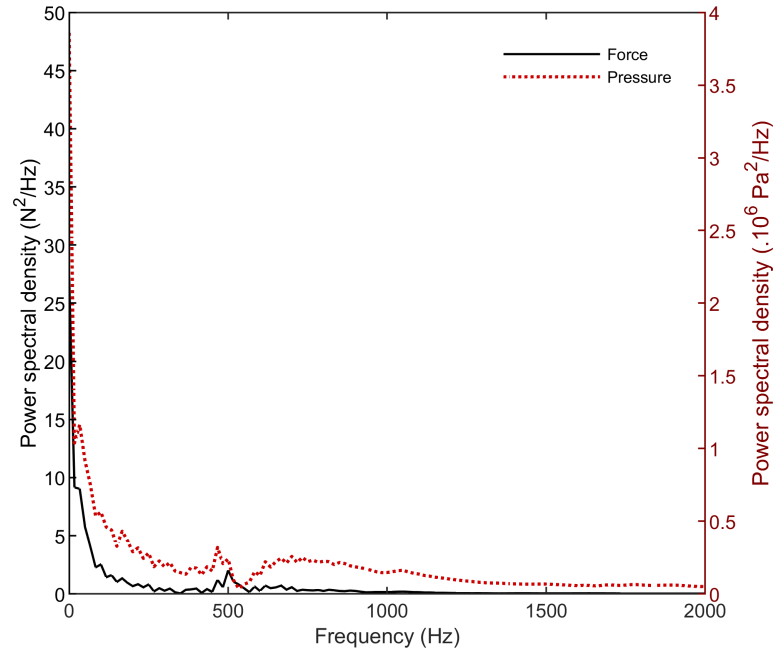
Figure 5.10: Average spectral density of pressure time histories recorded at perimeter range of 0° to 10° in comparison with the spectral density of the force time history from the pure water entry simulation of the semi-rigid cylinder with entry velocity of 5.5 m/s (simulation series S3).
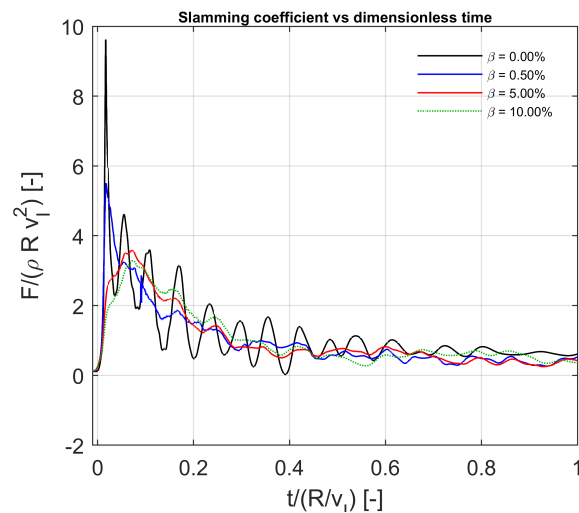
Figure 5.11: Time history of non-aerated and aerated water entry of semi-rigid cylinder with the entry velocity of 5.5 m/s (simulation series S3).

Table 5.5: Slamming coefficient values and rising time in aerated and pure water entries of semi-rigid cylinder and the most compliant cylinder ($f_1 = 28\,Hz$) for all simulation series. The values within parentheses show the percent changes of aerated case value with reference to the corresponding non-aerated case.

Series name	$\beta(\%)$	Semi-rigid cylinder		Compliant cylinder ($f_1 = 28\,Hz$)	
		C_s (-)	Rising time (ms)	C_s (-)	Rising time (ms)
S1 ($v_I = 1.5$ m/s)	0.000	8.5	0.7	7.6	0.7
	0.50	7.4 (-13%)	0.8 (+14%)	6.6 (-13%)	0.8 (+14%)
	5.0	5.9 (-31%)	1.0 (+42%)	5.5 (-28%)	1.0 (+42%)
	10.0	5.9 (-31%)	1.0 (+42%)	NA	NA
S2 ($v_I = 3.5$ m/s)	0.000	9.0	0.7	7.4	0.7
	0.50	6.3 (-30%)	0.7 (0%)	5.4 (-27%)	0.7 (0%)
	5.0	4.0 (-56%)	1.0 (+43%)	3.4 (-54%)	1.0 (+43%)
	10.0	4.0 (-56%)	1.0 (+43%)	NA	NA
S3 ($v_I = 5.5$ m/s)	0.000	9.8	0.4	7.9	0.4
	0.50	5.5 (-55%)	0.5 (+25%)	4.8 (-39%)	0.50 (+25%)
	5.0	3.6 (-63%)	1.2 (+200%)	2.9 (-63%)	1.2 (+200%)
	10.0	3.6 (-63%)	1.2 (+200%)	NA	NA
S4 ($v_I = 7.5$ m/s)	0.000	9.5	0.3	7.5	0.3
	0.50	4.7 (-51%)	0.4 (+33%)	4.0 (-46%)	0.4 (+33%)
	5.0	3.3 (-65%)	1.3 (+333%)	2.7 (-64%)	1.3 (+333%)
	10.0	3.3 (-65%)	1.3 (+333%)	NA	NA

constant with increasing impact velocity. This implies that, in contrast with maximum pressure values, peak slamming forces show a quadratic increase with impact velocity.

Variation of peak slamming force as a function of velocity and aeration is shown in Figure 5.13. Similar to plate entry cases, a single function can be derived to predict the peak slamming force for a given impact velocity and aeration level as

$$F_{max} = k_f\,\rho\,R\,v_I^{(0.18\ln c + 0.68)}, \tag{5.3}$$

in which, R is the radius of the cylinder and the coefficient k_f is calculated by the following function.

$$k_p = (0.98\beta + 0.87)\beta^{(-0.001\ln(\beta+\epsilon))} + 4.17, \tag{5.4}$$

Similar to Equation (5.2), ϵ is a very small quantity. The approximation function drawn
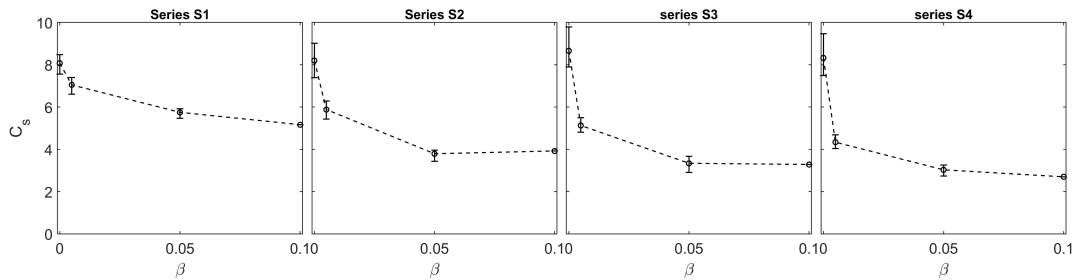
Figure 5.12: Variation of slamming coefficient in all cases with respect to aeration level. The circles show the mean values and the error bars display the variation of peak pressure due to cylinder's flexibility. There is no error bar for cases with $\beta = 10\%$ because the simulations were conducted only with the semi-rigid cylinder.

for four aeration levels of present simulation cases with dotted curves in Figure 5.13 gives a good agreement with the simulation data. As shown in the figure, the quadratic approximation drawn for pure water data gives identical values to Equation (5.3). This is remarkable due to the fact that all the force calculation formulas in the literature which are based on experimental data (e.g., Campbell and Weynberg (1980), Miao (1988), and Wienke and Oumeraci (2005)) have quadratic forms in terms of impact velocity, which can be a validation evidence for the present formula.

The effect of cylinder flexibility on the maximum impact force can be observed in Figure 5.14, where the maximum impact force normalized with the corresponding semi-rigid case is drawn as a function of the cylinder eigenfrequency for the pure and aerated water entries.
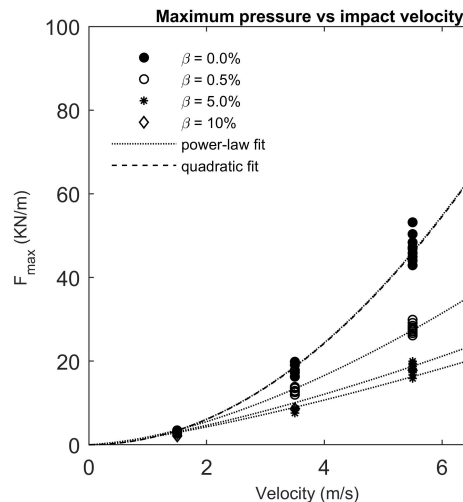
Figure 5.13: Peak slamming force values as functions of impact velocity resulted from all simulations with pure water as well as aerated water. The quadratic and power-law approximation curves are added to the graphs to show better the trends.

From the figure, it seems that the maximum force shows a logarithmic increase trend as a function of eigenfrequency. The lowest impact force belongs to the most compliant cylinder in all series, with up to 22% lower value in reference to the corresponding semi-rigid case, which except one case has the highest impact force value in all simulation series. As noticed before, Figure 5.14 shows that the variability of impact force as a function of cylinder flexibility does not decrease remarkably in aerated cases. This is a noticeable contrast to the plate entry cases.

5.3.3 Impact force impulse

The impact force impulse values were shown to be less affected by aeration than peak force/pressure in plate entry simulations. The impact force impulse of cylinder entries is calculated by integrating the force from the time of touch-down $(t/(R/v_I) = 0)$ to the time $t/(R/v_I) = 0.5$, in which we may assume that the force reaches a quasi-static state.

In cylinder entry simulations, as shown in Figure 5.15 and Table 5.6, the rate of reduction in force impulse is almost at the same order as in the slamming coefficient for the low-velocity entry of series S1. In contrast, with higher impact velocities, the difference between the force impulse values of aerated and non-aerated water entries vanishes. Another noticeable point is that no meaningful decline or increase can be seen in the force impulse values of aerated cases due to aeration level increase.

The dependence of force impulse on the cylinder's flexibility is observable in Figure 5.16, where the values of force impulse are drawn against the eigenfrequency of cylinders for all simulations. It seems from the figure that the force impulse values are in general slightly higher in the compliant cylinders comparing to the semi-rigid cylinder entries. The maximum difference between force impulse values in different cylinders with the same impact velocity is near 10% of the mean value. This may have a practical implication
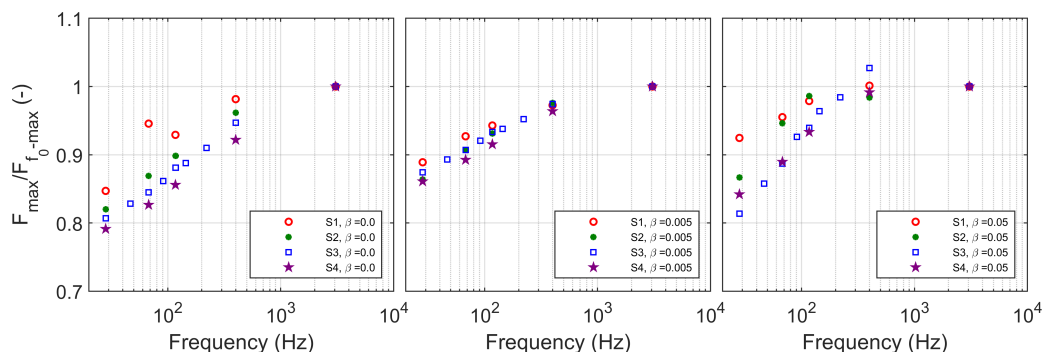
Figure 5.14: Ratio of peak impact force values of all cases to the corresponding semi-rigid case of their own series as a function of 1 st eigenfrequency, for cases with non-aerated water, $\beta = 0.0$ (left), aerated water, $\beta = 0.5\%$ (middle), and $\beta = 5\%$ (right).
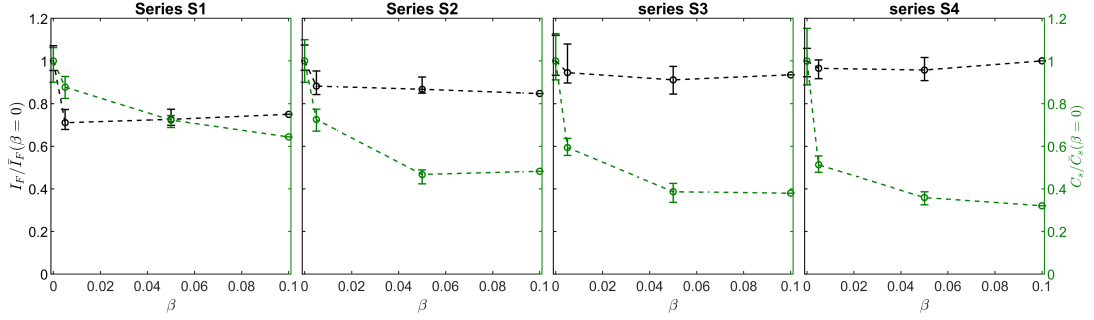
Figure 5.15: Relative mean impact force impulse I_F and impact force coefficient C_s as functions of aeration level for series S1 – S4. The values for 10% aeration level are only available for the semi-rigid cylinder.

Table 5.6: Mean impact force impulse values for simulation series S1-4. The values within parentheses show the percent changes of aerated case value with reference to the corresponding non-aerated case. The values for 10% aeration level are only available for the semi-rigid cylinder.

Series name	F_I (Ns/m), $\beta = 0.0$	F_I (Ns/m), $\beta = 0.5\%$	F_I (Ns/m), $\beta = 5.0\%$	F_I (Ns/m), $\beta = 10.0\%$
S1 $(v_I = 1.5 m/s)$	38.4	27.6 (-28%)	28 (-27%)	28 (-27%)
S2 $(v_I = 3.5 m/s)$	102.8	90.8 (-12%)	89.6 (-13%)	88 (-14%)
S3 $(v_I = 5.5 m/s)$	143.3	135.6 (-5%)	130.2 (-9%)	134 (-6%)
S1 $(v_I = 7.5 m/s)$	187.2	180.4 (-4%)	179.6 (-4%)	187.4 (+0%)

suggesting no need for a coupled FSI simulation to determine impulse, which is an essential parameter for calculating structural responses (Ghadirian and Bredmose, 2019).

Variation of force impulse with impact velocity for different aeration levels is observable in Figure 5.17. The pattern of variation is different from what was seen in peak force and pressure values. Here the trend approximation curve is power functions with the same
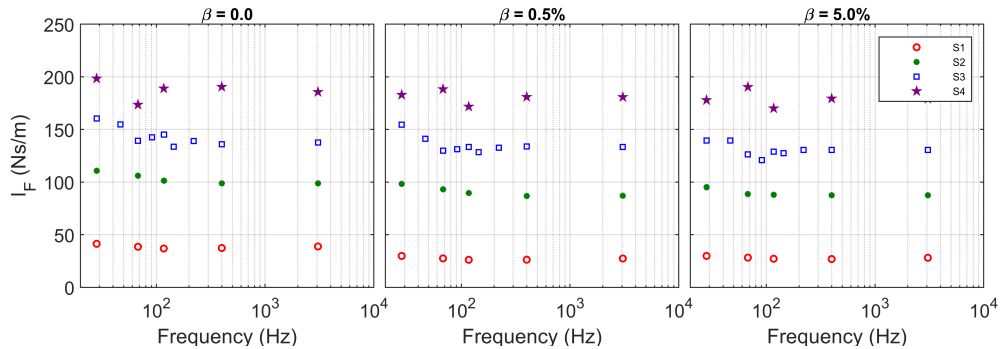
Figure 5.16: Force impulse vs 1st eigenfrequency, for cases with non-aerated water, $\beta = 0.0$ (left), aerated water, $\beta = 0.5\%$ (middle), and $\beta = 5.0\%$ (right).

exponent value of 0.85.

5.3.4 Analysis of response characteristics

Investigating the structural response to water entry impact has been carried out by observing the recorded bending strain in the cylinders' lowest point. Two main observations are discussed: (i) characteristics of strain time series and (ii) the maximum values of response strain.

Strain time series

Figure 5.18 presents a complete view of the response strain variation with time in simulations of series S3, in which a larger number of cylinders with different eigenfrequencies were simulated. To better see the differences in patterns of different graphs, the strain values of every cylinder are normalized with the maximum strain recorded in the corresponding non-aerated water entry. The following observations can be indicated from the plots.

- The highest absolute strain occurs in the first half-period of response in all cases, which contrasts with the results of plate entries, where the interaction of trapped air with the plate caused a delay in the occurrence of maximum strain.

- The contribution of higher natural frequencies is considerably higher in the non-aerated water entries. These high-frequency vibrations dissipate much faster than that of the main eigenfrequency. Figure 5.19 presents, as an example, the relative amplitude spectrum of strain signal in 4 cylinder model entries. It can be observed from the figure that with higher aeration levels, the strain amplitude of higher eigenfrequencies
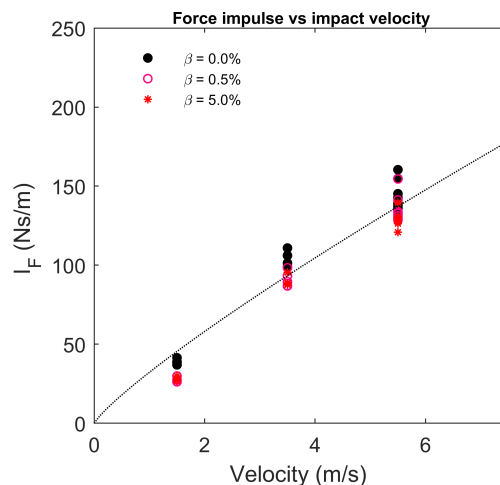
Figure 5.17: Force impulse as functions of impact velocity resulted from all simulations with pure water as well as aerated water ($\beta = 0.5\%$, 5.0%).

reduces substantially. This observation may have interesting implications from the fatigue design point of view, as it has been shown that the high-frequency bending strain has a significant role in fatigue damage (see chapter 2).

- Similar to plate entries, aeration seems to have an additional damping effect on slamming vibrations of cylinders. The plots also reveal that this damping shows to be stronger with higher levels of aeration. This is also a point of interest, particularly for fatigue life assessment suggesting further studies.

- Ratios of maximum strain values in aerated-water entries to that of non-aerated water entries seem to be considerably higher than what may be expected from the corresponding ratios of slamming coefficients. Table 5.7 presents a detailed overview of maximum absolute strain values resulted from non-aerated and aerated (with $\beta = 0.5\%$, 5.0%) water entry simulations with flexible cylinders. Comparing the values in Table 5.7 to the values of slamming coefficients shown in Table 5.5 also confirms that the slamming coefficient reduction does not necessarily lead to a reduction in peak strain with the same order. As an example, the slamming coefficient of the cylinder with 46 Hz eigenfrequency reduced by 69 % when the entry was simulated with 5 % aeration in water, while the maximum strain in that case reduced by 16 %.

Maximum response strain

The role of flexibility in the ratio of maximum responses in aerated water entries to that of pure water entries can be observed in both table 5.7 and Figure 5.20, where the variation of this ratio is drawn against cylinder's first eigenfrequency for 0.5% and 5.0% aerated water entries. Two different trends can be observed in the two plots of Figure 5.20. In the left plot drawn with the results of 0.5% aerated water entries, the maximum response ratio tends to increase with increasing eigenfrequency of the cylinder shell; In the right plot, the maximum response ratio increase with increasing eigenfrequency up to a maximum point (approximately 0.8), which is different for different series, and with the further increase of eigenfrequency the response ratio declines.

The fact that we see maximum responses in aerated water entries very close to the corresponding maximum responses in pure water entries may lead to the following implications:

- The slamming coefficient, which is derived from the maximum impact force, may not be the major parameter for determining the maximum response, and other parameters such as rising time and force impulse should be taken into consideration in loading and response analysis of the structure.

- As seen in some simulation results, the aerated water entry may cause higher than expected structural responses. As a result, it may be expected that aeration may have
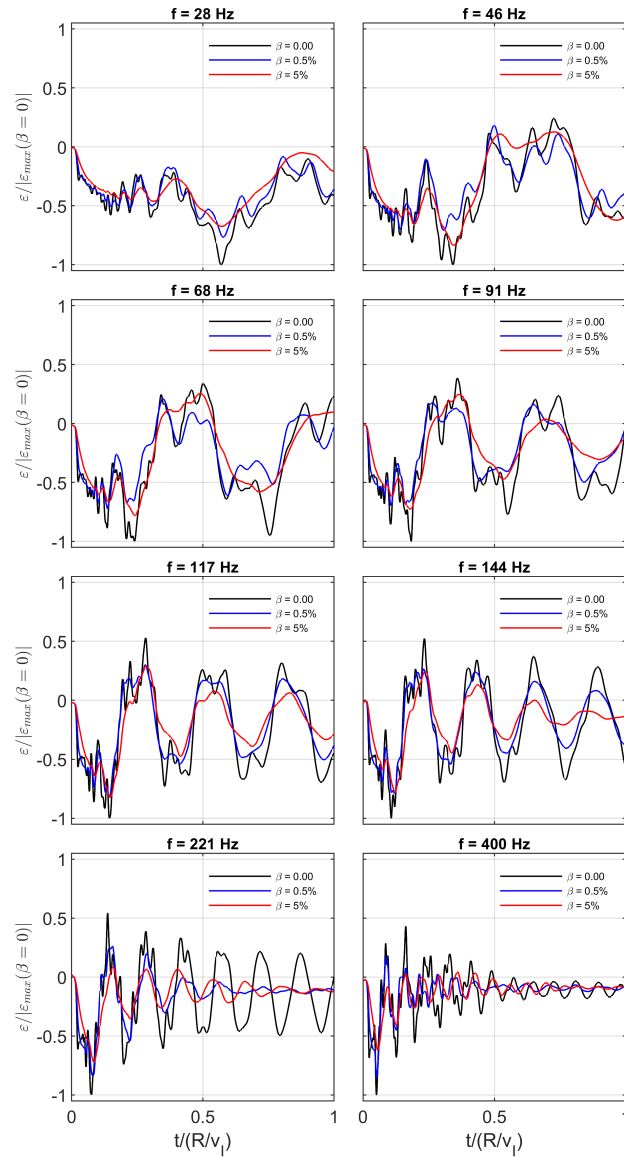
Figure 5.18: Time history of strain during water entry for all simulations of series S3 with impact velocity of 5.5 m/s.
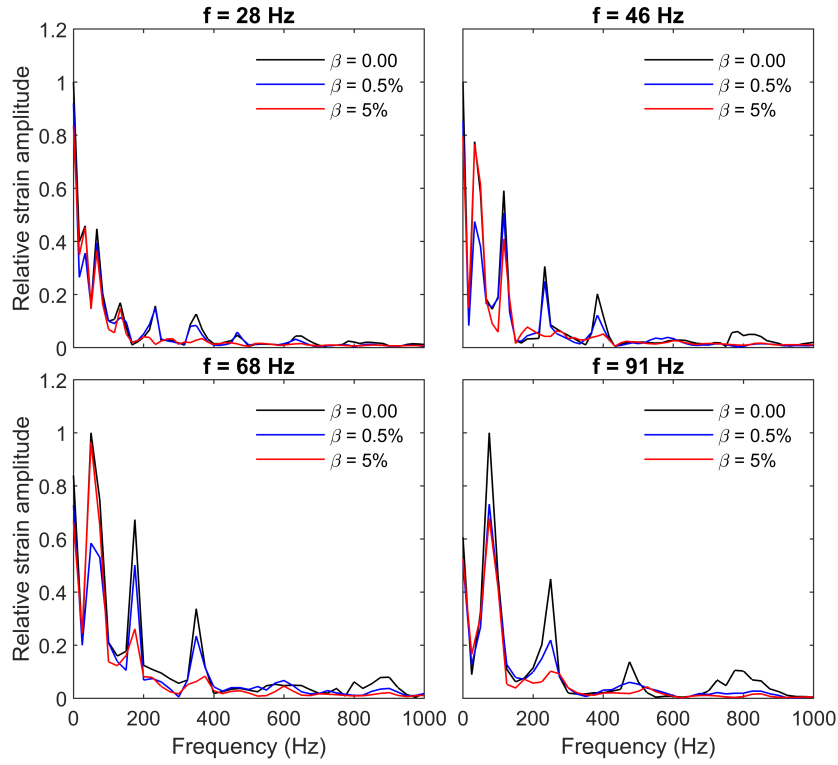
Figure 5.19: Amplitude spectrum of strain in aerated and pure water entry simulations of 4 different cylinders in series S3. The amplitudes are normalized with the maximum amplitude of corresponding non-aerated case.
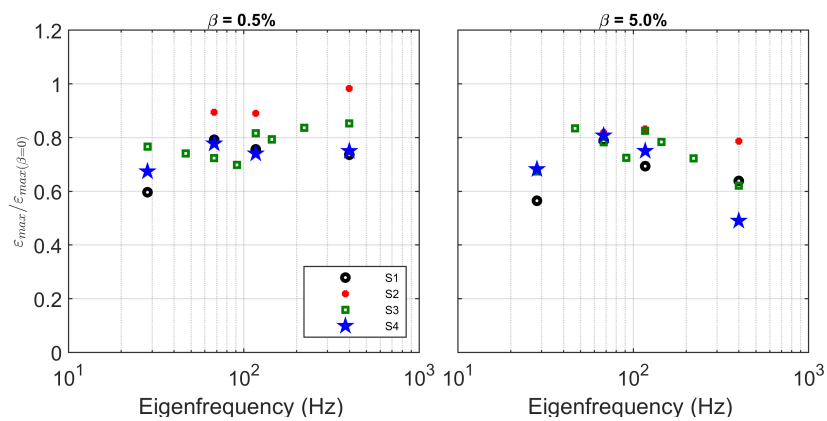
Figure 5.20: variation of the ratio of maximum strain in aerated water entry cases to that of the corresponding pure water entry cases for $\beta = 0.5\%$ (left) and $\beta = 5\%$ (right).

Table 5.7: Maximum strain values in aerated and pure water entries of semi-rigid cylinder and the most compliant cylinder ($f_1 = 28\,Hz$) for all simulation series. The values within parentheses show the percent changes of aerated case value with reference to the corresponding non-aerated case.

Series name	Eigenfrequency f_1 (Hz)	Maximum strain ($\mu m/m$) $\beta = 0.0$	$\beta = 0.5\%$	$\beta = 5.0\%$
S1 ($v_I = 1.5$ m/s)	28	461	275 (-40%)	261 (-43%)
	68	173	137 (-21%)	136 (-21%)
	117	104	78 (-25%)	72 (-31%)
	400	19	14 (-26%)	12 (-37%)
S2 ($v_I = 3.5$ m/s)	28	1387	936 (-32%)	950 (-31%)
	68	564	504 (-11%)	462 (-18%)
	117	353	314 (-11%)	294 (-17%)
	400	80	79 (-1%)	63 (-21%)
S3 ($v_I = 5.5$ m/s)	28	2771	2123 (-23%)	1869 (-33%)
	46	1470	1089 (-26%)	1227 (-16%)
	68	1090	789 (-28%)	853 (-22%)
	91	905	632 (-30%)	656 (-27%)
	117	687	560 (-18%)	566 (-18%)
	144	598	475 (-21%)	469 (-21%)
	221	402	337 (-16%)	291 (-28%)
	400	212	181 (-15%)	131 (-38%)
S1 ($v_I = 1.5$ m/s)	28	4437	2991 (-33%)	3027 (-32%)
	68	1740	1353 (-22%)	1405 (-19%)
	117	1150	851 (-26%)	862 (-25%)
	400	379	284 (-25%)	186 (-51%)

resonating effect in the local response of the cylindrical shells in certain combinations of aeration level, impact velocity, and flexibility.

5.4 Conclusions

This chapter investigates the combined effects of aeration and local hydroelasticity on the characteristics of impact loading and local responses of cylindrical shell sections during water entry slamming events.

Study of impact pressure evolution showed that the maximum impact pressure greatly reduces when the water is aerated. The peak pressure was also shown to have a logarithmic

relation with the cylinder's flexibility in terms of the first eigenfrequency, but this variability declines in aerated entries.

Compressibility of water was shown to play an important role in determining maximum impact pressure, and a simple function was derived that calculates the peak slamming pressure for different impact velocities and aeration levels.

Similar to pressure study, a thorough study was carried out on the characteristics of impact force, which revealed that aeration causes a sharp decline in the peak slamming force, while the rising time of the impact force increases up to 3 times of that in pure water entries due to addition of aeration into the water. Flexibility of the cylinder was observed to have no effect on the duration of rising time for all simulations.

Furthermore, the maximum force was found to be declining logarithmically with cylinder's flexibility increasing. The maximum difference, approximately 20%, was seen between the most compliant cylinder's peak forces and the semi-rigid cylinder. However, the insensitivity of maximum impact force to flexibility in the presence of aeration, observed in the plate entry simulations, was not found in cylinder entries. A new functional relation in the form of a simple power-law was also found, which defines the dependence of maximum impact force on impact velocity and water compressibility.

Effects of aeration and cylinder's flexibility on the impact force impulse were also studied, which learned that force impulse is far less sensitive to aeration than peak pressure and slamming coefficient. The same finding was observed in the variation of force impulse as a function of cylinder's flexibility, where the variation of force impulse with reference to its mean value is less than 10%.

Cylinder's response to water entry slamming was studied using the strain measurement at the cylinder's lowest point. This study revealed that the contribution of higher eigen-frequencies in the response is reduced substantially in the presence of more than 0.5 % aeration. Aeration is also shown to have a damping effect on the response strain, which becomes stronger with increasing aeration level. Finally, in some cases, the maximum response strain values of aerated water entries were observed to be very close to that of pure water entries, implying that, despite the reduction in slamming coefficient, aeration may show resonating effects by altering other characteristics of the slamming force such as rising time.

Summary chapter 5

- This chapter presents an extensive investigation of the effects of aeration and hydroelasticity on slamming loads and cylindrical shells' structural responses during a water entry event.

- The peak slamming pressure/force has a linear relation to the logarithm of the cylindrical shell's eigenfrequency and increases with the increasing cylindrical shell's stiffness/eigenfrequency.

- Unlike the observations on water entries of plates reported in chapter 4, the variability of slamming pressure/force as a function of cylinder flexibility does not decrease meaningfully in the presence of aeration, which means, compared to plate slamming, there is less interdependence between water compressibility and local flexibility in slamming of cylindrical shapes.

- A high-frequency pressure oscillation in pure water entry simulations was observed, caused by the cycles of compression and expansion of the trapped air beneath the cylinder. This phenomenon was also reported in experimental studies with less intensity. The oscillations were much less intense in the presence of aeration in water.

- Aeration caused up to 333% extension of the slamming force's rising time, but it did not affect the slamming load's total duration, unlike the plate entries.

- Impact force impulse has low sensitivity to the variation of aeration and local flexibility of the cylindrical structure. For the impact velocities of 5.5 m/s and higher, the variation of impulse due to aeration and cylindrical shell's flexibility is less than 10%.

- Aeration has an intensive damping effect on the response strain cylinders. It also reduces the contribution of higher eigenfrequencies substantially in the response. In cases with 0.5% aeration, the maximum response is very close to the corresponding values in pure water entries.

6 Numerical study of pure/aerated water entry of elastic cylinders

In chapters 4 and 5, the interacting effects of local hydroelasticity and aeration on the slamming load characteristics and structure's local responses were systematically studied. Apart from local vibrations, the global responses of the structure may affect the slamming load and vice-versa. As mentioned in chapter 3, implementing a complete 3D model of a structure, even a monopile, in strongly coupled interaction with breaking waves is computationally very expensive and out of scope for the present study. Therefore, in this chapter, a new simplified model is introduced to approach the problem with much less computational effort. The chapter continues by explaining this model. The model has been validated against the experimental data presented by Wienke and Oumeraci (2005).

6.1 A simplified FSI model for water impact

In most experimental investigations on breaking wave interactions with fixed offshore structures, the model structure is significantly stiffer than the prototype, and instead of modeling soil support, the structure is restrained by force transducers at the top and bottom of the structure (Figure 6.1 (b)). This system acts dynamically like a single degree of freedom (SDOF) system. The total hydrodynamic force from the wave impact, which
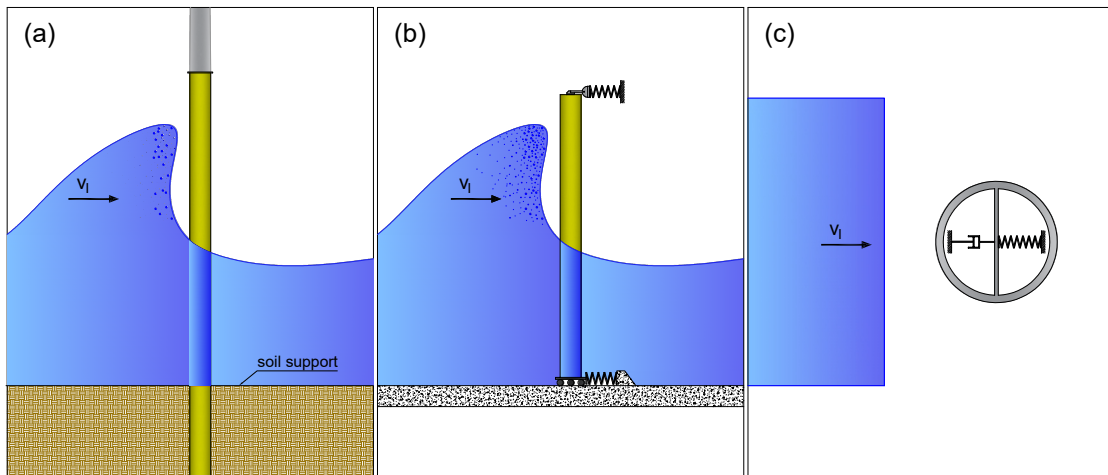
Figure 6.1: Sketches of (a) a prototype monopile, (b) a monopile experimental model, and (c) the proposed simplified two-dimensional model of a monopile.

cannot be directly measured, is therefore calculated by an iterative algorithm in which a guessed force time history is modified until the response calculated by convolution of the guessed force with the response function of the SDOF system is close enough to the measured response. This simplified experimental model can be further simplified into a 2D concept, as depicted in Figure 6.1 (c). A two-dimensional body of water moves with a constant velocity toward a SDOF system consisting of a rigid cylinder constrained by a spring-damper system. This model can be implemented with reasonable numerical resources available for the present study, and it can provide interesting insights into the slamming problem, among which the following are pointed out:

1. The evolution of inline slamming force can be directly obtained along with other hydrodynamic details around the cylinder;

2. Interaction of a specific structural eigenfrequency with the impacting water and the characteristics of loading and vibration caused by this interaction can be observed, and in addition, in the absence of interfering effects of complex parameters which are present in a 3D model such as the approaching wave characteristics, the role of aeration in the interaction can be investigated;

3. The model provides the possibility to study the effects of existing vibration of the structure, due to a successive slamming event, on the slam loading and response of the structure; and finally

4. The proposed model can investigate the effects of cylinder surface roughness on pressure evolution characteristics in time and space during the slamming events.

The first two aspects have been studied in this chapter. In the following section, the performance of the proposed 2D model is studied using the experimental data presented in Wienke and Oumeraci (2005), and later, the interaction of this system with different eigenfrequencies with impacting water body has been investigated.

6.2 Validation study

In the present validation study, the results of the large scale slamming experiments carried out in the large wave flume (GWK) of the Coastal Research Center (FZK) in Hannover and presented by Wienke and Oumeraci (2005) has been used. In those experiments, Gaussian wave packets were generated in the water depths of 4 to 4.25 m to make a focused breaker at specific locations near the test cylinder. The breaking waves were all plunging breakers with the celerity of around 6 m/s and near breaking height (H_b) of 2.2 m to 2.8 m. The characteristics of generated breaking waves are shown in Figure 6.2. The installation system for the steel test cylinder with 0.7 m diameter was like the Figure 6.1b sketch, in which force transducers at the top and bottom of the cylinder allowed it to oscillate in the transverse direction. The cylinder was tested in five different yaw angles; however, this
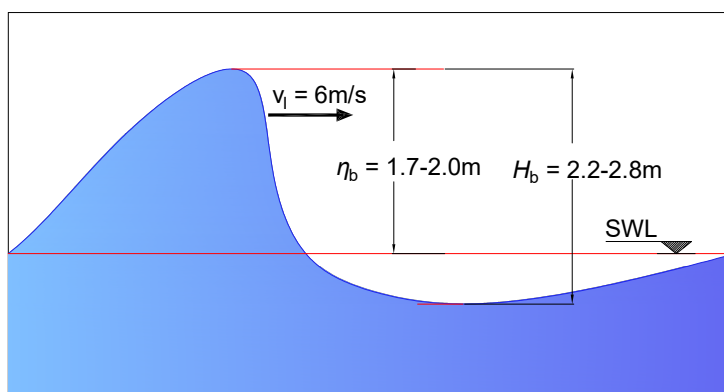
Figure 6.2: Characteristics of generated breaking waves in the experiments of Wienke and Oumeraci (2005) (Drawing by the author).

study focuses on the experiments with the vertical cylinder. The natural frequency of the system inside water measured by impacting a concrete block to the submerged cylinder was 11 Hz for the upright mode. The main measurements of the experiments concerning this study were:

1. Local point pressure time-series on the surface of the cylinder recorded by 55 pressure transducers, which were placed at the front line and on 3 circular arrays, at heights of wave through, still water level, and wave crest; and

2. Response of the system recorded by force transducers at the bearing positions.

6.2.1 Numerical simulation setup

Figure 6.3 depicts the numerical domain concept for the proposed water impact model, in which the fluid domain is a two-dimensional channel with one input and one output boundaries. The channel is 1.4 m wide and 21.4 m long, and the cells' width in the third dimension is 0.01 m. The reason to define a relatively large length for the channel is to prevent the reflected pressure waves generated in the impact area to interfere with the loading. This additional length is mostly on the side of the water front and has relatively low mesh resolution. The solid domain consists of a stiff cylinder attached through a stiff shaft to the middle of a flexible clamped-end beam. The beam plays the role of the spring-damper system in the 2D concept of Figure 6.1 (c). The cylinder is posed in the middle of the channel's width near the channel's output boundary. The simulation duration was set to cover the slamming load and the first two response cycles of the structure.

The numerical schemes applied in this chapter's simulations were the same as that in the simulations in chapter 4 and 5 and are described in chapter 3.
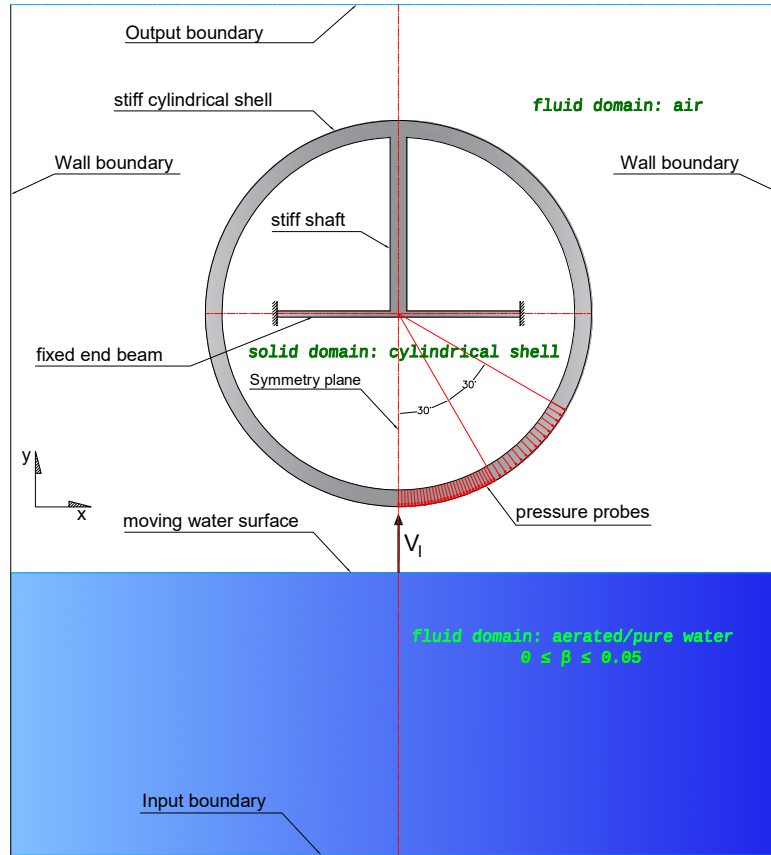
Figure 6.3: Simulation domain concept for 2D water impact model.

Boundary and initial conditions

The water surface in the channel is initially horizontal and, for the sake of saving computational time, close to the cylinder's lowest point with an initial distance of 2 cm. The whole water body has an initial velocity of 6 m/s (equal to the mean wave celerity in the experiments) in the upward direction toward the initially motionless cylinder.

The gravity force direction was set to be perpendicular to the domain and did not affect the simulation.

The boundary conditions for fluid and solid field variables are given in Table 6.1. As the table shows, a constant and uniform water flow with 6 m/s velocity enters the domain at the Input boundary. In order to reduce the computational time, a symmetry plane boundary condition was applied to the simulations.

Table 6.1: Boundary conditions for solid and fluid variables.

Boundary name	$\boldsymbol{u}_s$	$\boldsymbol{v}_f$	p	α_1	α_2
Wall	-	Fixed value, $\boldsymbol{0}$	Zero gradient	Zero gradient	Zero gradient
Solid-fluid interface	Traction-displacement	$\dot{\boldsymbol{u}}_s$	Zero gradient	Zero gradient	Zero gradient
Input	-	6 m/s (normal)	Zero gradient	1	0
Output	-	Free Inlet/outlet	Fixed value, $10^5\ Pa$	Zero gradient	Zero gradient

Specifications of the SDOF system

The main structural specifications of the SDOF system are listed in Table 6.2. As in chapter 5 and with the same argument, fiberglass material is chosen for the structural system. The system's geometrical properties were defined so that the submerged system's natural frequency had to be equal to that indicated for the vertical pile in the experiments (i.e., 11 Hz). The natural frequency and stiffness of the system were determined by *in vacu* and submerged free vibration simulations. The force transducers' damping coefficient in the experiments has not been indicated in any relevant document; however, since the hydrodynamic damping is substantially greater than the system's structural damping, the structural damping has been neglected in this study.

Table 6.2: Main structural specifications of the SDOF system.

Young's modulus (GPa)	33.2
Poisson's ratio (-)	0.28
Cylinder outer diameter (m)	0.7
Cylinder thickness (m)	0.13
Shaft thickness (m)	0.03
Beam length (m)	0.4
Beam thickness (m)	0.01
Natural frequency *in vacuo* (Hz)	17.7
Natural frequency in water (Hz)	11.1
Stiffness (N/m)	67160
Density (kg/m^3)	2250

Numerical probes

The following numerical probes were mounted in the domain to record the required field data at every time-step of the simulation.

1. Pressure probes; 46 pressure probes were arrayed on the outside surface of the cylinder from the lowest point (i.e., stagnation point) with perimeter angle 0° to 60°. The angular steps of the probe locations were 1° for the 0° to 30° interval and 2° for the interval of 30° to 60°.

2. Total force probe; This probe recorded the total hydrodynamic force by calculating the integral of fluid pressure around the cylinder-fluid interface.

3. Deflection probe, which recorded the deflection of the beam at the middle span.

6.2.2 Analysis of impact pressure

At first, in this section, the experimental pressure measurements are compared with the present numerical model results, and later, more details of the evolution of the pressure field are discussed.

Figure 6.4 compares the impact pressure measurements of the present numerical simulation with that in the experiment at the angular positions of 0°, 15°, and 30°.

At 0°, the numerical model reaches the peak pressure of 13.1 bar, which is reasonably close to that in the experiment (14.4 bar). After the peak, the pressure oscillation can be seen in both time histories, where secondary pressure peaks near 3.5 bar are observable. However, the oscillation in the experiment seems to be vanished rapidly after the second peak, while the rate of decline in the post-impact oscillation of numerical pressure is considerably slower. The causes of such observation have been discussed in chapter 5, which also apply to the present simulation.

At 15° perimeter angle, the numerical model shows a good agreement with the experimental data. The peak pressure values presented in Table 6.3 have a near 6% difference. A noticeable course of variation similarly seen in both the numerical and experimental time series is a very short rising time compared to the rising time of peak pressure at 0°. This can be explained by the formation of two mirroring jet flows rising beneath the cylinder, where a substantial pressure gradient forms at the root of the jet flow and moves very fast with it. In contrast, the falling time of impact pressure seems to be longer compared to 0°. The post-impact pressure oscillation in 15° position is lower in both datasets.
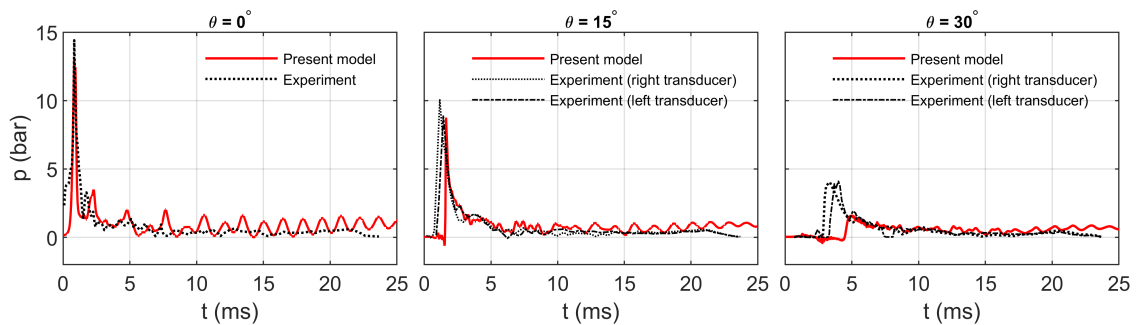
Figure 6.4: Time histories of impact pressure in the GWK experiments and present simulation at three angular positions of 0°, 15° and 30°.

Table 6.3: Comparison of peak impact pressure values at different positions measured in the GWK experiments and the present numerical model.

	P_{max} $(\theta = 0°)$ (bar)	$P_{max}(\theta = 15°)$ (bar)	P_{max} $(\theta = 30°)$ (bar)
Numerical simulation	13.1	8.9	1.6
Experiment	14.4	9.5 (average)	4.0 (average)

At 30°, the numerical impact pressure starts to rise by about 1 ms later, and its peak value is 60% lower than that in the experiment. It is worth mentioning that Wienke's theory also significantly underestimates the peak pressure at this point. Wienke did not suggest any explanation for this difference, which is reasonable since we have not enough information about the flow during the experiment for hypothesizing a possible cause.

The GWK experiments did not provide a detailed view of the pressure distribution around the cylinder. Taking the theory into account, Wienke considered the maximum impact pressure to occur at 0° position (i.e., stagnation point of the cylinder); However, the measured pressure value at this point is far less than the theoretical value. Wienke identified the air entrapment, which is also referred to as the "cushioning effect," as the most likely cause of that substantial difference. Figure 6.6 offers evidence for this claim. The Figure shows six snapshots of the present simulation taken from the important moments of the impact. The first snapshot, taken at $t = 0.0\,R/v_I$, shows that small pockets of air are entrapped between the cylinder and water surfaces at the beginning of the encounter of two surfaces. The compression of entrapped air reduces the impact pressure at air layer positions. The second snapshot, taken at the time near to the occurrence of maximum impact pressure, shows that the air layer is extremely compressed. The highest pressure
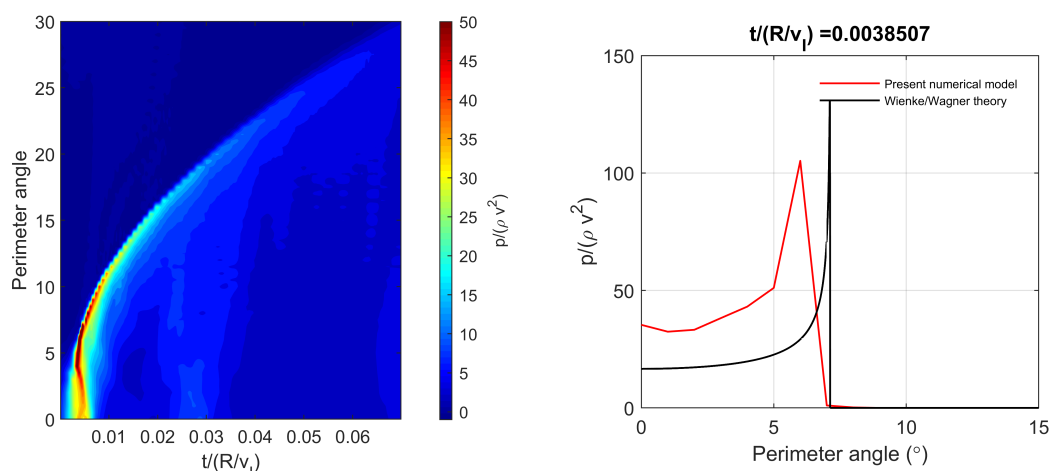
Figure 6.5: Left: Pressure distribution around the cylinder surface as function of time. Right: Pressure distribution around the cylinder surface at the time of peak pressure ($t = 0.00385\,R/v_I$).

seems to be shaping at the region outside of the entrapped air region between 0° to near 5°. This becomes clearer by observing Figure 6.5, in which the variation of pressure along the cylinder perimeter is drawn as a function of time. As the Figure shows, the pressure almost simultaneously hikes at a perimeter between 0° and around 4°. At this neighborhood, the pressure seems to vary more smoothly than its variation at points after 4° position, which may be considered the effect of higher compressibility of the air layer at this region.

Figure 6.5 (Right) presents the simulated pressure distribution around the cylinder at the moment of maximum pressure ($t = 0.00385\,R/v_I$) together with the distribution of slamming pressure calculated by Wagner/Wienke theory. The simulation and theory's peak values are relatively close, while the simulation shows significantly higher pressure values at the interval of 0° to 5°, which can be interpreted as the effect of the compressed air layer.

Similar to what was stated in chapter 5, we may expect that the entrapped air region in the simulation is considerably larger than what may be developed in the real world situation. however, it may be implied that pressure values higher than that recorded at 0°, may have occurred in the experiment in an area between 0° to 10° perimeter angles which were not recorded due to measurement limitations.

6.2.3 Analysis of impact response

Comparing the present SDOF system's response with the measured response in GWK experiments is also crucial since Wienke applied the measured response to determining the total force. Figure 6.7 presents the system's response to the slamming impact in the simulation in terms of mid-span deformation of the flexible beam and the equivalent response force F_l calculated by the system's stiffness. As may be expected, the maximum response occurs in the first half-period of the oscillation, and after that, the response is damped out by the hydrodynamic damping force. The oscillation frequency seems to be reduced after the first half-period, which is the effect of the cylinder's gradual submergence and the consequent increase in hydrodynamic mass. The response force F_l is a line force, and in order to compare it with the total experimental wave impact responses, we may multiply it by the effective height of the wave front:

$$F = \lambda\,\eta_b\,F_l, \tag{6.1}$$

where η_b is the elevation of breaking wave crest with reference to the still water level and λ is a coefficient named "curling factor".

The curling factor is an empirical coefficient depending mostly on the shape of the breaking wave at the moment of impact (Wienke and Oumeraci, 2005). Wienke (2001) determined the curling factor for each impact incident so that the calculated response from the convolution of theoretical force became equal to the pile system's actual measured response. In that
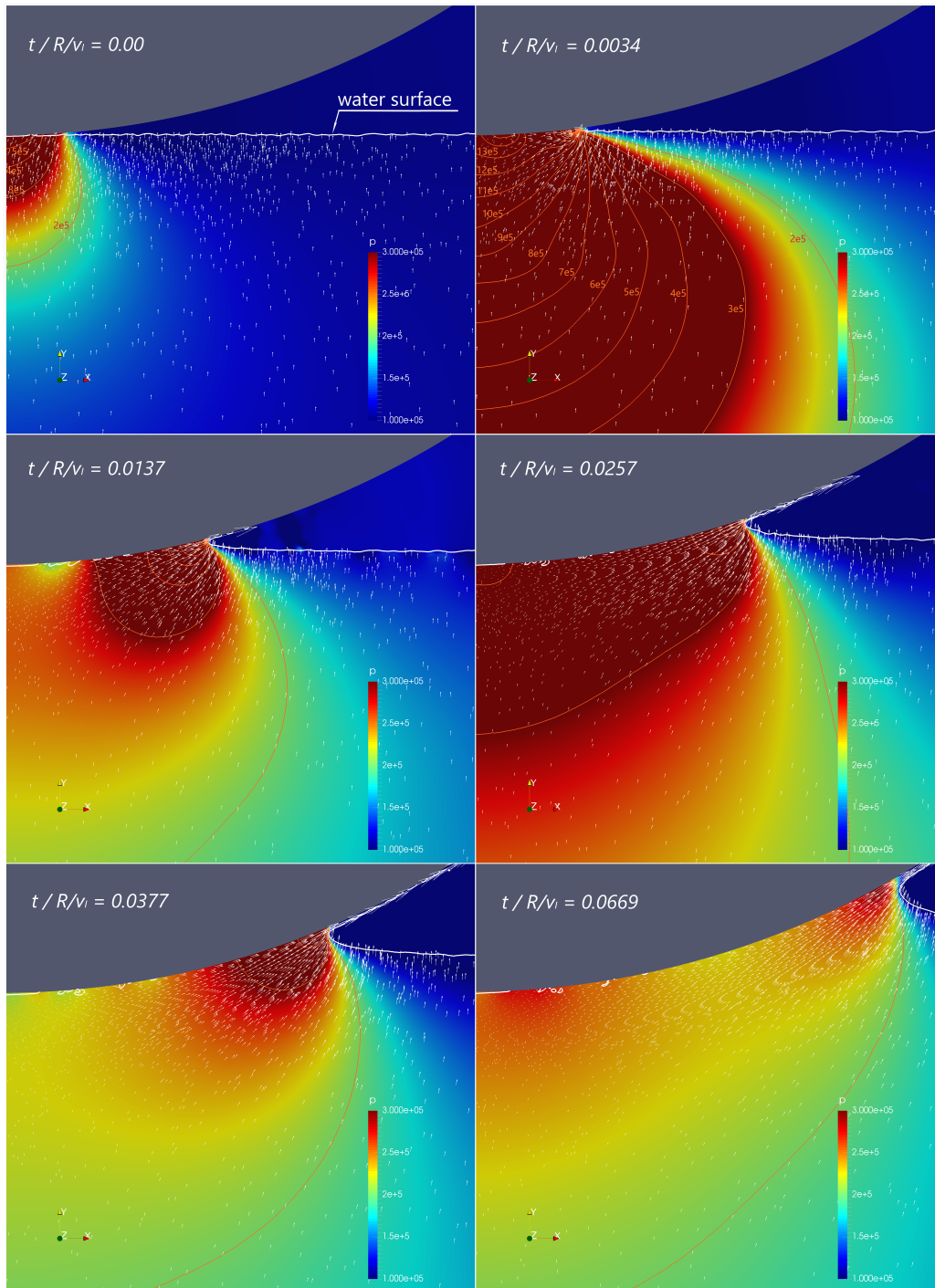
Figure 6.6: Simulation snapshots showing the development of pressure and velocity fields and water surface near the impact area. The plots show important processes during the early stage of the impact, such as the formation of peak pressure, successive cycles of contraction-expansion of trapped air and the formation of water jet beneath the cylinder.
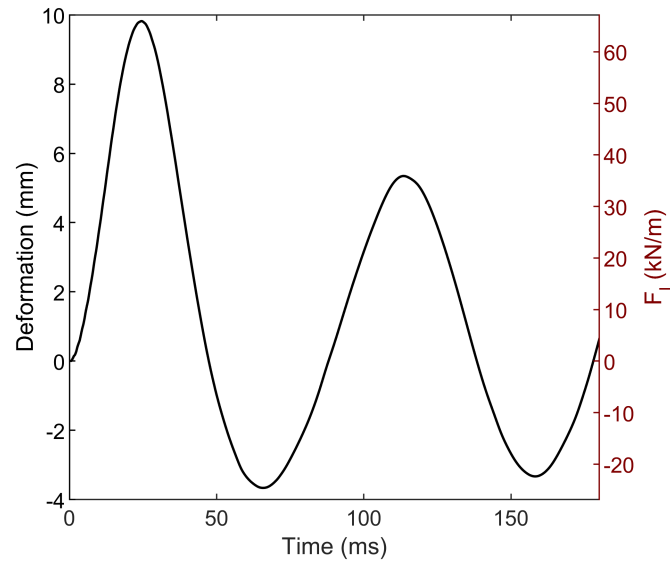
Figure 6.7: Time history of the simulated response of the numerical SDOF structural model to the water impact.

way, he suggests a range of $0.26 - 0.46$ for the curling factor of near-breaking/breaking waves with a vertical pile. By applying the above-recommended range of curling factor in (6.1), the numerical model's response is transformed into total force and can be compared with GWK measured responses, as implemented in Figure 6.8.

The experimental responses shown in Figure 6.8 are obtained from three wave impact incidents with the same water depth of $4.0\ m$. The left plots show the profile of the wave right before the moment of impact. The crest elevation (η_b) of the waves are very close in a range of $1.96 - 1.99\ m$. Since the curling factor has been defined with an empirical validity range, the numerical responses drawn in the right plots are calculated with three values of λ, namely the minimum value of 0.26, the mean value of 0.36, and the maximum value of 0.46. A good agreement between the numerical and experimental responses can be observed in terms of the overall shape of the response force's variation and peak values. It can be observed that the experimental system was not a perfect SDOF system, and a secondary frequency is visible in the measurement, which dissipates quickly after the first half period.

The comparisons imply that the simplified numerical model can be a reliable tool, though with limitations, in further investigation of the slamming phenomenon, part of which has been conducted and presented in the following sections of this chapter.
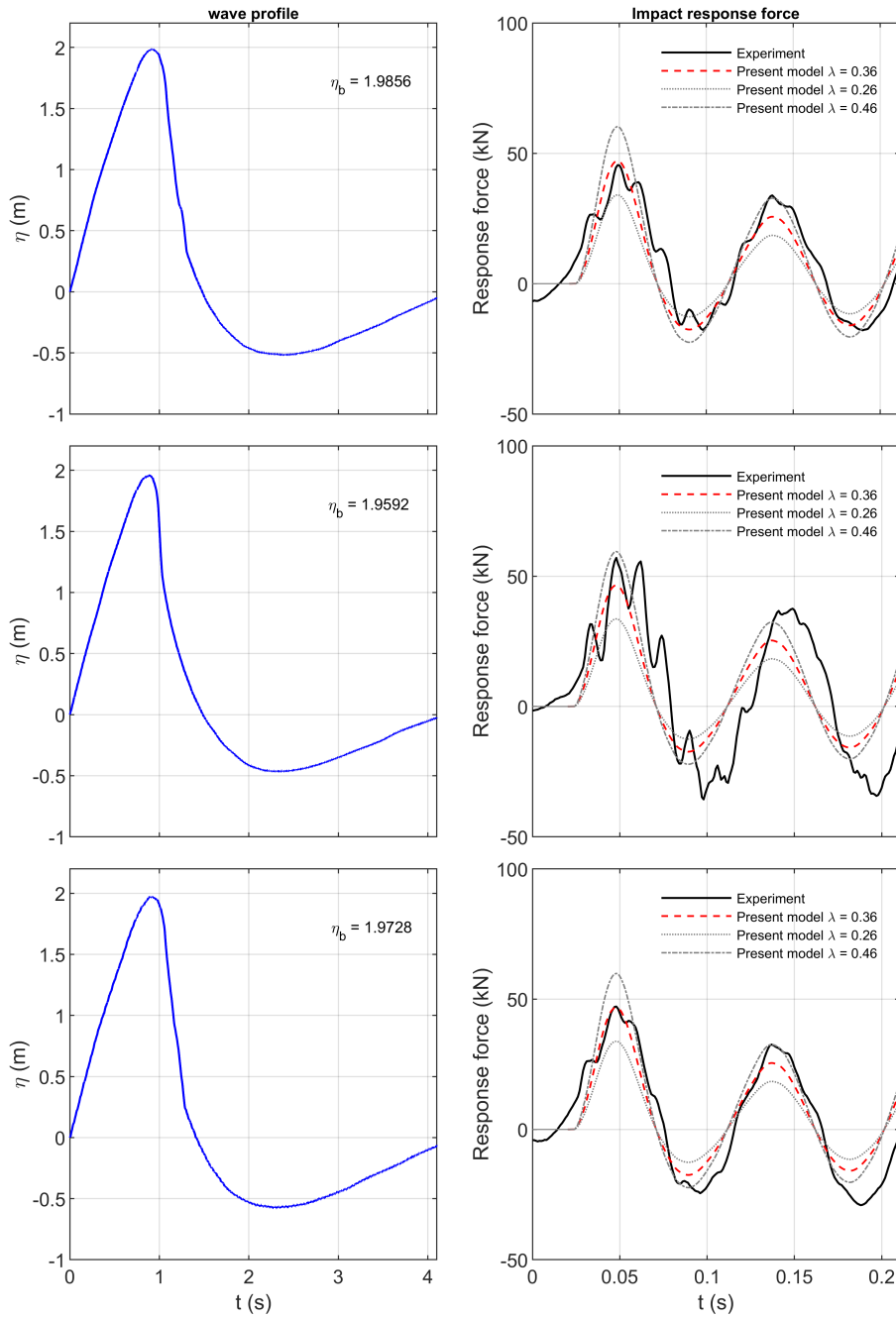
Figure 6.8: Comparison of experimental dynamic response forces measured in GWK experiments during the impact of waves with profiles shown in the left plots to present numerical force calculated with three curling factor values.
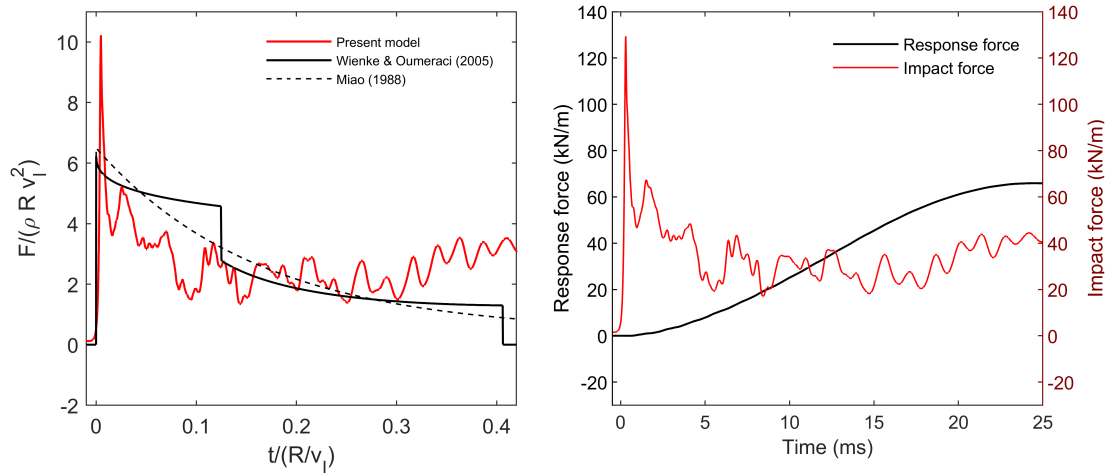
Figure 6.9: Left: time history of the impact force derived from the numerical simulation in comparison with the theoretical suggestions by Wienke and Oumeraci (2005) and Miao (1988). Right: time series of numerical impact force and the synchronous response of the 2D model.

6.2.4 Analysis of slamming force

The actual exerted wave slamming forces in the experiments that caused the dynamic responses shown in the previous section are unknown due to the measurement limitations. Therefore, in Figure 6.9 (left), the impact line force resulted from the numerical simulation is compared with the theoretical suggestion of Wienke and Oumeraci (2005) as well as the Miao (1988) formula. The numerical force has a very sharp peak at the beginning of impact with a very short duration of less than 1 ms and significantly larger than both theories. As shown in chapter 5, the value of this peak force is directly related to water compressibility. After the short-duration high peak, the numerical impact force fluctuates near the values of the plotted theoretical formulas and gradually declines until around $t = 0.25 \, R/v_I$ (or 14.5 ms). Near that time, the numerical force rises again and reaches a maximum value around the maximum response time (see the right plot of Figure 6.9). This part of the numerical force is affected by the hydrodynamic inertia force caused by the cylinder's acceleration. In the right plot of Figure 6.9, the cylinder's response is drawn along with the impact force. The response force seems to have a very short delay of about 0.7 ms compared to the impact force. This delay occurs because the cylinder shell is not entirely rigid and, though very stiff, it still deforms at the beginning of impact, and this deformation causes the mentioned delay in the response of the support beam.

6.3 Effect of global vibration characteristics and aeration on the slamming pressures, forces and structural responses

The validation study presented above showed that the suggested simplified model could present valuable data on the physics of the interaction of a flexible SDOF cylindrical structure with impacting waves. Thus, to study the effect of global structural vibration eigenfrequencies along with aeration on the characteristics of loading and structural response during a wave impact, the simplified model was applied in a parameter study. $5{\times}3$ numerical simulations of the impact of non-aerated and aerated water (with two aeration levels of 0.5% and 5%) on five SDOF cylinders with different eigenfrequencies (i.e., $f_1 = 18$, 26, 58, 99, and 150 Hz), as well as a semi-rigid cylinder (i.e., $f_1 = 30\ kHz$) were carried out. The initial and boundary conditions and numerical probes of the simulations were similar to that in the validation study. The results of the parameter study are discussed in the following sections.

6.3.1 Impact pressure

Figure 6.10 shows the variation of pressure distribution around the cylinder during the high-pressure phase of impact is drawn for the semi-rigid cylinder and the most compliant SDOF cylinder ($f_1 = 18\ Hz$) under the impact of non-aerated as well as aerated water. The figure reveals the effects of aeration and global hydroelasticity on the variation of pressure.
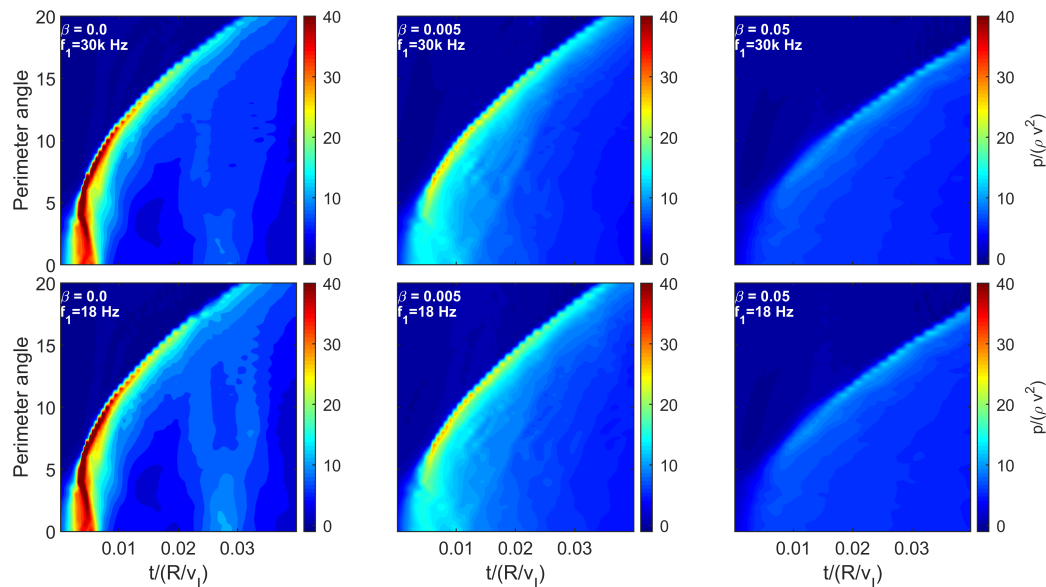
Figure 6.10: Variation of pressure distribution around the cylinder in time during the high-pressure phase of impact of non aerated (left), 0.5% aerated (middle) and 5% aerated (right) water on the semi-rigid (up) and compliant (down) SDOF cylinder cases.

In contrast with the elastic cylinder water entries in chapter 5, the impact pressure seems
to be insensitive to the cylinder's global flexibility, as pressure distributions of semi-rigid
and compliant cases seem very similar in all impact incidents. On the other hand, the effect
of aeration is very similar to the entry cases of chapter 5, in which the aeration flattens
the peak of the pressure variation around the cylinder.

Table 6.4: Peak impact pressure values occurred on aerated and pure water impact on semi-
rigid cylinder and the most compliant cylinder ($f_1 = 18\,Hz$). The values within parentheses
show the percent changes of aerated case value with reference to the corresponding non-aerated
case.

	Semi-rigid cylinder		Compliant cylinder ($f_1 = 28\,Hz$)	
β	$p_{max}(bar)$	$p_{max}/(\rho v_I^2)$	$p_{max}(bar)$	$p_{max}/(\rho v_I^2)$
0.000	39.5	106.9	38.9	105.2
0.005	11.3 (-71%)	30.5	11.2 (-71%)	30.2
0.050	4.9 (-88%)	13.1	4.9 (-87%)	13.1

Table 6.4 presents the values of maximum impact pressure on the impact incidents of
Figure 6.10. The maximum pressure of the non-aerated water impact case is considerably
higher than that at 0° perimeter point of the cylinder presented in Table 6.3. This high
pressure occurs near 6° perimeter angle, located immediately after the trapped air layer.
The rates of peak pressure reduction in the presence of aeration are of the same order as
that in the cylinder entry study in chapter 5.

The pressure distribution around the cylinder at the time of peak pressure occurrence is
depicted for non-aerated, and 0.5% aerated water impacts on semi-rigid and compliant
cylinder models in Figure 6.11. The figure also shows the pressure distribution at the
theoretical time of impact beginning (i.e., when the water body touches the cylinder surface)
and four later time steps with the increments of $0.001\,R/v_I$ (the dotted lines). Observation
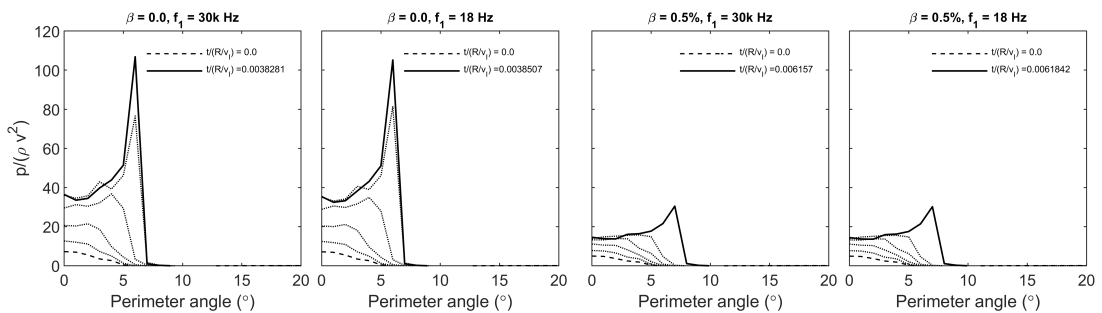
Figure 6.11: Profiles of pressure around the cylinder at $t/T_i = 0.0$ (dashed line), $t/T_i =$
0.001-0.004 (dotted lines with intervals of 0.001), and at the moment of peak pressure (solid
line) resulted from pure and aerated ($\beta = 0.5\,\%$) water entry of semi-rigid and compliant
($f_1 = 18Hz$) cylinders.

of the figure shows that there is a negligible difference between the semi-rigid and compliant cases. Apart from that, 0.5% aeration has significantly reduced the pressure intensity, particularly at the point of peak pressure, and also, it has shifted the time and location of the peak pressure.

6.3.2 Impact line force and structural response

Figure 6.12 provides an overview of the simulation results in terms of slamming forces and the structural responses of 5 cylinder models with dry eigenfrequencies of 18, 26, 58, 99, and 141 Hz, under the impact of non-aerated and aerated water. As seen and explained in Figure 6.9, all the impact responses have a very short delay of about 0.7 ms caused by cylinder shell deformation. Like impact pressure results, the peak impact force seems to be indifferent to structural eigenfrequency in all cases. However, the impact of force variation is affected moderately by structural responses.
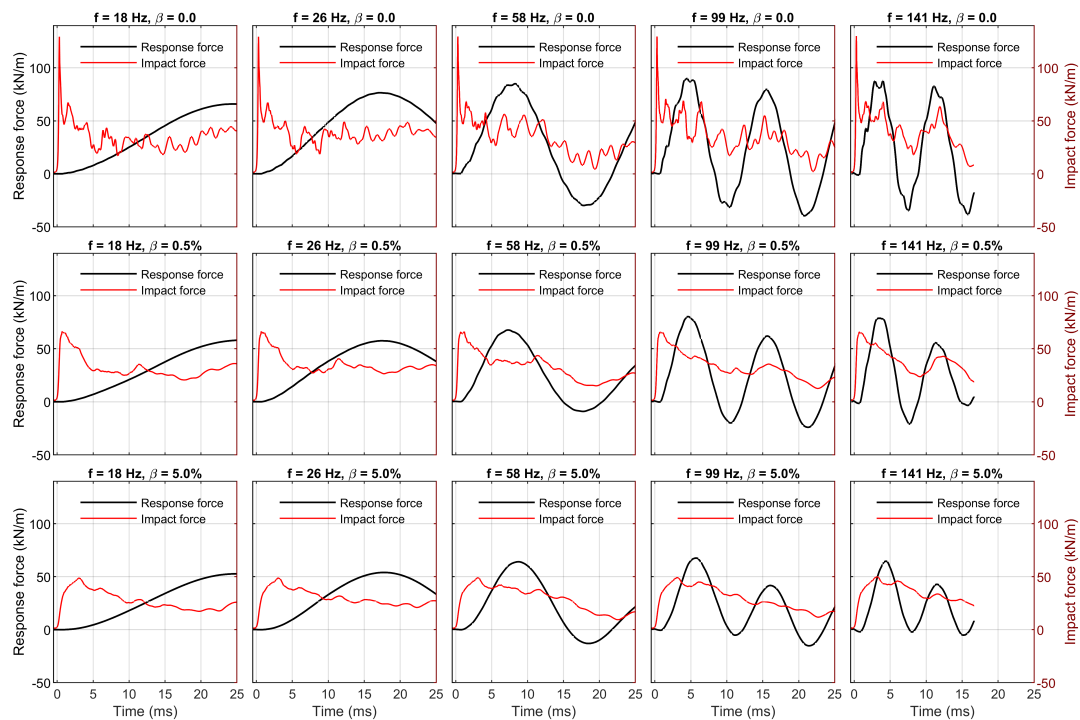
Figure 6.12: Time histories of slamming force and structural response for 5 cylinder models under the impact of non-aerated water (upper row) and aerated water (middle and down rows).

The spectral densities of the impact forces, drawn for all simulations on five cylinder models in Figure 6.13, may show better the effect of the structural vibration eigenfrequency on the impact force. All the spectra have a peak at the natural frequency of the models. Furthermore, in Figure 6.13, the share of structural eigenfrequency in the force power

spectrum declines in the aerated water impact cases.

Table 6.5 summarizes the main quantities related to slamming force and structural response of models shown in Figure 6.12. As shown in the table, the wet eigenfrequencies are smaller than the dry values for all models. The table values also confirm that the peak slamming force is not affected by the vibration properties (i.e., eigenfrequency) of the cylinder models. This is also valid for the force impulses in non-aerated and aerated water impacts. On the other hand, the maximum response value varies with structural eigenfrequency. To better see the whole picture, Figure 6.14 depicts the maximum response values in terms of dynamic response factor, which is defined as the ratio of maximum response to the maximum impact force as a function of dry eigenfrequency.

Table 6.5: Main results of the simulation for 5 compliant cylinder models. The values within parentheses show the percent changes of aerated case value with reference to the corresponding non-aerated case.

	1	2	3	4	5
Dry eigenfrequency (Hz)	18	26	58	99	141
Wet eigenfrequency (Hz)	11	20	40	75	100
Peak impact force, $\beta = 0$ (kN/m)	132.7	132.6	132.5	132.8	133.0
Force impulse, $\beta = 0$ (Ns/m)	5.6	6.2	6.8	6.6	6.6
Peak response, $\beta = 0$ (kN/m)	65.9	76.6	85.1	89.9	87.8
Rising time, $\beta = 0$ (ms)	0.3	0.3	0.3	0.3	0.3
Peak impact force, $\beta = 0.5\%$ (kN/m)	66.8 (-50%)	67.0 (-49%)	66.3 (-50%)	66.2 (-50%)	66.4 (-50%)
Force impulse, $\beta = 0.5\%$ (Ns/m)	5.4 (-4%)	5.9 (-5%)	6.3 (-7%)	6.1 (-8%)	6.3 (-4%)
Peak response, $\beta = 0.5\%$ (kN/m)	58.1 (-12%)	57.5 (-25%)	67.7 (-20%)	80.3 (-11%)	78.8 (-10%)
Rising time, $\beta = 0.5\%$ (ms)	0.7 (+133%)	0.7 (+133%)	0.7 (+133%)	0.7 (+133%)	0.7 (+133%)
Peak impact force, $\beta = 5.0\%$ (kN/m)	48.7 (-63%)	48.7 (-63%)	48.9 (-63%)	49.1 (-63%)	50.0 (-62%)
Force impulse, $\beta = 5.0\%$ (Ns/m)	5.0 (-11%)	5.2 (-16%)	5.8 (-14%)	5.6 (-15%)	5.6 (-15%)
Peak response, $\beta = 5.0\%$ (kN/m)	52.7 (-20%)	54.0 (-29%)	64.0 (-25%)	67.6 (-25%)	64.6 (-26%)
Rising time, $\beta = 5.0\%$ (ms)	3 (+900%)	3 (+900%)	3 (+900%)	3 (+900%)	3 (+900%)

Observing the three plots of Figure 6.14 reveals that for all aeration levels, the response factor increases with eigenfrequency until reaching a maximum at 99 Hz, which seems
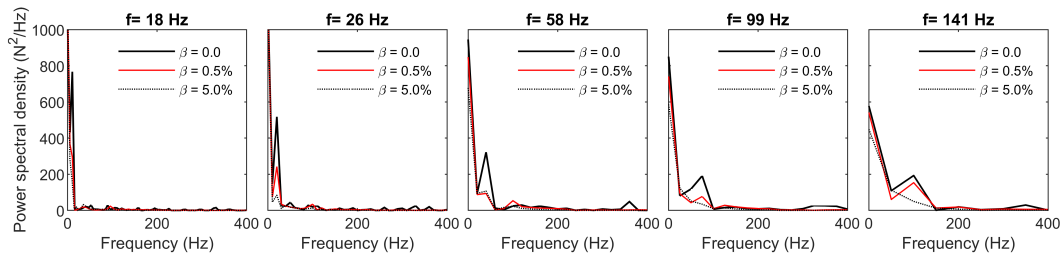
Figure 6.13: Power spectral densities of impact force for 5 cylinder models under the impact of non-aerated and aerated water.
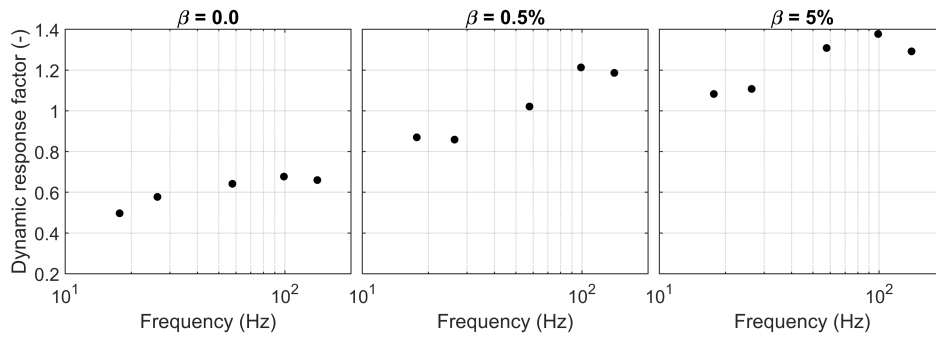
Figure 6.14: Dynamic response factor of the SDOF cylinder models as function of dry eigenfrequency for non-aerated (left) and aerated (middle and right) water impact simulations.

to be the resonance eigenfrequency within the simulated range. It is counter-intuitively interesting that in all aeration levels, the resonating eigenfrequency is the same.

Survey of results shown in Table 6.5 also reveals that the curbing effect of aeration on the models' peak response is much less intense than that on the peak impact forces. Figure 6.15 shows better the effect of aeration on the major characteristics of slamming force and response. In the left plot, the variation of maximum response is drawn with respect to the aeration level. As shown, the mean non-dimensional peak response reduces from 6.26, in non-aerated water impacts, to 5.29, in 0.5% aerated water impacts (i.e., near 15% reduction rate); while the corresponding reduction rate of mean slamming coefficient, as shown in the right plot, is near 50%. The left plot also shows the ratio of force impulses to the mean force impulse of the non-aerated impacts as a function of aeration level β. Similar to the results of water entries in chapter 4 and 5, aeration seems to have much less altering effect on the force impulses of present water impacts.
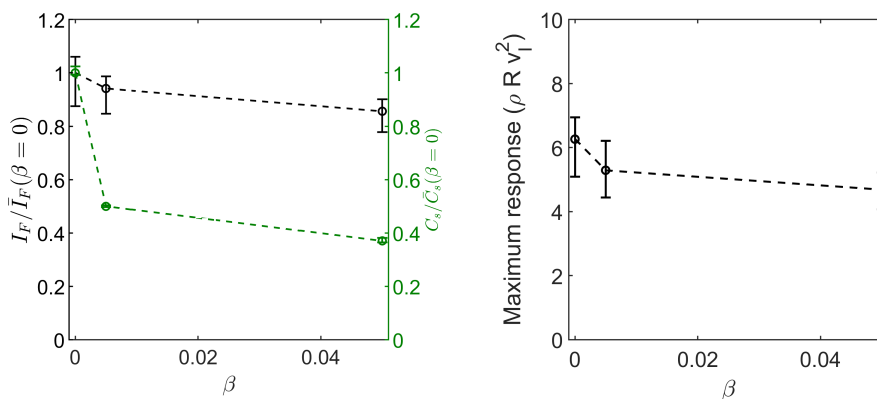
Figure 6.15: Left: Relative mean impact force impulse I_F and slamming coefficient C_s as functions of aeration level for all simulations. Right: Non-dimensional mean maximum response as function of aeration level.

6.4 Conclusions

This chapter introduces a simplified numerical modeling concept to investigate the coupled interaction of a SDOF cylindrical structure with a body of water impacting it, a simplified model of wave slamming on a cylindrical structure. The numerical model has been validated through comparison with the large-scale experimental data.

The validated numerical model has been used in a parameter study to understand the effect of global structural flexibility with or without the existence of aeration inside water on the characteristics of slam loading and structural response during wave slamming events.

Observations on the impact pressure during the simulations showed that the peak value and distribution of slamming pressure are not affected by the eigenfrequency (i.e., flexibility) of the SDOF cylinder. An air cushion developed in all simulations at the bottom of the cylinder between 0° to 5° angular positions, which causes the peak slamming pressure to occur at near 6° position in all simulations. The cushioning effect of trapped air has also been reported by Wienke (2001), implying that higher pressures might have occurred in the experiments between 0° and 5° angular coordinated, which has not been recorded due to measurement limitations. The effect of aeration on peak pressure values and temporal and spatial development of slamming pressure is similar to what chapter 5 reported.

Investigation of the slamming force time series reveals that the structure's global flexibility has a negligible effect on load characteristics such as peak impact force, rising time, and the total duration of impact. However, the structural vibrations affect the force time history in the form of an additional inertia force that can be distinguished from the whole force signal. Similar to findings of chapter 5, aeration shows to cause a significant reduction in peak impact force (by up to 63% for 5% aeration in water), while it increases the impact force rising time up to 900%. On the other hand, the effect of aeration on the force impulse is much less intense as it declines by up to 16% when the water has 5% aeration.

The response of the SDOF system to slamming has a resonance eigenfrequency near 99 Hz. With this eigenfrequency, the system shows the maximum response to non-aerated as well as aerated slamming impact.

The study also shows that in relatively high aerated levels (5% in the study), the maximum response is meaningfully reduced (up to 29%); while in low aerated cases, the peak response is much closer to that in pure water impact, which implies that a combination of parameters such as rising time, force impulse and structural flexibility should be taken into account in addition to slamming coefficient for the dynamic analysis of structures under slamming.

Summary chapter 6

- A novel simplified model of wave slamming on an SDOF cylindrical structure was developed. The model could reproduce the slamming force and pressure time series of the large scale wave slamming on monopile experiments with a reasonable accuracy level. The validation study showed that the introduced simplified model could present valuable data on the physics of the interaction of a flexible cylindrical structure with impacting body of water.

- The simplified model was applied in a parameter study to investigate the effect of global structural vibration characteristics along with aeration on the characteristics of slam loading and structural response. a combination of three water aeration levels (0%, 0.5%, and 5%) with six eigenfrequencies of the SDOF structure was applied in the simulations.

- The parameter study revealed that the peak value and distribution of slamming pressure, as well as the peak value, rising time, and total duration of inline slamming force, are insensitive to the global flexibility of the structure.

- With the variation of structural eigenfrequency, the SDOF system's response to slamming has a maxima point near 99 Hz. This resonance eigenfrequency does not change with the variation of aeration level in the water.

- The peak slamming force reduced up to 63 % in aerated water impact simulations, but on the other hand, the slamming force rising time expanded up to 900 %. The effect of aeration on the impact force impulse is much less intense, and it declines up to 16 % in high aeration levels.

- The maximum structural response reduced up to 16% in high aeration impacts, while it was barely declined in the low aeration water impacts despite the large decline in peak impact force.

7 Conclusions and outlook

7.1 Conclusions

Slamming is still a source of uncertainties in the practice of planning and design of marine structures. Lack of knowledge in the role of interacting processes such as hydroelasticity and aeration is a major obstacle toward clearly addressing the slamming loads in practice. This thesis was initiated and developed around the following core practical questions.

- How and when should the hydroelasticity process, on local and global scale, be involved in the analysis of marine structures under violent wave slamming events?

- What is the role of aeration in the slamming process, and how it is involved in the coupled structure-fluid interaction during slamming events?

This chapter is dedicated to highlighting the key findings of this study based on the above questions, describing the major limitations of this work's methodology, and recommending further works to address the limitations and problems beyond the reach of this thesis.

Four main parts can be distinguished within the contents of this thesis. The first part (Chapters 1-3) consists of preliminary studies and preparation of tools developed for the numerical simulation series carried out in this thesis. The second part (Chapters 4-5) discusses the development and results of numerical studies on the local effects of hydroelasticity and aeration in slamming. In the third part (Chapter 6), the results of the numerical tool, developed to study the effects of global hydroelasticity along with the aeration parameter, are discussed.

7.1.1 Conclusions, part 1: preparation

Within this part of the work, a comprehensive review of the literature on slamming was carried out, which led to the specification of main knowledge gaps and raising the questions mentioned above. The defined objectives initiated in this part for the whole study are as follows.

1. Developing and validating a numerical model capable of simulating the strongly coupled interaction of a flexible structure and water with free surface, which may be aerated;

2. Systematic numerical study of slamming of basic geometries to investigate in detail the interconnecting effects of aeration and local hydroelasticity on the evolution of impact pressures/forces and the local responses of the structures;

3. Develop a simple way to investigate the effects of global structural response interacting with aerated/pure fluid during the slamming event.

4. Develop a basic conceptual framework for the dynamic analysis of ocean structures under wave slamming loads.

The first objective is dealt with in chapter 3, where a comprehensive review and analysis of the state-of-the-art numerical methods have been conducted. A combination of numerical methods was selected and implemented on the C++ numerical library of OpenFOAM.

The implemented numerical tool was validated against experimental data from available benchmark tests. The numerical model shows in the validation study the ability to capture the physics of hydroelasticity and the effects of aeration on fluid-solid interaction problems.

During the implementation and validation process, it was found that simulating in a three-dimensional setup is computationally very expensive (relative to the limitations of this work) and out of reach for this thesis, even for simple water entry simulations. Therefore all the simulation cases, including the validation tests, were carried out in two-dimensional form. The two-dimensional setup has apparent limitations that affect the results of the simulations. One of the major adverse side effects of the 2D setup was that the volume of air pocket that entrapped between the water and plate/cylinder bottom is larger than that observed in the experiments, and the entrapped air cannot escape as quickly as in real conditions. This may cause the pressure oscillations induced by the air pocket's contraction-expansion cycles to become more intense and last longer than expected. However, the validation study results show that even with such limitations, the 2D numerical model is capable of providing the required field data with reasonable accuracy for the present study.

7.1.2 Conclusions, part 2: the role of local hydroelasticity and aeration

Two similar systematic numerical parameter study reported in chapters 4 and 5 were carried out to investigate the interlinked effects of local hydroelasticity and aeration on the hydrodynamic impact loading and local structural responses. The numerical simulations were conducted in the form of water entry of basic shapes. In the first group of simulations, water entries of plates, and in the second group, water entries of circular shell sections were investigated. In the following, a summary of the key findings of both studies is presented.

- Both studies showed that flexibility has a noticeable reducing effect on peak values of slamming pressures and forces. This effect increases with increasing length in plates.

The cylinder diameter was not included in the parameter study. The reducing trend seems to be proportional to the logarithm of plate/cylinder eigenfrequency.

- In entry slamming of plates, the effect of plate flexibility on slamming load reduces significantly in the presence of aeration and almost vanishes for aeration levels over 5%. This may have important implications for the modeling since it seems in such situations where water is aerated, e.g., in breaking wave load impact, there may be no need to use a strong coupling for accurate assessment of hydrodynamic loads. This trend was not found in cylinder entry cases.

- In all cases of cylinder and plate water entries, flexibility has no significant effect on the rising time and total impact loading duration.

- Only a slight amount of aeration in water substantially reduces the maximum slamming pressures and forces, but on the other side, it elongates the rising time and duration of loading, which implies that the impact force impulse may not be affected as much as maximum forces.

- The peak impact pressure/force depends on the impact velocity and water compressibility, which changes significantly with the aeration level. This finding has led to new functional relations in terms of relatively simple power-law approximations, which has been derived for plates (Relations (4.1), for peak pressure, and (4.3), for peak slamming force) and cylinders (Relations (5.1), for peak pressure, and (5.3), for peak slamming force).

- Local structural response of plates and cylinders to slamming in the presence of aeration may be classified into high aeration and low aeration slamming responses. In high aeration cases ($\beta > 0.5\%$), the response is reduced significantly with respect to the non-aerated slamming. On the other hand, in some low aerated cases ($\beta \leqslant 0.5\%$), the maximum local structural response was observed to be very close to that of pure water entries, implying that, despite the reduction in slamming coefficient, aeration may show resonating effects by altering other characteristics of the slamming force such as rising time.

- In plate entry and cylinder entry simulations, aeration shows a damping effect on the response strain oscillations, which increases with increasing aeration level.

7.1.3 Conclusions, part 3: the role of global hydroelasticity and aeration

In the preparation phase of this work, it was discerned that the implementation of 3D simulations of wave impact onto the simplest form of structures such as a monopile with taking compressibility and FSI coupling into consideration need resources and time beyond the reach of the current thesis. Therefore, the third objective of the work was set to develop and validate a simplified model capable of showing the main characteristics of wave impact

loading and its interaction with the structure's global displacements. Chapter 6 introduced a simplified model of a monopile in the form of a single degree of freedom (SDOF) 2D cylinder-spring system. The numerical model was validated using the measurement data from large-scale experiments conducted by Wienke (2001) in the Large Wave Flume (GWK) of the Forschungszentrum Küste institute (FZK) in Hannover, Germany. The validation study shows that the numerical model can reproduce the impact loads and structural response with acceptable accuracy. Next, a numerical investigation on the effect of global structural flexibility in addition to aeration on the characteristics of slamming load and the structural response was carried out. The following is a summary of the main findings of this part of the thesis:

- The study shows that the SDOF system's global flexibility has no noticeable effect on the peak value of slamming pressure and its distribution around the cylinder. The system's flexibility also has a negligible effect on load characteristics such as peak impact force, rising time, and the total duration of slamming force.

- The structural vibration affects the time history of the force in the form of an additional inertia force that can be distinguished from the whole force signal.

- An air cushion developed in all simulations at the bottom of the cylinder between 0° to 5° angular positions, which causes the peak slamming pressure to occur at near 6° position in all simulations. The cushioning effect of trapped air has been reported by Wienke (2001), which implies that higher pressures might have occurred in the experiments between 0° and 5° angular coordinated, which has not been recorded due to measurement limitations.

- The study shows that in relatively high aerated levels (5% in the study), the maximum response is meaningfully reduced (up to 29%); while in low aerated cases (0.5% in the study), the peak response is much closer to that in pure water impact, which implies that a combination of parameters such as rising time, force impulse and structural flexibility should be taken into account in addition to slamming coefficient for the dynamic analysis of structures under slamming.

7.1.4 Conclusions, part 4: summarizing remarks

Based on the findings of this study, a basic framework can be established for the dynamic analysis of structures under breaking wave slamming attacks. Two scale modes of analysis may be distinguished from each other in practice, for which the following recommendations are stated.

Local effects of slamming; the study shows that local hydroelasticity and aeration have significant intertwined effects at the local level when the structure is flexible. Values of interest, such as peak value and the local evolution of impact pressure, maximum local response strains, and vibration characteristics, are affected by both

aeration and hydroelasticity. Therefore, in such analysis measures, it is recommended to consider both the strong coupling of fluid and structure and fluid compressibility. For locally stiff structures, hydroelasticity may not be an essential issue, but processes such as air entrainment and entrapment are important in determining local loading characteristics. Therefore for locally stiff structures, compressibility should be taken into account in the local slamming analysis.

Global dynamic analysis; in global scale, processes related to compressibility such as aeration and air entrapment are far more important than hydroelasticity. A significant percentage of wave impact events in real conditions may incorporate high aeration levels in the water, which has been shown to reduce the peak structural response and duration of vibration. On the other hand, low aeration wave impacts may cause resonated responses. Hence, in both deterministic and stochastic studies of wave impact dynamics, the compressibility parameter is important and should be considered in the analysis.

7.2 Outlook

Along with opening new insights into understanding the slamming phenomenon, this thesis exposed several challenging topics for further investigation, as listed below.

- One of the significant limitations of the current work was the impossibility of conducting three-dimensional numerical simulations of slamming since the local cell density in the impact area should be very high. Also, due to the compressible flow modeling, time-steps are very small. Further studies are needed to develop effective methods to reduce the computational resources needed for slamming simulations in a three-dimensional configuration.

- The most simple equation of state has been used for the numerical simulation of the fluid domain in the current work, which may cause larger than reality oscillations in pressure signals, particularly in cylinder slamming simulations. Studying the effect of different approaches toward the energy equation for the fluid domain on the outcome of such simulations would be valuable for future works.

- For the first time, the current research investigated the simultaneous and interacting roles of aeration and hydroelasticity on the slamming loads through numerical simulation campaigns on simple object geometries. Extending the current work to experimental investigations might be valuable for future research since there is no single experimental data on this combination of phenomena, which is crucial for validating numerical models and providing new insights beyond the present work's findings.

- As mentioned in chapter 2, the influence of scale in slamming dynamics has been recognized and is still under investigation by the research community. However,

it was beyond the reach of the present research to study the effects of scale in conjunction with aeration and structural deformations. Such an investigation is, therefore, suggestible for future research.

- In the present study, new functional relations were found to define the dependence of peak slamming forces/pressures on the impact velocity and the compressibility of water. However, further studies are needed with taking parameters such as length-/radius and mass of the plate/cylinder into account to generate general relationships for such object shapes.

- The simple structural model developed in the current work and presented in chapter 6 provides the possibility to study the effects of existing vibration of the structure on the slamming load and its interaction with the structure.

- The present research has shown that slamming load and structural responses are very sensitive to water compressibility variation induced by aeration in water. However, in the state of the art practice, such effects are not taken into account, which increases the level of uncertainties in the structure's design, operation and maintenance. Therefore more profound studies of the aeration process in seawater from the statistical and physical points of view will improve the loading process of offshore structures.

Bibliography

Aarsnes, J. V. (1994). An experimental investigation of the effect of structural elasticity on slamming loads and structural response. Technical Report Technology Report MT60 A95-0053,602119.00.01, Norwegian Maritime Technology Research Institute A/S, MARINTEK.

Agertz, O., Moore, B., Stadel, J., Potter, D., Miniati, F., Read, J., Mayer, L., Gawryszczak, A., Kravtsov, A., Nordlund, A., Pearce, F., Quilis, V., Rudd, D., Springel, V., Stone, J., Tasker, E., Teyssier, R., Wadsley, J., and Walder, R. (2007). Fundamental differences between SPH and grid methods. *MNRAS*, 380(3):963–978.

Allen, T. and Battley, M. (2015). Quantification of hydroelasticity in water impacts of flexible composite hull panels. *Ocean Engineering*, 100:117–125.

Arai, M. and Miyauchi, T. (1998). Numerical study of the impact of water on cylindrical shells, considering fluid-structure interactions. In *Proceedings of Conference on Practical Design of Ships and Mobile Structure (PRADS'98), The Hague, Netherlands*, pages 59–68.

Arntsen, O. A., Collados, X. R., and Tørum, A. (2011). Impact forces on a vertical pile from plunging breaking waves. In *6th International Conference on Coastal Structures, Yokohama, Japan*. World Scientific.

Baaijens, F. P. (2001). A fictitious domain/mortar element method for fluid-structure interaction. *International Journal for Numerical Methods in Fluids*, 35(7):743–761.

Bazilevs, Y., Takizawa, K., and Tezduyar, T. E. (2013). *Computational Fluid-Structure Interaction: Methods and Applications*. John Wiley & Sons.

Bereznitski, A. (2001). Slamming: The role of hydroelasticity. *International shipbuilding progress*, 48(4):333–351.

Bishop, R. E. D., Price, W. G., and Wu, Y. (1986). A general linear hydroelasticity theory of floating structures moving in a seaway. *Philosophical Transactions of the Royal Society of London A: Mathematical, Physical and Engineering Sciences*, 316(1538):375–426.

Brackbill, J. U., Kothe, D. B., and Zemach, C. (1992). A continuum method for modeling surface tension. *Journal of Computational Physics*, 100(2):335–354.

Bredmose, H., Bullock, G. N., and Hogg, A. J. (2014). Violent breaking wave impacts. Part 3: Effects of scale and aeration. *Accepted paper: Journal of Fluid Mechanics.*

Bredmose, H., Bullock, G. N., and Hogg, A. J. (2015). Violent breaking wave impacts. Part 3. Effects of scale and aeration. *Journal of Fluid Mechanics*, 765:82–113.

Bredmose, H. and Jacobsen, N. G. (2010). Breaking Wave Impacts on Offshore Wind Turbine Foundations: Focused Wave Groups and CFD. In *ASME 2010 29th International Conference on Ocean, Offshore and Arctic Engineering*, pages 397–404. American Society of Mechanical Engineers.

Bredmose, H., Peregrine, D. H., and Bullock, G. N. (2009). Violent breaking wave impacts. Part 2: modelling the effect of air. *Journal of Fluid Mechanics*, 641:389–430.

Bredmose, H., Slabiak, P., Sahlberg-Nielsen, L., and Schlütter, F. (2013). Dynamic excitation of monopiles by steep and breaking waves: experimental and numerical study. In *ASME 2013 32nd International Conference on Ocean, Offshore and Arctic Engineering*, pages V008T09A062–V008T09A062. American Society of Mechanical Engineers.

Buchner, B. (1995). The Impact of Green Water on FPSO Design. In *Offshore Technology Conference*. Offshore Technology Conference.

Buchner, B., Hodgson, T., Ballard, E., Barltrop, N., Falkenberg, E., Fyfe, S., Soares, C. G., and Iwanowski, B. (2004). Summary report on design guidance and assessment methodologies for wave slam and green water impact loading. European Community project 15874-1-OE, SAFE-FLOW Project.

Bullock, G. N., Obhrai, C., Peregrine, D. H., and Bredmose, H. (2007). Violent breaking wave impacts. Part 1: Results from large-scale regular wave tests on vertical and sloping walls. *Coastal Engineering*, 54(8):602–617.

Campbell, I. M. C. and Weynberg, P. A. (1980). *Measurement of parameters affecting slamming.* University of Southampton, Department of Aeronautics and Astronautics.

Cartmill, J. W. and Yang Su, M. (1993). Bubble size distribution under saltwater and freshwater breaking waves. *Dynamics of Atmospheres and Oceans*, 20(1):25–31.

Chan, E.-S., Cheong, H.-F., and Tan, B.-C. (1995). Laboratory study of plunging wave impacts on vertical cylinders. *Coastal Engineering*, 25(1–2):87–107.

Chaplin, J. R., Rainey, R. C. T., and Yemm, R. W. (1997). Ringing of a vertical cylinder in waves. *Journal of Fluid Mechanics*, 350:119–147.

Chella, M. A., Tørum, A., and Myrhaug, D. (2012). An Overview of Wave Impact Forces on Offshore Wind Turbine Substructures. *Energy Procedia*, 20:217–226.

Chen, X.-j., Wu, Y.-s., Cui, W.-c., and Jensen, J. J. (2006). Review of hydroelasticity theories for global response of marine structures. *Ocean Engineering*, 33(3–4):439–457.

Choi, S.-J., Lee, K.-H., Hong, K., Shin, S.-H., and Gudmestad, O. (2013). Nonlinear Wave Forces on an Offshore Wind Turbine Foundation in Shallow Waters. *International Journal of Ocean System Engineering*, 3(2):68–76.

Christensen, E. D., Bredmose, H., and Hansen, E. A. (2005). Extreme wave forces and wave run-up on offshore windturbine foundations. *Proceedings of Copenhagen Offshore Wind*.

Corte, C. and Grilli, S. T. (2006). Numerical modeling of extreme wave slamming on cylindrical offshore support structures. In *the Sixteenth International Offshore and Polar Engineering Conference*.

Courant, R., Friedrichs, K., and Lewy, H. (1928). Über die partiellen Differenzengleichungen der mathematischen Physik. *Math. Ann.*, 100(1):32–74.

Crawford, A. R. (1999). *Measurement and Analysis of Wave Loading on a Full Scale Coastal Structure*. Ph.D. Thesis, Plymouth University, Plymouth, UK.

Cruz, A. M. and Krausmann, E. (2008). Damage to offshore oil and gas facilities following hurricanes Katrina and Rita: An overview. *Journal of Loss Prevention in the Process Industries*, 21(6):620–626.

Damsgaard, M. L., Gravesen, H., and Andersen, T. L. (2007). Design loads on platforms on offshore wind turbine foundations with respect to vertical wave run-up. In *Proceedings of Offshore Wind 2007 Conference & Exhibition*, page 7. The European Wind Energy Association.

Deane, G. B. and Stokes, M. D. (2002). Scale dependence of bubble creation mechanisms in breaking waves. *Nature*, 418(6900):839–844.

Deparis, S., Discacciati, M., Fourestey, G., and Quarteroni, A. (2006). Fluid–structure algorithms based on Steklov–Poincaré operators. *Computer Methods in Applied Mechanics and Engineering*, 195(41):5797–5812.

Dias, F. and Ghidaglia, J.-M. (2018). Slamming: Recent Progress in the Evaluation of Impact Pressures. *Annual Review of Fluid Mechanics*, 50(1):243–273.

Donea, J., Fasoli-Stella, P., and Giuliani, S. (1977). Lagrangian and Eulerian finite element techniques for transient fluid-structure interaction problems.

Donea, J., Huerta, A., Ponthot, J.-P., and Rodríguez-Ferran, A. (2004). Arbitrary Lagrangian–Eulerian Methods. In *Encyclopedia of Computational Mechanics*. John Wiley & Sons, Ltd.

Dunne, T. (2006). An Eulerian approach to fluid–structure interaction and goal-oriented mesh adaptation. *Int. J. Numer. Meth. Fluids*, 51(9-10):1017–1039.

el Moctar, O., Ley, J., Oberhagemann, J., and Schellin, T. (2017). Nonlinear computational methods for hydroelastic effects of ships in extreme seas. *Ocean Engineering*, 130:659–673.

Fallah, N. (2004). A cell vertex and cell centred finite volume method for plate bending analysis. *Computer Methods in Applied Mechanics and Engineering*, 193(33–35):3457–3470.

Faltinsen, O. M. (1997). The effect of hydroelasticity on ship slamming. *Philosophical Transactions of the Royal Society of London A: Mathematical, Physical and Engineering Sciences*, 355(1724):575–591.

Faltinsen, O. M. (2000). Hydroelastic slamming. *J Mar Sci Technol*, 5(2):49–65.

Faltinsen, O. M. (2014). Hydrodynamics of marine and offshore structures. *J Hydrodyn*, 26(6):835–847.

Faltinsen, O. M., Kvålsvold, J., and Aarsnes, J. V. (1997). Wave impact on a horizontal elastic plate. *J Mar Sci Technol*, 2(2):87–100.

Faltinsen, O. M., Landrini, M., and Greco, M. (2004). Slamming in marine applications. *Journal of Engineering Mathematics*, 48(3-4):187–217.

Faltinsen, O. M. and Timokha, A. N. (2009). *Sloshing*, volume 577. Cambridge university press Cambridge.

Fang, J., Parriaux, A., Rentschler, M., and Ancey, C. (2009). Improved SPH methods for simulating free surface flows of viscous fluids. *Applied Numerical Mathematics*, 59(2):251–271.

Felippa, C. A., Park, K. C., and Farhat, C. (2001). Partitioned analysis of coupled mechanical systems. *Computer Methods in Applied Mechanics and Engineering*, 190(24–25):3247–3270.

Franck, R. M. and Lazarus, R. B. (1964). Mixed eulerian-lagrangian method. *Methods in computational physics*, 3:47–67.

Ge, C. (2002). *Global Hydroelastic Response of Catamarans due to Wetdeck Slamming*. Ph.D. Thesis, Norwegian University of Science and Technology, Trondheim, Norway.

Gerbeau, J.-F. and Vidrascu, M. (2003). A Quasi-Newton Algorithm Based on a Reduced Model for Fluid-Structure Interaction Problems in Blood Flows. *ESAIM: Mathematical Modelling and Numerical Analysis*, 37(04):631–647.

Ghadirian, A. and Bredmose, H. (2019). Pressure impulse theory for a slamming wave on a vertical circular cylinder. *Journal of Fluid Mechanics*, 867.

Gingold, R. A. and Monaghan, J. J. (1977). Smoothed particle hydrodynamics: theory and application to non-spherical stars. *MNRAS*, 181(3):375–389.

Glowinski, R., Pan, T. W., Hesla, T. I., and Joseph, D. D. (1999). A distributed Lagrange multiplier/fictitious domain method for particulate flows. *International Journal of Multiphase Flow*, 25(5):755–794.

Gomez-Gesteira, M., Rogers, B. D., Dalrymple, R. A., and Crespo, A. J. (2010). State-of-the-art of classical SPH for free-surface flows. *Journal of Hydraulic Research*, 48(sup1):6–27.

Gorf, P., Barltrop, N., Okan, B., Hodgson, T., and Rainey, R. (2002). FPSO bow damage in steep waves. *Actes De Colloques-Ifremer*, pages 37–46. Publisher: EDITIONS IFREMER.

Graham, D. I. and Hughes, J. P. (2008). Accuracy of SPH viscous flow models. *Int. J. Numer. Meth. Fluids*, 56(8):1261–1269.

Greco, M. (2001). *A two-dimensional study of green-water loading.* Doctoral thesis, Norwegian University of Science and Technology, Trondheim, Norway. Publisher: Fakultet for ingeniørvitenskap og teknologi.

Greenhow, M. (1987). Wedge entry into initially calm water. *Applied Ocean Research*, 9(4):214–223.

Habchi, C., Russeil, S., Bougeard, D., Harion, J.-L., Lemenand, T., Ghanem, A., Valle, D. D., and Peerhossaini, H. (2013). Partitioned solver for strongly coupled fluid–structure interaction. *Computers & Fluids*, 71:306–319.

Hallquist, J. O. (2001). *LS-DYNA keyword user's manual.* Livermore Software Technology Corporation.

Hattori, M., Arami, A., and Yui, T. (1994). Wave impact pressure on vertical walls under breaking waves of various types. *Coastal Engineering*, 22(1–2):79–114.

Heller, S. R. and Abramson, H. N. (1959). Hydroelasticity: A New Naval Science. *Journal of the American Society for Naval Engineers*, 71(2):205–209.

Hicks, P. D., Ermanyuk, E. V., Gavrilov, N. V., and Purvis, R. (2012). Air trapping at impact of a rigid sphere onto a liquid. *Journal of Fluid Mechanics*, 695:310–320.

Hicks, P. D. and Purvis, R. (2013). Liquid–solid impacts with compressible gas cushioning. *Journal of Fluid Mechanics*, 735:120–149.

Hildebrandt, A. (2012). *On Pressures, Forces, and Hydrodynamics due to Breaking Waves on Offshore Wind Turbines.* PhD thesis, Leibniz University, Hannover, Germany.

Hildebrandt, A. and Schlurmann, T. (2012). Breaking Wave Kinematics, Local Pressures, and Forces on a Tripod Structure. *Int. Conf. Coastal. Eng.*, 1(33):structures.71.

Hirdaris, S. E. and Temarel, P. (2009). Hydroelasticity of ships: Recent advances and future trends. *Proceedings of the Institution of Mechanical Engineers, Part M: Journal of Engineering for the Maritime Environment*, 223(3):305–330.

Hirt, C. W., Amsden, A. A., and Cook, J. L. (1974). An arbitrary Lagrangian-Eulerian computing method for all flow speeds. *Journal of Computational Physics*, 14(3):227–253.

Holzapfel, G. A. (2000). *Nonlinear Solid Mechanics: A Continuum Approach for Engineering.* Wiley.

Hou, G., Wang, J., and Layton, A. (2012). Numerical methods for fluid-structure interaction—a review. *Commun. Comput. Phys*, 12(2):337–377.

Hübner, B., Walhorn, E., and Dinkler, D. (2004). A monolithic approach to fluid–structure interaction using space–time finite elements. *Computer Methods in Applied Mechanics and Engineering*, 193(23–26):2087–2104.

Irschik, K., Sparboom, U., and Oumeraci, H. (2004). Breaking Wave Loads on a Slender Pile in Shallow Water. In *COASTAL ENGINEERING CONFERENCE*, volume 29, page 568. ASCE AMERICAN SOCIETY OF CIVIL ENGINEERS.

Issa, R. I. (1986). Solution of the implicitly discretised fluid flow equations by operator-splitting. *Journal of Computational Physics*, 62(1):40–65.

Jasak, H. (1996). *Error analysis and estimation for the finite volume method with applications to fluid flows.* Ph.D., Imperial College London (University of London).

Jasak, H., Jemcov, A., and Tukovic, Z. (2007). OpenFOAM: A C++ library for complex physics simulations. In *International workshop on coupled methods in numerical dynamics*, volume 1000, pages 1–20.

Jasak, H. and Tukovic, Z. (2006). Automatic mesh motion for the unstructured finite volume method. *Transactions of FAMENA*, 30(2):1–20.

Jasak, H. and Weller, H. G. (2000). Application of the finite volume method and unstructured meshes to linear elasticity. *International journal for numerical methods in engineering*, 48(2):267–287.

Kapsenberg, G. K. (2011). Slamming of ships: where are we now? *Philosophical Transactions of the Royal Society of London A: Mathematical, Physical and Engineering Sciences*, 369(1947):2892–2919.

Kassiotis, C. (2008). Which strategy to move the mesh in the Computational Fluid Dynamic code OpenFOAM. *Report École Normale Supérieure de Cachan. Available online: http://perso. crans. org/kassiotis/openfoam/movingmesh. pdf.*

Kassiotis, C. (2009). *Nonlinear fluid-structure interaction: a partitioned approach and its application through component technology.* PhD thesis, Université Paris-Est.

Kassiotis, C., Ibrahimbegovic, A., Niekamp, R., and Matthies, H. G. (2011). Nonlinear fluid–structure interaction problem. Part II: space discretization, implementation aspects, nested parallelization and application examples. *Comput Mech*, 47(3):335–357.

Katsir, Y., Goldstein, G., and Marmur, A. (2015). Bubble the wave or waive the bubble: Why seawater waves foam and freshwater waves do not? *Colloids and Interface Science Communications*, 6:9–12.

Kettle, A. J. (2015). Storm Britta in 2006: offshore damage and large waves in the North Sea. *Natural Hazards & Earth System Sciences Discussions*, 3(9).

Korobkin, A. A. (2006). Second-order Wagner theory of wave impact. *J Eng Math*, 58(1-4):121–139.

Kwon, S. H., Lee, H. S., Park, J. S., Ha, M. K., and Kim, Y. J. (2001). - Analysis of Ringing by Continuous Wavelet Transform. In Wu, Y.-S., Cui, W.-C., and Zhou, G.-J., editors, *Practical Design of Ships and Other Floating Structures*, pages 587–592. Elsevier Science Ltd, Oxford.

Küttler, U. and Wall, W. A. (2008). Fixed-point fluid–structure interaction solvers with dynamic relaxation. *Comput Mech*, 43(1):61–72.

Lamarre, E. and Melville, W. (1992). Instrumentation for the measurement of void-fraction in breaking waves: laboratory and field results. *IEEE Journal of Oceanic Engineering*, 17(2):204–215.

Lange, N. A. and Rung, T. (2011). Impact Tests in Pure and Aerated Water. pages 559–567.

LeVeque, R. J. (2002). *Finite Volume Methods for Hyperbolic Problems.* Cambridge University Press.

Lin, M.-C. and Shieh, L.-D. (1997). Flow visualization and pressure characteristics of a cylinder for water impact. *Applied Ocean Research*, 19(2):101–112.

Liu, I.-S. (2002). *Continuum Mechanics*. Springer Science & Business Media.

Liu, M. B. and Liu, G. R. (2010). Smoothed Particle Hydrodynamics (SPH): an Overview and Recent Developments. *Arch Computat Methods Eng*, 17(1):25–76.

Lucy, L. B. (1977). Numerical approach to the testing of the fission hypothesis. *Astronomical Journal*, 82(12):1013–1024.

Luengo Frades, J., Negro, V., García Barba, J., Martín-Antón, M., López-Gutiérrez, J. S., Esteban, M. D., and Moreno Blasco, L. J. (2019). Preliminary Design for Wave Run-Up in Offshore Wind Farms: Comparison between Theoretical Models and Physical Model Tests. *Energies*, 12(3):492. Number: 3 Publisher: Multidisciplinary Digital Publishing Institute.

Lyu, W., Moctar, O. e., Potthoff, R., and Neugebauer, J. (2017). Experimental and numerical investigation of sloshing using different free surface capturing methods. *Applied Ocean Research*, 68:307–324.

Löhner, R. and Yang, C. (1998). Improved ALE mesh velocities for moving bodies. *Communications in numerical methods in engineering*, (12):599–608.

Ma, Z. H., Causon, D. M., Qian, L., Mingham, C. G., Mai, T., Greaves, D., and Raby, A. (2016). Pure and aerated water entry of a flat plate. *Physics of Fluids (1994-present)*, 28(1):016104.

MAIB (2007). Report on the Investigation of the Structural Failure of MSC Napoli, English Channel on 18 January 2007. Technical Report 2007-9, UK Marine Accident Investigation branch (MAIB). Publisher: Marine Accident Investigation Branch Southampton, Hampshire, UK.

Matthies, H. G., Niekamp, R., and Steindorf, J. (2006). Algorithms for strong coupling procedures. *Computer Methods in Applied Mechanics and Engineering*, 195(17–18):2028–2049.

Matthies, H. G. and Steindorf, J. (2002). Partitioned but strongly coupled iteration schemes for nonlinear fluid–structure interaction. *Computers & Structures*, 80(27–30):1991–1999.

Matthies, H. G. and Steindorf, J. (2003). Partitioned strong coupling algorithms for fluid–structure interaction. *Computers & Structures*, 81(8–11):805–812.

Miao, G. (1988). *Hydrodynamic forces and dynamic responses of circular cylinders in wave zones*. PhD Thesis, University of Trondheim.

Miller, S. T., Jasak, H., Boger, D. A., Paterson, E. G., and Nedungadi, A. (2013). A pressure-based, compressible, two-phase flow finite volume method for underwater explosions. *Computers & Fluids*, 87:132–143.

Mittal, R. and Iaccarino, G. (2005). Immersed Boundary Methods. *Annual Review of Fluid Mechanics*, 37(1):239–261.

Mizoguchi, S. and Tanizawa, K. (1996). Impact wave loads due to slamming–a review. *Ship Technology Research*, 43(4):139–154.

Monaghan, J. J. (2005). Smoothed particle hydrodynamics. *Rep. Prog. Phys.*, 68(8):1703.

Morgan, G. C. and Zang, J. (2010). Using the rasInterFoam CFD model for non-linear wave interaction with a cylinder. In *Proc. ISOPE*.

Moukalled, F., Mangani, L., and Darwish, M. (2015). *The Finite Volume Method in Computational Fluid Dynamics: An Advanced Introduction with OpenFOAM® and Matlab*. Springer.

MSC.Software (2001). *MSC. DytranTheory manual*. MSC.Software company.

Murrone, A. and Guillard, H. (2005). A five equation reduced model for compressible two phase flow problems. *Journal of Computational Physics*, 202(2):664–698.

Nguyen, V. P., Rabczuk, T., Bordas, S., and Duflot, M. (2008). Meshless methods: A review and computer implementation aspects. *Mathematics and Computers in Simulation*, 79(3):763–813.

Noh, W. F. (1963). Cel: A Time-Dependent, Two-Space-Dimensional, Coupled Eulerian-Lagrange Code. Technical Report UCRL-7463, Lawrence Radiation Lab., Univ. of California, Livermore.

Oberhagemann, J. and el Moctar, O. (2011). Numerical And Experimental Investigations of Whipping And Springing of Ship Structures. In *International Offshore and Polar Engineering Conference*. International Society of Offshore and Polar Engineers.

Oliver, J. M. (2007). Second-order Wagner theory for two-dimensional water-entry problems at small deadrise angles. *Journal of Fluid Mechanics*, 572:59–85.

Oumeraci, H., Partenscky, H. W., Kohlhase, S., and Klammer, P. (1993). Impact loading and dynamic response of caisson breakwaters-Results of large-scale model tests. In *Coastal Engineering 1992*, pages 1475–1488.

Panciroli, R., Ubertini, S., Minak, G., and Jannelli, E. (2015). Experiments on the Dynamics of Flexible Cylindrical Shells Impacting on a Water Surface. *Exp Mech*, 55(8):1537–1550.

Park, K. C., Felippa, C. A., and Ohayon, R. (2001). Partitioned formulation of internal fluid–structure interaction problems by localized Lagrange multipliers. *Computer Methods in Applied Mechanics and Engineering*, 190(24–25):2989–3007.

Peseux, B., Gornet, L., and Donguy, B. (2005). Hydrodynamic impact: Numerical and experimental investigations. *Journal of Fluids and Structures*, 21(3):277–303.

Peskin, C. S. (1972). Flow patterns around heart valves: A numerical method. *Journal of Computational Physics*, 10(2):252–271.

Peskin, C. S. (2002). The immersed boundary method. *Acta Numerica*, 11:479–517.

Plumerault, L. R., Astruc, D., and Maron, P. (2012a). The influence of air on the impact of a plunging breaking wave on a vertical wall using a multifluid model. *Coastal Engineering*, 62:62–74.

Plumerault, L.-R., Astruc, D., Villedieu, P., and Maron, P. (2012b). A numerical model for aerated-water wave breaking. *Int. J. Numer. Meth. Fluids*, 69(12):1851–1871.

Price, D. J. and Federrath, C. (2010). A comparison between grid and particle methods on the statistics of driven, supersonic, isothermal turbulence. *MNRAS*, 406(3):1659–1674.

Richter, T. (2013). A Fully Eulerian formulation for fluid–structure-interaction problems. *Journal of Computational Physics*, 233:227–240.

Ross, M. R., Felippa, C. A., Park, K. C., and Sprague, M. A. (2008). Treatment of acoustic fluid–structure interaction by localized Lagrange multipliers: Formulation. *Computer Methods in Applied Mechanics and Engineering*, 197(33–40):3057–3079.

Ross, M. R., Sprague, M. A., Felippa, C. A., and Park, K. C. (2009). Treatment of acoustic fluid–structure interaction by localized Lagrange multipliers and comparison to alternative interface-coupling methods. *Computer Methods in Applied Mechanics and Engineering*, 198(9–12):986–1005.

Rusche, H. (2003). *Computational fluid dynamics of dispersed two-phase flows at high phase fractions*. Ph.D., Imperial College London (University of London).

Sagar, H., Ley, J., and el Moctar, B. (2015). Hydroelasticity effects of wave induced loads on offshore monopile structure. In *7th international conference on hydroelasticity in marine technology, Split, Croatia*, pages 82–101.

Schimmels, S., Schlurmann, T., Brühl, M., and Goseberg, N. (2018). Large scale experiments in coastal and Ocean engineering A Review of 35 years of physical model tests in the Large Wave Flume (Grosser Wellenkanal, GWK). Technical report, Forschungszentrum Küste.

Scott, J. C. (1975). The role of salt in whitecap persistence. *Deep Sea Research and Oceanographic Abstracts*, 22(10):653–657.

Shahmiri, S. (2014). *A Hybrid Fixed-Grid-ALE Approach for Fluid-Structure Interaction.* PhD thesis, Technische Universität München.

Shams, A. and Porfiri, M. (2015). Treatment of hydroelastic impact of flexible wedges. *Journal of Fluids and Structures*, 57:229–246.

Shams, A., Zhao, S., and Porfiri, M. (2017). Analysis of hydroelastic slamming of flexible structures: modeling and experiments. *Procedia Engineering*, 199:1484–1488.

Shibue, T., Ito, A., and Nakayama, E. (1993). Structural response analysis of a cylinder under water impact. *Journal of the Society of Naval Architects of Japan*, 1(174):479–484.

Slauenwhite, D. E. and Johnson, B. D. (1999). Bubble shattering: Differences in bubble formation in fresh water and seawater. *Journal of Geophysical Research: Oceans*, 104(C2):3265–3275.

Slone, A. K., Bailey, C., and Cross, M. (2003). Dynamic solid mechanics using finite volume methods. *Applied Mathematical Modelling*, 27(2):69–87.

Steindorf, J. (2002). *Partitionierte Verfahren für Probleme der Fluid-Struktur-Wechselwirkung.* PhD thesis, Mechanik-Zentrum.

Sun, H. (2007). *A Boundary Element Method Applied to Strongly Nonlinear Wave-Body Interaction Problems.* Fakultet for ingeniørvitenskap og teknologi.

Sun, H. and Faltinsen, O. M. (2006). Water impact of horizontal circular cylinders and cylindrical shells. *Applied Ocean Research*, 28(5):299–311.

Tenzer, M., el Moctar, O., and Schellin, T. E. (2015). Experimental investigation of impact loads during water entry. *Ship Technology Research*, 62(1):47–59. Publisher: Taylor & Francis _eprint: https://doi.org/10.1179/0937725515Z.0000000003.

Tsui, Y.-Y., Huang, Y.-C., Huang, C.-L., and Lin, S.-W. (2013). A Finite-Volume-Based Approach for Dynamic Fluid-Structure Interaction. *Numerical Heat Transfer, Part B: Fundamentals*, 64(4):326–349.

Tuitman, J. T. (2010). *Hydro-elastic response of ship structures to slamming induced whipping.* Doctoral thesis, TU Delft, Delft, Netherlands.

Tuković, Z., Karač, A., Cardiff, P., Jasak, H., and Ivanković, A. (2015). Parallel unstructured finite-volume method for fluid-structure interaction (Draft Version). *Journal of Fluids and Structures*.

Tuković, Z., Karač, A., Cardiff, P., Jasak, H., and Ivanković, A. (2018). OpenFOAM Finite Volume Solver for Fluid-Solid Interaction. *Transactions of FAMENA*, 42(3):1–31.

Tödter, S., el Moctar, O., Neugebauer, J., and Schellin, T. E. (2020). Experimentally Measured Hydroelastic Effects on Impact-Induced Loads During Flat Water Entry and Related Uncertainties. *J. Offshore Mech. Arct. Eng*, 142(1). Publisher: American Society of Mechanical Engineers Digital Collection.

Ubbink, O. (1997). *Numerical prediction of two fluid systems with sharp interfaces*. PhD thesis, University of London UK.

van Loon, R., Anderson, P. D., de Hart, J., and Baaijens, F. P. T. (2004). A combined fictitious domain/adaptive meshing method for fluid–structure interaction in heart valves. *Int. J. Numer. Meth. Fluids*, 46(5):533–544.

Van Nuffel, D. (2014). *Experimental study of the slamming induced pressures, forces and deformations of quasi-rigid and deformable bodies during vertical water entry.* PhD thesis, Ghent University.

von Karman, T. (1929). The impact on seaplane floats during landing. Technical note TN 321, National Advisory Committee for Aeronautics.

von Scheven, M. and Ramm, E. (2011). Strong coupling schemes for interaction of thin-walled structures and incompressible flows. *Int. J. Numer. Meth. Engng.*, 87(1-5):214–231.

Wagner, H. (1932). Über Stoß- und Gleitvorgänge an der Oberfläche von Flüssigkeiten. *Z. angew. Math. Mech.*, 12(4):193–215.

Walkden, M. J. A. (1999). *Model wave impulse loads on caisson breakwater aeration, scale and structural response.* Ph.D. Thesis, Plymouth University, Plymouth, UK.

Wall, W. A. (1999). *Fluid-struktur-interaktion mit stabilisierten finiten elementen.* PhD Thesis, Universität Stuttgart.

Wall, W. A., Genkinger, S., and Ramm, E. (2007). A strong coupling partitioned approach for fluid–structure interaction with free surfaces. *Computers & Fluids*, 36(1):169–183.

Wall, W. A., Gerstenberger, A., Gamnitzer, P., Förster, C., and Ramm, E. (2006). Large Deformation Fluid-Structure Interaction – Advances in ALE Methods and New Fixed Grid Approaches. In Bungartz, H.-J. and Schäfer, M., editors, *Fluid-Structure Interaction*, number 53 in Lecture Notes in Computational Science and Engineering, pages 195–232. Springer Berlin Heidelberg.

Weller, H. G. (2008). A new approach to VOF-based interface capturing methods for incompressible and compressible flow. *OpenCFD Ltd., Report TR/HGW*, 4.

Weller, H. G., Tabor, G., Jasak, H., and Fureby, C. (1998). A tensorial approach to computational continuum mechanics using object-oriented techniques. *Computers in Physics*, 12(6):620–631.

Wemmenhove, R. (2008). *Numerical simulation of two-phase flow in offshore environments.* PhD thesis, University of Groningen.

Wienke, J. (2001). *Druckschlagbelastung auf schlanke zylindrische Bauwerke durch brechende Wellen: theoretische und gro\s sma\s sstäbliche Laboruntersuchungen.* PhD thesis, TU Braunschweig, Braunschweig, Germany.

Wienke, J. and Oumeraci, H. (2005). Breaking wave impact force on a vertical and inclined slender pile—theoretical and large-scale model investigations. *Coastal Engineering*, 52(5):435–462.

Wood, D., Peregrine, D., and Bruce, T. (2000). Wave Impact on a Wall Using Pressure-Impulse Theory. I: Trapped Air. *Journal of Waterway, Port, Coastal, and Ocean Engineering*, 126(4):182–190.

Wu, Y. (1984). *Hydroelasticity of floating bodies.* Ph.D., University of Brunel.

Wu, Y.-S. and Cui, W.-C. (2009). Advances in the three-dimensional hydroelasticity of ships. *Proceedings of the Institution of Mechanical Engineers, Part M: Journal of Engineering for the Maritime Environment*, 223(3):331–348.

Zhang, Y., Mohtat, A., and Yim, S. C. (2015). Effect of Compressibility on Peak Impact Pressure and Pressure Distribution During Water Entry of a Wedge. page V011T12A007.

Zhou, D., Chan, E., and Melville, W. (1991). Wave impact pressures on vertical cylinders. *Applied Ocean Research*, 13(5):220–234.

Curriculum Vitae

Personal Details

Name	Ali Aghaei born on 26.08.1978 in Esfahan, Iran married, one child

Work Experience

Mar.2020 - current	Project Engineer at Ramboll, Hannover, Germany
Nov.2015 - Apr.2019	Research Associate at Coastal Research center, Leibniz University Hannover, Germany
Oct.2013 - Oct.2015	Student Research Assistant at Coastal Research center, Leibniz University Hannover, Germany
Jun.2009 - Sep.2013	Technical Office Chief Engineer at Mehraz Water Infrastructures Company, Tehran, Iran
Oct. 2008 - Jun. 2009	Construction Manager, Self-employed, Isfahan, Iran
Apr. 2007 - Oct. 2008	FEED Engineering Team Manager, Self-employed, Isfahan, Iran
Jul. 2001 - Apr. 2007	Structural Design Engineer at SBR Consultants, Isfahan, Iran

Education

Sep. 2002 - Mar. 2005	MSc., Civil Engineering, Marine structures, Sahand University of Technology, Tabriz, Iran
	Master thesis: 'New parametric Equations for estimating SCFs in tubular KK joints under axial, in plane and out of plane bending loads'
Sep. 1996 - Mar. 2001	Bachelor, Civil Engineering, University of Yazd, Yazd, Iran

Promotion Study

Sep. 2015 - Feb. 2022	Faculty of Civil Engineering and Geodetic Science, Leibniz University Hannover